Charles University

Second Faculty of Medicine

Doctoral Study Program: Neurosciences

Mgr. Tereza Filipi

Glial Cells in Progression of Amyotrophic Lateral Sclerosis

Gliové buňky v progresi amyotrofické laterální sklerózy

Dissertation Thesis

Supervisor: Ing. Miroslava Anděrová, CSc.

Prague, 2024

Prohlášení

Prohlašuji, že jsem závěrečnou práci zpracovala samostatně a že jsem řádně uvedla a citovala všechny použité prameny a literaturu. Současně prohlašuji, že práce nebyla využita k získání jiného nebo stejného titulu. Souhlasím s trvalým uložením elektronické verze mé práce v databázi systému meziuniverzitního projektu Theses.cz za účelem soustavné kontroly podobnosti kvalifikačních prací.

V Praze dne …..

TEREZA FILIPI

……………………….. …..

Podpis autora

Acknowledgements

I would like to thank my supervisor, Dr. Miroslava Anděrová, for her patience and guidance during my research experience in her laboratory. In addition, I would like to thank my colleagues and technicians, who participated in experiments and were a significant source of help and advice.

Glial cells in progression of Amyotrophic lateral sclerosis

Abstract

Glial cells are known to support neurons, maintain homeostasis in the nervous system and act as an immune defense to name a few of their physiological functions. In pathological conditions, they change their properties and become active participants with beneficial and/or harmful effects. The exact role they play in Amyotrophic lateral sclerosis (ALS) is not known, but with the urgent need for efficient therapy, there is a constant effort to precisely elucidate their involvement. We examined cortical astrocytes, microglia and oligodendrocytes in a SOD1(G93A) mouse model of ALS with the use of single-cell RNA sequencing and immunohistochemistry and then further focused on the functional properties of astrocytes in ALS and in Alzheimer's disease (AD) using *in situ* 3D-morphometry and the real-time iontophoretic method. The profiling revealed minimal changes in the cortical glia in the final stage of ALS, suggesting unsuitability of the model for future cortical studies. Nevertheless, with the use of the ALS mouse model on a different background, we were able to detect cortical and spinal astrogliosis and identify diminished K^+ uptake during hyperkalemia and downregulation of Kir4.1 in spinal ALS-affected astrocytes. The investigation in the AD model also showed diminished astrocytic swelling in response to hyperkalemia and hypo-osmotic stress. The overall results provide insights into the astrocytic homeostatic abilities during pathology and highlight the importance of using a reliable animal model.

Keywords

AD, ALS, astrocytes, microglia, oligodendrocytes, potassium uptake

Gliové buňky v progresi amyotrofické laterální sklerózy

Abstrakt

Gliové buňky jsou známy tím, že poskytují podporu neuronům, zajišťují homeostázu v nervovém systému nebo se účastní imunitních reakcí, což je ale jen několik z jejich mnoha fyziologických funkcí. Během patologií se však jejich funkce a vlastnosti mění a glie jsou aktivními účastníky s potenciálně protektivním a/nebo škodlivým účinkem. Přesná role gliových buněk v progresi Amyotrofické laterální sklerózy (ALS) není dosud známa, ale vzhledem k nutnosti efektivní léčby se na jejím objasnění neustále pracuje. My jsme se věnovali kortikálním astrocytům, mikrogliím a oligodendrocytům v myším modelu SOD1(G93A) s využitím sekvenování na úrovni jedné buňky a imunohistochemie a poté jsme se detailněji zaměřili na funkční vlastnosti astrocytů v průběhu ALS a také Alzheimerovy choroby (AD) s pomocí *in situ* 3D-morfometrie a iontoforetické metody v reálném čase. Profilování odhalilo pouze mírné změny u kortikálních glií ve finálním stádiu nemoci, což naznačuje nevhodnost tohoto modelu pro další studie zaměřené na mozkovou kůru. S využitím myšího ALS modelu s odlišným genetickým pozadím jsme nicméně identifikovali astrogliózu v mozkové kůře i v míše, společně se sníženým vychytáváním K^+ iontů a sníženou expresí Kir4.1 u míšních astrocytů. Experimenty v AD modelu ukázaly rovněž snížené vychytávání K^+ iontů během hyperkalémie i hypoosmotického stresu. Celkově naše výsledky poskytly vhled do homeostatických schopností astrocytů během patologie a ukázaly důležitost využití spolehlivého animálního modelu pro výzkum.

Klíčová slova

AD, ALS, astrocyty, mikroglie, oligodendrocyty, vychytávání draslíku

List of abbreviations

Aβ	amyloid-beta
AD	Alzheimer´s disease
ALS	Amyotrophic lateral sclerosis
AMPA	α-amino-3-hydroxy-5-methyl-4-isoxazolepropionic acid
Apc	gene encoding adenomatous polyposis coli
APC	adenomatous polyposis coli
APP	amyloid precursor protein
Apod	apolipoprotein D
Apoe	apolipoprotein E
ARM	activated response microglia
ATP	adenosine triphosphate
ATAXN2	ataxin 2
BDNF	brain-Derived neurotrophic factor
BBB	blood brain barrier
CA1	hippocampal cornu ammonis 1
CC3	cleaved-caspase 3
Cd11b	cluster of differentiation molecule 11b
Cd11c	cluster of differentiation molecule 11c
CD206	mannose receptor
CNS	central nervous system
COP	differentiation-committed oligodendrocyte precursors
CSFR1	colony stimulating factor 1 receptor
CTRL	control
CX3CR1	C-X3-C Motif Chemokine Receptor 1
CXCL1	C-X-C Motif Chemokine Ligand 1
CXCL10	C-X-C Motif Chemokine Ligand 10
CXCL12	C-X-C Motif Chemokine Ligand 12
CXCR4	C-X-C Motif Chemokine Receptor 4
C9orf72	gene encoding chromosome 9 open reading frame 72
C9ORF72	chromosome 9 open reading frame 72
DAM	disease associated microglia
DAA	disease associated astrocytes
DEA	differential expression analysis

DEG	differentially expressed gene
DE	differential expression
DNA	deoxyribonucleic acid
ECM	extracellular matrix
ECS	extracellular space
EAAT1	excitatory amino acid transporter 1
EAAT2	excitatory amino acid transporter 2
EGFP	enhanced green fluorescent protein
FACS	fluorescent activated cell sorting
fALS	familial Amyotrophic lateral sclerosis
Fus	gene encoding fused in sarcoma
FUS	fused in sarcoma
GFAP	glial fibrillary acidic protein
GLAST	glutamate aspartate transporter
GLT	glutamate transporter
GABA	gamma-aminobutyric acid
GO	gene ontology
GSEA	gene set enrichment analysis
HCN	hyperpolarization-activated cyclic nucleotide-gated
IFN	interferon
IFN-α/β	interferon alpha/beta
IFN-γ	interferon gamma
IEGs	immediate early genes
IFIT2	interferon-induced protein with tetratricopeptide repeats 2
IFIT3	interferon-induced protein with tetratricopeptide repeats 3
Ifit3m	gene encoding interferon induced transmembrane protein 3
IL	interleukin
IL-1β	interleukin 1 beta
IL-4	interleukin 4
IL6	interleukin 6
IL10	interleukin 10
IL-12	interleukin 12
IL-13	interleukin 13
IL-33	interleukin 33

IRM	interferon responsive microglia
ISM	intermediate state microglia
Kir4.1	potassium channel, inwardly rectifying subfamily J, member 10
LPS	lipopolysaccharide
log2FC	log2 fold change
MAPT	microtubule-associated protein tau
MBP	myelin basic protein
MCT1	monocarboxylate transporter 1
MFOL	myelin forming oligodendrocyte
MHCII	major histocompatibility complex class II
MN	motor neuron
MOL2	mature oligodendrocytes type 2
mRNA	messenger ribonucleic acid
MS	multiple sclerosis
NF-κβ	nuclear factor kappa-light-chain-enhancer of activated B cells
NFTs	neurofibrillary tangles
NMDA	N-methyl-D-aspartate
NO	nitric oxide
NOX2	NADPH oxidase 2
OPC	oligodendrocyte precursor cell
OPTN	optineurin
padj	adjusted p-value
PAM	proportion of activated microglia
PAR	protease-activated receptor
PBS	phosphate-buffer saline
PC	principal component
PCA	principal component analysis
PFA	paraformaldehyde
RNA	ribonucleic acid
RNS	reactive nitrogen species
ROS	reactive oxygen species
RTI	real-time iontophoretic
sALS	sporadic Amyotrophic lateral sclerosis
SLC	solute carrier

Sod1	gene encoding superoxide dismutase 1
SOD1	superoxid dismutase 1
Tardbp	gene encoding TAR DNA binding protein 43
TBK1	TANK-Binding Kinase 1
TDP-43	TAR DNA binding protein 43
TGF-β	transforming growth factor beta
TGF-β1	transforming growth factor beta 1
TNF	tumor necrosis factor
TNF-α	tumor necrosis factor alpha
TRP	transient receptor potential
TREM2	triggering receptor expressed on myeloid cells 2
UMAP	uniform manifold approximation and projection
UBQLN2	ubiquilin 2
Ym1	gene encoding chitinase-like 3

TABLE OF CONTENTS

1 INTRODUCTION

Amyotrophic lateral sclerosis (ALS) also known as Lou Gehrig´s disease is a fatal neurological disease that primarily affects motor neurons (MNs) in the motor cortex, brainstem and spinal cord. Motor neurons progressively degenerate during ALS and the transmission of signals from the central nervous system (CNS) to muscles is impaired, which leads to muscle weakness, atrophy and ultimately paralysis. Early symptoms often include muscle twitching, cramping and stiffness, and as the disease progresses, it affects speech, swallowing and breathing, ultimately leading to respiratory failure and death. The median survival is from 3 to 5 years from diagnosis. The diagnosis is complicated and there is currently no cure, but treatments such as Riluzole and Edaravone can modestly slow disease progression (Neupane et al., 2023). A main roadblock to developing effective therapy is the lack of understanding of the pathological cellular and molecular mechanisms that cause and/or contribute to the disease.

Glial cells, traditionally considered as only supportive, are now recognized as active participants in the pathology of neurodegenerative diseases, including ALS (Filipi et al., 2020). In ALS, glial cells become dysfunctional and contribute to the disease progression. Several mechanisms such as failure of metabolic supply, glutamate excitotoxicity and inflammatory response have already been elucidated; however, the precise role of glia during the whole course of the disease is still unknown. One of the essential tools for studying glia in ALS is a reliable animal model, allowing us to closely mimic the disease´s complex pathology, and investigate the specific roles and interactions.

The goal of this thesis was to better characterize the ALS animal model with a focus on glial cells and analyze their functioning during the pathology progression. This knowledge could serve as another piece of the puzzle in the development of glia-targeted ALS therapy.

1.1 Glia in Physiology

Glial cells were first recognized in the 19th century and were thought to have a sole purpose as so-called nerve glue. However, further studies have shown that their role in the CNS is much bigger and it is probable that the full spectrum of their functions is yet to be discovered. Glia constitute between 33 and 66 % of the total brain mass, depending on the mammalian species (Azevedo et al., 2009, Herculano-Houzel, 2014). In the CNS, their population is not identical but can be subdivided into four major groups: astrocytes, microglia, oligodendrocytes and their progenitors NG2-glia.

Astrocytes are the most abundant population of glia in the adult brain (Kettenmann and Ransom, 2004) and as such, they are probably the best described among all glial cell types. The name refers to their shape, which is indeed star-like (Fig. 1) with a certain morphology heterogeneity across various regions of the CNS. They are derived from progenitor cells in neuroepithelium and then integrated into cellular networks called syncytia. Individual astrocytes in the syncytium are connected by gap junctions, which enables intercellular transport of ions and other molecules smaller than 1 kDa (Verkhratsky et al., 2020).

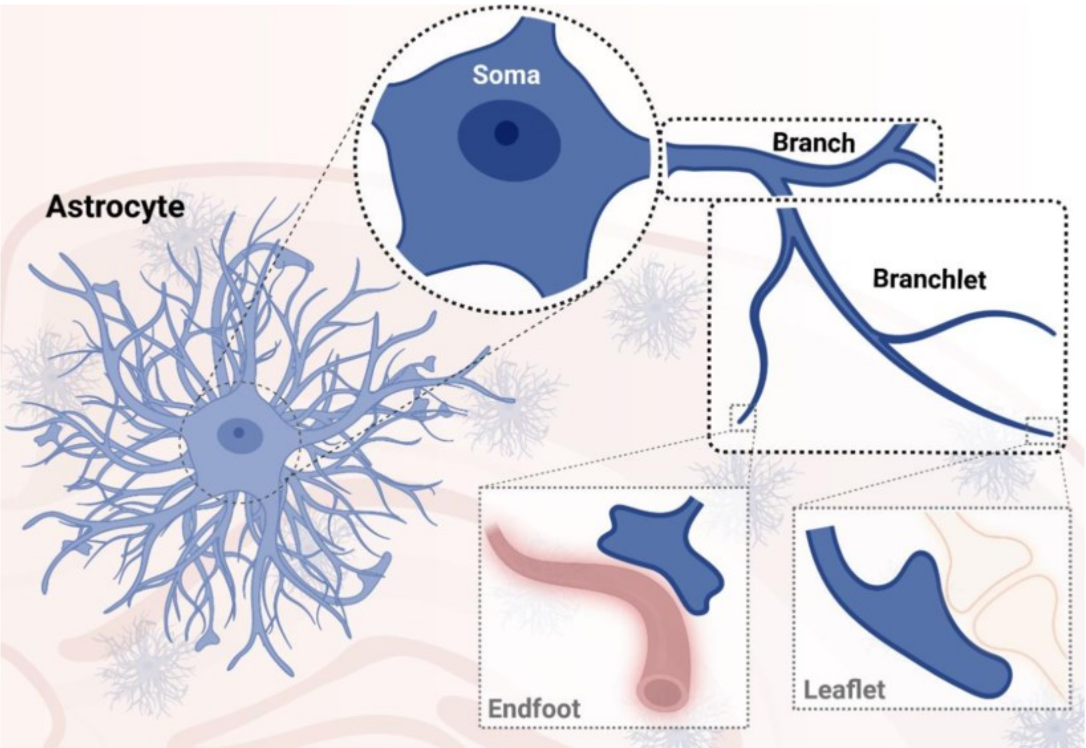

Fig. 1 Characteristic astrocytic morphology. The illustration shows the astrocyte´s cell body (soma), ramifying branches, branchlets and eventually endfeet closely attached to a blood vessel, and leaflets in close contact with synapses. This close proximity allows for the astrocyte functions such as maintenance of the BBB and synapses (Cabral-Costa and Kowaltowski, 2023).

Astrocytes execute a wide array of functions, which can be collectively called homeostatic. Some of their many responsibilities include ion and transmitter homeostasis, metabolic energy support, regulation of pH, synaptic maturation and maintenance, blood-brain barrier (BBB) maintenance, operation of the glymphatic system or chemosensing of oxygen and carbon dioxide (Verkhratsky and Nedergaard, 2018). To execute all these functions, the cell membrane contains numerous ion channels, receptors and transporters.

Potassium channels are dominant on the membrane, and the K^+ conductance defines the homeostatic potential of astrocytes, as it supports the movement of ions and provides an electrical driving force for membrane transporters (Nwaobi et al., 2016). Astrocytes express inward rectifier K^+ channels, voltage-independent K^+ channels, voltage-gated K^+ channels and calcium dependent K^+ channels. Beside potassium, they express calcium channels, transient receptor potential (TRP) channels, aquaporins, hyperpolarization-activated cyclic nucleotide-gated (HCN) channels and despite being non-excitable also voltage-gated sodium channels (Verkhratsky et al., 2020).

(Kettenmann and Zorec, 2012) described that expression of receptors is restrictive and regulated by the local neurochemical environment but generally astrocytes express purinoceptors, gamma-aminobutyric acid (GABA) receptors, glycine receptors, acetylcholine receptors, receptors for monoamines, cannabinoids and neuropeptides, protease-activated receptors (PAR) and glutamate receptors both ionotropic (α-amino-3-hydroxy-5-methyl-4-isoxazolepropionic acid (AMPA) and N-methyl D-aspartate (NMDA) and metabotropic.

When it comes to transporters, the most prominent and functionally important is the Na^+-K^+ ATPase, which sustains the membrane potential. Another important group is the solute carrier (SLC) transporters family, which among others contain glutamate and glutamine transporters. Astrocytes are the main glutamate sink (Danbolt, 2001) and express two types of glutamate transporters: the excitatory amino acid transporter 1 (EAAT1) (GLAST1 in rodents) and the excitatory amino acid transporter 2 EAAT2 (GLT-1 in rodents). Their ability to transport excessive glutamate from the synaptic cleft is crucial for the proper functioning of synapses. Molecules of glutamate are processed in the astrocytes by glutamine synthetase and the resulting glutamine is then released by glutamine transporters into extracellular space. This glutamine is then taken up by neurons and serves as a new supply of glutamate. This mechanism of exchange is called the glutamate-glutamine shuttle (Fig. 2).

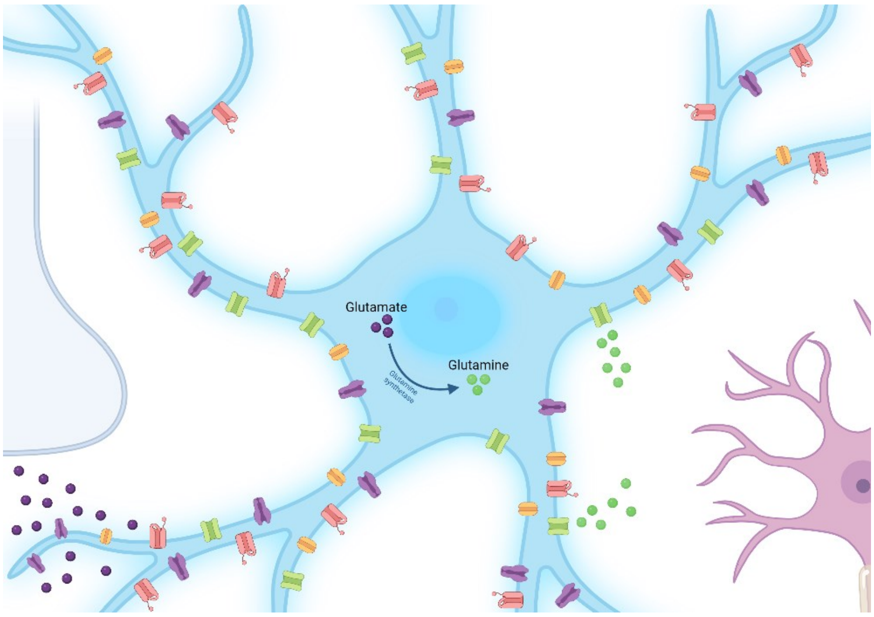

Fig. 2 Schematic overview of the glutamate-glutamine shuttle. Molecules of glutamate (purple) are transported from the synaptic cleft via glutamate receptors (purple) into astrocytes, where they are processed via the enzymatic reaction with glutamine synthetase. The resulting glutamine is then transferred to extracellular space through glutamine receptors and serves as an energy source for neurons. The image was created using BioRender.

Microglia are derived from yolk sac-primitive macrophages (Ginhoux et al., 2010) and are the main immune cells in the CNS. They enter the brain early (between fourth and 24th gestational weeks) and their population is maintained by local proliferation (Menassa and Gomez-Nicola, 2018). Microglial distribution throughout the adult brain is uneven and the density can greatly vary (Lawson et al., 1990). With that comes also regional and temporal heterogeneity (Augusto-Oliveira et al., 2019). Microglia maintain the neuronal environment by constantly monitoring their surroundings and are the first cells to respond to any pathological processes or changes. They are endowed with a wide range of receptors, which makes them highly sensitive to disruptions in cerebral homeostasis (Liu et al., 2016). These receptors detect neurotransmitters or danger-associated molecules such as adenosine triphosphate (ATP), lipopolysaccharide (LPS) or deoxyribonucleic acid (DNA) and ribonucleic acid (RNA) and provide signals regulating the alteration between the homeostatic and active profile of microglia (Benarroch, 2013). The profiles are associated with distinct cell morphology and changes in the cell transcriptome. Homeostatic microglia are highly ramified cells with multiple branches and processes, which are continuously protruding and retracting. When such microglia are activated, they shorten their processes, the cell body enlarges and their overall shape could be likened to amoeba (Gao et al., 2023) (Fig. 3).

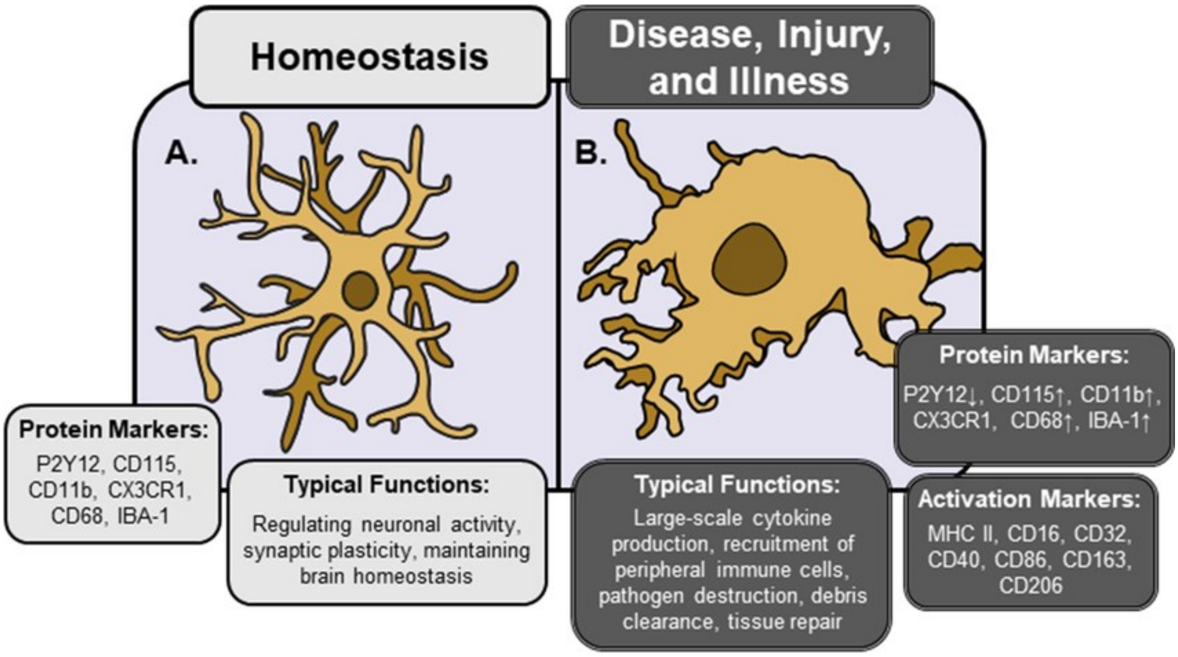

Fig. 3 Morphological differences between homeostatic and activated microglia. A) Microglia display the characteristic ramified morphology and expression profile characterized by homeostatic markers such as P2Y12, CX3CR1, etc. They execute typical functions such as regulating the neuronal activity and maintaining CNS homeostasis. However, when stimulated, microglia can quickly change their phenotype. B) Activated microglia acquire amoeboid morphology with enlarged soma, shorter, thicker and less ramified processes. They downregulate homeostatic genes and express markers of activation. In an activated state, they produce cytokines, recruit peripheral immune cells and perform phagocytosis to destroy pathogens. (Woodburn et al., 2021).

As mentioned above, microglia express a wide range of receptors. Chemokine receptors (C-X-C Motif Chemokine Ligand 1 (CX3CR1) and C-X-C Motif Chemokine Ligand 4 (CXCR4)), as well as integrins (a cluster of differentiation molecules 11b and 11c (CD11b,CD11c)), which control microglial migration and location within the CNS and increase their ability to bind target cells for phagocytosis and elimination. Immune receptors regulate the magnitude and duration of activation. One of these is thoroughly studied triggering a receptor expressed on myeloid cells 2 (TREM2), which binds the phospholipids and works as an activating receptor (Colonna and Wang, 2016). Activation is also regulated by receptors for proinflammatory and anti-inflammatory cytokines such as interferons (IFN) IFN-α/β, IFN-γ, tumor necrosis factor alpha (TNF-α), interleukins (IL) IL-1β, IL-10, and transforming growth factor beta (TGF-β) (Colonna and Butovsky, 2017). In addition, microglia express multiple receptors for neurotransmitters and neuropeptides, which promote neural-glia communication (Pocock and Kettenmann, 2007). There receptors allow for the detection and elimination of damaged neurons, promote neurotrophic factors for neural regeneration and regulate the release of inflammatory cytokines (Colonna and Butovsky, 2017).

Oligodendrocytes are the myelin-forming cells of the CNS derived from oligodendrocyte progenitor cells (OPCs). These progenitors persist in the adult CNS and serve as a source of oligodendrocytes to replace lost myelin or to myelinate new connections (Butt et al., 2019). The process of oligodendrogenesis is multistep, starting with a change of the OPC´s gene expression and morphology, gradually going through developmental stages. and giving rise to a mature myelinating oligodendrocyte (Fig. 4).

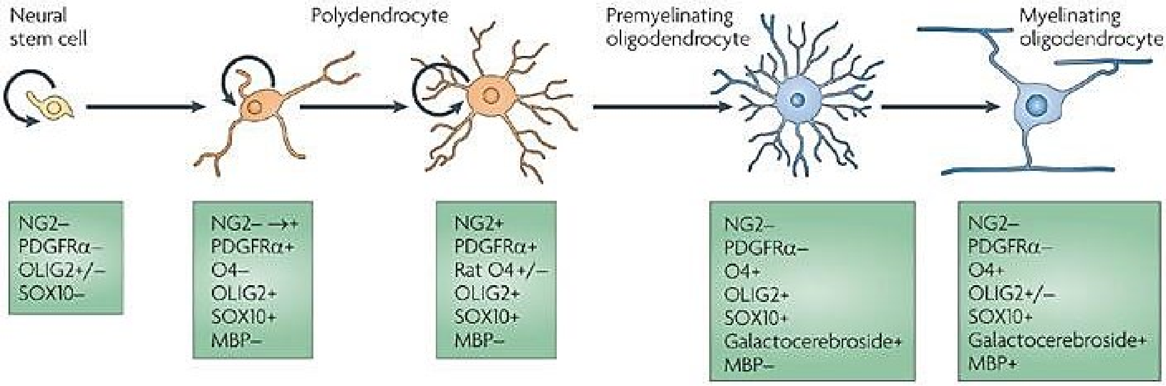

Fig. 4 Representation of individual developmental stages of the oligodendrocyte lineage. Each stage is depicted with its characteristic morphology and specific gene expression profile. Circular arrows represent the ability to self-renew. The cell ramification changes during the developmental period and so does the expression of specific marker genes. Mainly the *O4*, *Mbp*, *galactocerebroside* or *SOX10* characterizes the mature oligodendrocytes (Nishiyama, 2009).

Oligodendrocytes are abundant in white matter but can also be found in gray matter, mostly intrafascicularly (Stadelmann et al., 2019). The main function of oligodendrocytes is the formation of myelin sheaths. Myelin sheaths are extended and modified plasma membranes spirally wrapped around the axon (Raine, 1984), whose main purpose is to promote rapid saltatory conduction and reduce axonal energy consumption (Huxley and Stampfli, 1949). Besides forming myelin, oligodendrocytes are also responsible for metabolic support to neurons via myelin sheaths (Fünfschilling et al., 2012, Lee et al., 2012), they play a role in immunomodulation (Kirby and Castelo-Branco, 2021) and there is growing evidence for their role in influencing the neuronal circuit functions (Monje, 2018, Forbes and Gallo, 2017).

Oligodendrocytes express a range of ion channels, neurotransmitter receptors and transporters. They are needed for sustaining ion and water homeostasis and metabolism, which are crucial conditions to maintain myelin and axon integrity (Butt et al., 2019). This, however, may not be their full potential. Heterogeneous expression of channels and receptors in oligodendrocytes and the physiological difference between cells found in gray and white matter suggests the existence of oligodendrocyte subpopulations with different physiological properties (Mangin et al., 2012).

1.2 Glia in Pathology

As described above, glia have a wide variety of physiological functions, hence it is only logical that they encounter changes during pathological states. A spectrum of molecular, cellular and functional changes that occur in response to CNS injuries and diseases is collectively termed reactive gliosis. The changes result in alterations of glia´s role through gain and/or loss of functions and the outcome can be either beneficial or detrimental to the organism.

Astrogliosis - a reaction of astrocytes, is classically accompanied by cellular hypertrophy and increased expression of the glial fibrillary acidic protein (GFAP) (Wilhelmsson et al., 2006, Hol and Pekny, 2015, Escartin et al., 2021). During severe tissue damage, individual reactive astrocytes can even overlap their processes and together with substantive proliferation and loss of individual astrocyte domain structures, create a dense and compact formation called glial scar (Sofroniew and Vinters, 2010). Glial scar serves as a neuroprotective barrier to inflammatory cells and infectious agents and besides tissue damage, it is formed alongside necrosis, infection or inflammatory infiltration (Herrmann et al., 2008, Sofroniew, 2009, Voskuhl et al., 2009).

From a molecular standpoint, many signaling molecules can trigger or regulate specific aspects of reactive astrogliosis in some way. Such molecules can be cytokines (e.g. IL6, TNF-α, IFNγ, Il10, TGF-β), LPS, neurotransmitters (e.g. glutamate), purines (e.g. ATP), reactive oxygen species (ROS), or products associated with neurodegeneration (e.g. β-amyloid) (Sofroniew, 2009). Any cell type in the CNS including neurons, microglia, oligodendrocyte lineage cells, pericytes, endothelia or even other astrocytes can release these, most likely in response to some form of CNS insult (Sofroniew, 2009).

Astrocytes display a portion of common features in response to various pathological stimuli, however; it seems that their reaction is far more heterogeneous and dynamic than was assumed (Batiuk et al., 2020, Bayraktar et al., 2020, Habib et al., 2020, Wheeler et al., 2020, Hasel et al., 2021, Sadick et al., 2022). Until recently, reactive astrocytes were only divided into neurotoxic (A1) and neuroprotective categories (A2), but with more reactive astrocyte populations identified (reviewed in (Matusova et al., 2023), it has been suggested to use rather multiple parameters including gene expression, proteomics, function and morphology instead of only a few marker genes to define a population (Matusova et al., 2023, Escartin et al., 2021). Therefore, the A1 and A2 division is currently used less and there is a rising endeavor to characterize astrocytes in greater detail.

Microgliosis is the term for a reaction of microglia, accompanied by characteristic features such as an increase in the cell count, cell body hypertrophy, and retraction of their processes (Li and Zhang, 2016). Over many years, reactive microglia were classified based on their pro- or anti-inflammatory profile as so-called M1 and M2 microglia, which is a system based on the classification of peripheral macrophages. Even though the terminology is slowly being abandoned for reasons discussed later in the chapter, some publications still use this nomenclature, therefore when citing such sources; the M1/M2 division will be kept. As aforementioned, homeostatic or resting microglia (also called M0) become activated through immune receptors and shift their profile to either M1 or M2 type. M1 microglia produce and release ROS, reactive nitrogen species (RNS) and cytokines such as TNF-α, IL-1β or IL-12 while M2 microglia on the other hand produce trophic factors, such as TGF-β and brain-derived neurotrophic factor (BDNF) (Tang and Le, 2016). Since M2 microglia induce anti-inflammatory reactions and neuroprotection (Colonna and Butovsky, 2017), promoting a polarization shift from M1 to M2 microglia was proposed as a potential therapeutic strategy in neurodegenerative diseases (Wen et al., 2017, Zhang et al., 2018). However, with more microglia-oriented studies, it seems that the heterogeneity and variability of microglia populations are larger than expected. Thus, although the potential microglia shift towards neuroprotective state might offer some benefits, it is not likely to be efficient as a stand-alone therapeutic approach.

Similar to the situation in astrocytes, the use of new technologies has revealed several microglia populations, suggesting that the activation profile of microglia is not black or white but more of a gray scale. Therefore, the M1/M2 nomenclature seems to be an oversimplification of microglia heterogeneity and variability and it has been suggested to consider more factors (e.g. age, location or sex) to create better microglia classification (Ransohoff, 2016, Martinez and Gordon, 2014, Paolicelli et al., 2022).

Oligodendrocytes are more susceptible to death during pathologies than astrocytes or microglia. In order to myelinate properly, they have a high metabolic rate creating toxic byproducts, that need to be properly metabolized (McTigue and Tripathi, 2008), they have low concentration of anti-oxidative enzyme glutathione (Thorburn et al., 1996) and also a high intracellular concentration of iron (Connor and Menzies, 1996). All these factors mentioned above make them very vulnerable to oxidative damage occurring e.g. during multiple sclerosis (MS) or ischemia. Their receptors make them vulnerable to glutamate toxicity and their death can also occur as a result of exposure to inflammatory cytokines (Bradl and Lassmann, 2010). The death of oligodendrocytes is connected to demyelination, which is a hallmark of some neurodegenerative diseases.

1.3 Amyotrophic Lateral Sclerosis

Amyotrophic lateral sclerosis (ALS) is a MN disease caused by MN degeneration in the motor cortex, brainstem, and spinal cord, which culminates in death, mostly from respiratory failure within three to five years from diagnosis. ALS occurs globally and there is some evidence the disease is increasing in incidence (Longinetti and Fang, 2019, Park et al., 2022). The primary mechanisms that drive the onset and progression of ALS are not completely understood, thus only symptomatic treatment with minimal benefit is currently available to patients.

Approximately five to ten percent of patients have a family history of ALS; hence this form is sometimes referred to as familial ALS (fALS) while the rest of the cases are called sporadic ALS (sALS). The disease is complex and has a monogenic cause in only 10 – 21 % of patients. In the majority of cases, it seems to be the interaction of multiple genetic and environmental risk factors are to blame (Mead et al., 2023). So far, the only confirmed epidemiological risk factors correlated to ALS development are male gender and age (Longinetti and Fang, 2019). A genetic cause has now been identified in 60 – 70 % of fALS patients (Ranganathan et al., 2020), but genetic factors also seem to be important in the absence of a family history. More than 30 genes either causative or associated with a higher risk of developing ALS have been identified, with four of them accounting for 70 % fALS cases – *chromosome 9 open reading frame 72 (C9orf72), superoxide dismutase (Sod1), TAR DNA binding protein (Tardbp), fused in sarcoma (Fus)* (Mead et al., 2023).

The key hallmark for all ALS cases is the loss of upper and lower MNs with denervation changes in muscles, in most patients also accompanied by TAR DNA-binding protein 43 (TDP-43) proteinopathy. There is, however, a certain pathological variability with ALS cases caused by the mutation of either *Sod1* or *Fus*, where the TDP-43 aggregates are not present**.** Other pathological mechanisms associated with the disease are oxidative stress, excitotoxicity, mitochondrial dysfunction, impaired protein homeostasis, impaired axonal transport and neuroinflammation (Filipi et al., 2020) (Fig. 5).

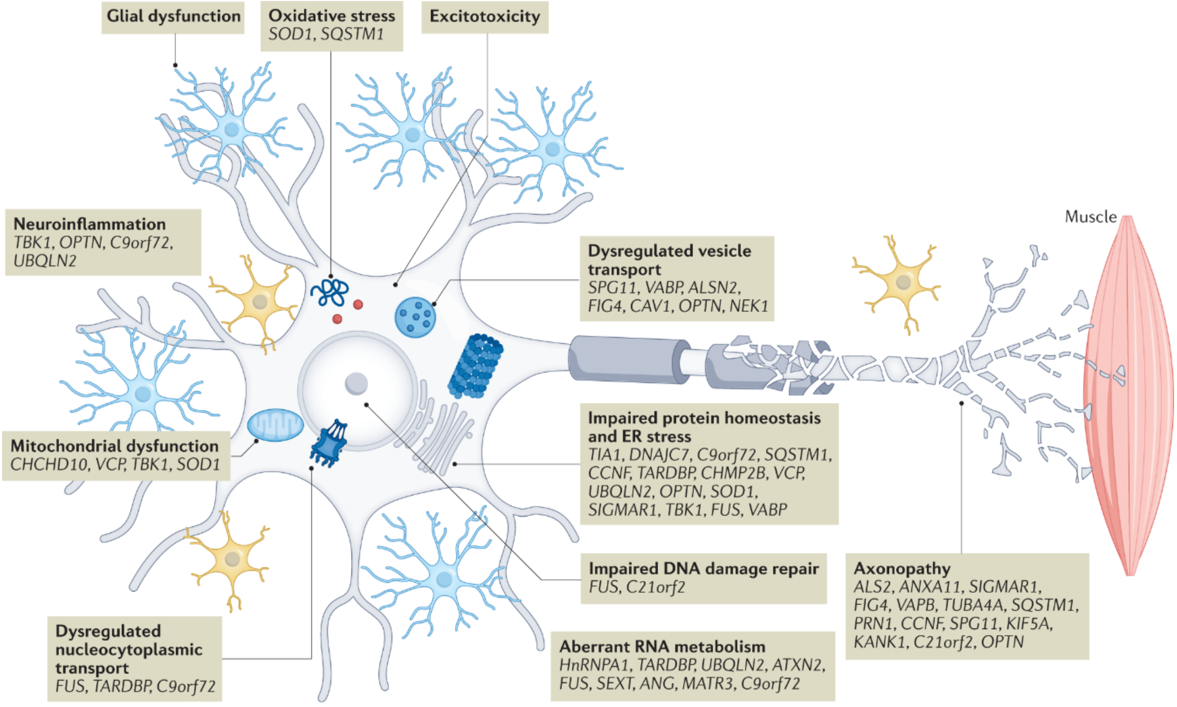

Fig. 5 Schema of key pathological processes associated with ALS and causative genes linked to those processes. Some of these mechanisms were described only recently owing to new genetic information. Some ALS-associated genes (e.g. *C9orf72*, *Tbk1*, *Fus*, *Tardbp*, *Optn*, *Ubqln2* or *Ataxn2*) were also described in closely related neurological diseases such as frontotemporal dementia. This suggests that some neurological disorders could share a pathological pattern to some extent. Indeed, many of the pathways are relevant in Alzheimer's disease (Mead et al., 2023).

For a long time, ALS was considered to exclusively affect motor neurons, however, it is now known that it affects also glial cells and that they have a role throughout the whole course of the disease prior to the onset. This was proven by the conditional deletion of mutated genes in individual glia populations, which slowed down the progression of the disease (Boillée et al., 2006, Kang et al., 2013, Yamanaka et al., 2008). Furthermore, implanting wildtype glia into an ALS animal model turned out to be beneficial and prolonged survival (Clement et al., 2003). Even though the exact role of glial cells in ALS has not yet been discovered at least some of the mechanisms and processes that can help with the overall understanding have been described in recent years.

Astrocytes become reactive during ALS and it seems that the first astrogliosis appears even before the symptom manifestation and MN degeneration (Howland et al., 2002a). The astrocytic activation during ALS has a dual effect. Firstly, it seems to restrict an ongoing inflammation by preventing infiltration of activated immune cells into surrounding tissues

(Faulkner et al., 2004). Secondly, the modifications of extracellular matrix that are a crucial part of reactive astrogliosis contribute to the inhibition of axonal regeneration and growth (Zamanian et al., 2012). ALS astrocytes also seem to affect the MN survival directly. Mutated SOD1 astrocytes from mice were shown to cause MN toxicity even before any reactive gliosis (Nagai et al., 2007) and astrocytes derived from sALS patients transplanted into the mouse also led to MN degeneration (Qian et al., 2017).

One of the proposed pathological mechanisms in ALS associated with astrocytes is excitotoxicity (Rothstein, 1996). A hypothesis emerged with information of increased glutamate concentration in sALS patients' cerebrospinal fluid early in progression (Van Den Bosch et al., 2006). The mechanism of glutamate excitotoxicity represents an excessive activation of neuronal glutamate receptors, causing calcium influx, resulting in apoptotic processes and eventual cell death. The EAAT2 transporter, responsible for the uptake of nearly 90 % of synaptic glutamate (Lauriat and McInnes, 2007), was found to be substantially decreased in ALS animal models (Bendotti et al., 2001, Bruijn et al., 1997, Howland et al., 2002b) (Fig. 6). The absence of the transporter and thus inadequate glutamate uptake could therefore contribute to MN death. However, when (Li et al., 2015) upregulated the GLT-1 in the mouse spinal cord via intraspinal delivery at disease onset, it failed to protect phrenic MNs and extend the animal lifespan. (Battaglia et al., 2015) enhanced GLT-1 expression in the spinal cord and even though they were able to rescue MNs, they did not manage to extend the lifespan. These results suggest that the impaired glutamate uptake affects motor neurons most likely prior to disease onset, and even though the restored level of GLT-1 can help to rescue MNs, it is not sufficient to prolong survival.

Another mechanism connected to astrocytes in ALS is called the non-cell autonomous effect and it has an impact on neuronal survival. The process is mediated by astrocyte-specific soluble factors (IL-6, CXCL1, 10 and 12, TNF-α or TGF-β1) that are upregulated in ALS astrocytes and secreted to the surrounding tissue. This causes changes in MNs morphology, specifically smaller cellular bodies, shorter axons, and axonal swelling (Bruijn et al., 1997, Tripathi et al., 2017). Besides neurons, the soluble factors from astrocytes also affect the functioning of other cell types e.g. microglia and regulate their immunological response (Ouali Alami et al., 2018).

In addition to their impact on neurons, many studies confirmed that astrocytes themselves have perturbed intracellular processes (Fig. 6). There are multiple reports of transcriptional deregulation of an immune response, lysosomal and phagocytic pathways or ion and cholesterol homeostasis (Baker et al., 2015, Miller et al., 2018). Downregulation of K^+

channel $K_{ir}4.1$ expression was detected in both SOD1 patients and rats (Kelley et al., 2018, Bataveljic et al., 2012) and murine SOD1 astrocytes were shown to have abnormal intracellular Ca^{2+} dynamics (Kawamata et al., 2014). The perturbation of the homeostatic function of astrocytes could thus be an important factor during ALS.

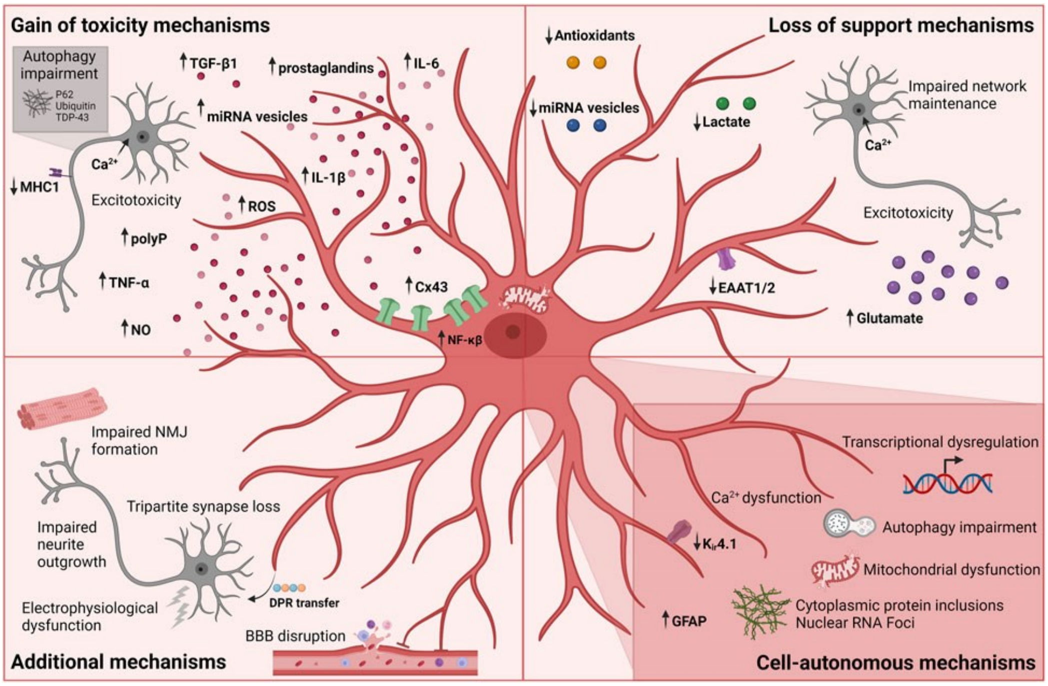

Fig. 6 Summary of proposed pathological mechanisms concerning astrocytes and playing a role in ALS. Astrocytes can become toxic to neurons by gaining or losing functions (e.g. production of ROS and nitric oxide (NO), impairment of glutamate and lactate homeostasis) by cell-autonomous mechanism (e.g. Kir4.1 downregulation or Ca^{2+} dysfunction) and others, such as BBB disruption (Stoklund Dittlau et al., 2023).

Microglia, in the same way as astrocytes, become activated during ALS, and their association with the disease has been known for a while (Fig. 7). (Hall et al., 1998) described some proinflammatory microglia detected in the mouse spinal cord prior to disease onset, whose number increased with the disease progression and persisted into the end-stage. When the activation was reduced via the inhibition of colony-stimulating factor 1 receptor (CSFR1) protein, it extended the survival of mice (Martinez-Muriana et al., 2016).

When it comes to the exact role of microglia and especially their heterogeneity during ALS, there is some contradiction. Originally, microglia´s contribution was thought to be important mostly later during the disease progression, as the removal of the mutated gene from microglia caused lengthening of lifespan, but did not affect the onset point (Boillée et al., 2006). Studies from Tang and Le (2016) and Gordon et al. (2003) on SOD1(G93A) mice described that microglia at first act more in an anti-inflammatory manner. They activate myeloid cells by releasing cytokines with anti-inflammatory activities such as IL-4, IL-10, and IL-13. Moreover, they also express neurotrophic factors such as BDNF. (Beers et al., 2011) found upregulation of the M2 profile marker genes for chitinase-like 3 (*Ym1)* and mannose receptor (*CD206)* in the spinal cord, which supports the idea of the early anti-inflammatory phenotype. Eventually, near the final stage of the disease, microglia from SOD1(G93A) mice seem to develop pro-inflammatory phenotype, starting to exhibit phagocytic activity and produce pro-inflammatory mediators, including ROS, NO, IL-1β, IL-6, TNF-α (Liao et al., 2012) (Fig. 7) and also have upregulated expression of M1 prototypic marker NADPH oxidase 2 (NOX2) (Beers et al., 2011).

Data from (Chiu et al., 2013) who analyzed transcriptomic profiles of ALS microglia and revealed significant induction of potentially neuroprotective and neurotoxic factors occurring concurrently, on the other hand challenge the idea of a microglial shift from M2 to M1. Moreover, a study from (Maniatis et al., 2019) using spatial transcriptomic in mouse spinal cord showed that changes in microglial expression precede changes in MNs, and another study showed a decreased number of microglia before onset (Gerber et al., 2012). These findings thus suggest the involvement of microglia rather early in the disease process.

In pursuit of better microglia characterization, (Keren-Shaul et al., 2017) used single-cell RNA sequencing and described a novel population called disease-associated microglia (DAM). The population was originally described in a mouse model of Alzheimer´s disease, but they detected these microglia also in the spinal cord of SOD1(G93A). The DAMs are activated by a two-step process and have a unique RNA signature. They downregulate homeostatic genes like *Cx3Cr1* and *P2ry12* and simultaneously upregulate *Trem2, Tyrobp*, *Lpl* and *Cst7*, genes linked to inflammation, phagocytic and lipid metabolism pathways. It seems that this subpopulation could be associated with the clearance of the aggregates often accumulating during neurodegeneration, and the authors suggest that blocking microglia-specific checkpoints could be used therapeutically (Keren-Shaul et al., 2017, Yerbury et al., 2016).

One of ALS hallmarks involving microglia is inflammation. Nuclear factor kappa-light-chain-enhancer of activated B cells (NF-κβ) protein is a key regulator of the inflammatory pathway and is known to be upregulated in the patient's spinal cords (Frakes et al., 2014). The reduction of NF-κβ in SOD1(G93A) mouse microglia resulted in extended survival. Constitutive activation, alternatively, caused microgliosis and death of MNs *in vitro* and *in vivo* (Frakes et al., 2014), proving that inflammation has an important role in the progression.

Nevertheless, the exact trigger or specific mechanism causing the NF-κβ upregulation is not clear.

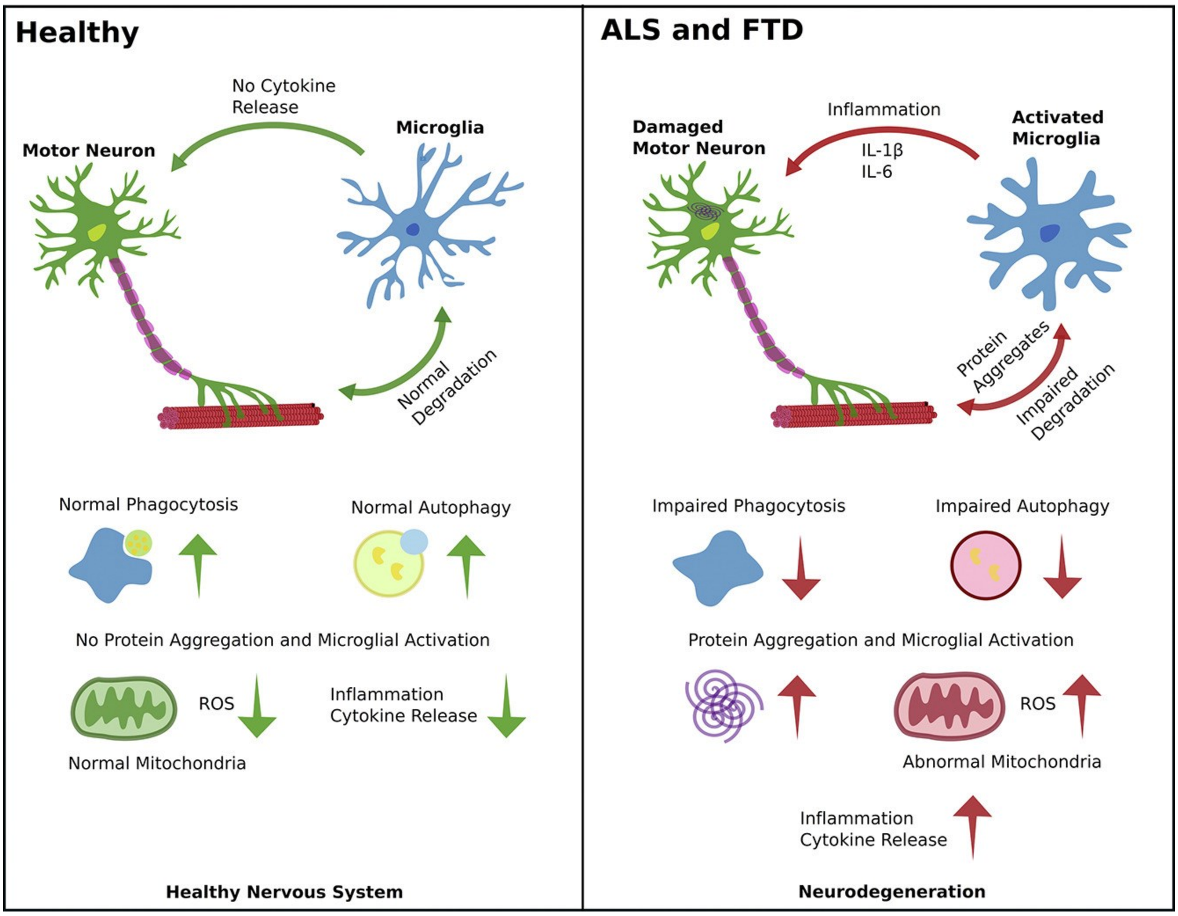

Fig. 7 Interaction of microglia and MNs in the ALS compared to their functioning in a healthy environment. In ALS, microglia are activated, they secrete proinflammatory cytokines and their ability to phagocyte is impaired. This, among others, leads to protein aggregation. Mitochondrial dysfunction then causes the production of ROS and thus further inflammation leading to further neurodegeneration (Haukedal and Freude, 2019).

Oligodendrocytes, unlike astrocytes and microglia, do not have active and resting forms; nevertheless, ALS still affects them in various manners (Fig. 8). In the mutant mice, the degenerating oligodendrocytes had a characteristically thickened cell body, they showed immunopositivity for the marker of apoptosis cleaved caspase-3 (CC3) and were surrounded by clusters of activated microglia (Kang et al., 2013, Philips et al., 2013). Demyelination of MN axons was reported in the spinal cords of both SOD1(G93A) mouse and ALS patients. Consistently, myelin basic protein (MBP) levels were reduced in the spinal cord of SOD1(G93A) mice (Philips et al., 2013). In the mouse model, the degeneration of oligodendrocytes precedes motor neuron death and visible symptoms, such as muscle weakness, twitching or cramping (Zeis et al., 2016, Peferoen et al., 2014) and OPC proliferation in the spinal cord is not sufficient to compensate for the loss of mature oligodendrocytes (Bonfanti et al., 2020). Oligodendrocytes are not only passive sufferers in the pathology and the impairment of their physiological functions can influence the progression.

One mechanism associated with oligodendrocytes potentially affecting the MNs is the impairment of glucose and lactate shuttling. Oligodendrocytes express connexins that enable the diffusion of small molecules including glucose and connexins 32 and 47 predominantly expressed on the oligodendrocytes membrane, which turned out to be downregulated in the anterior horn of ALS transgenic mice (Cui et al., 2013). The monocarboxylate transporter 1 (MCT1), a vital transporter for lactate, which is physiologically in the myelin sheath around axons (Rinholm et al., 2011) was deficient in the spinal cord of mice and the motor cortex of patients (Lee et al., 2012). Insufficiency of intercellular glucose and lactate trafficking could result in energy deficiency in MNs and exacerbate their degeneration. Beside dysregulation of energy metabolism, alterations in myelin lipid composition were identified in SOD1(G93A) animals (Niebroj-Dobosz et al., 2007), suggesting that lipid production may be impaired.

Neuroinflammation, which was mentioned earlier concerning microglia, can also affect the functioning of oligodendrocytes. Proinflammatory cytokines, such as TNF lead to OPC damage and prevent them from maturing (Lim et al., 2016, Jana and Pahan, 2005). (Deng et al., 2014) showed that IL-1β could induce apoptosis and hypomyelination. However, they are not just victims, but can actively participate in the inflammatory processes (Gong et al., 2022). They can react to inflammation through the expression of cytokines, inflammasomes and chemokines, which make them, along with astrocytes and microglia, active in the neuroinflammatory network (Zeis et al., 2016).

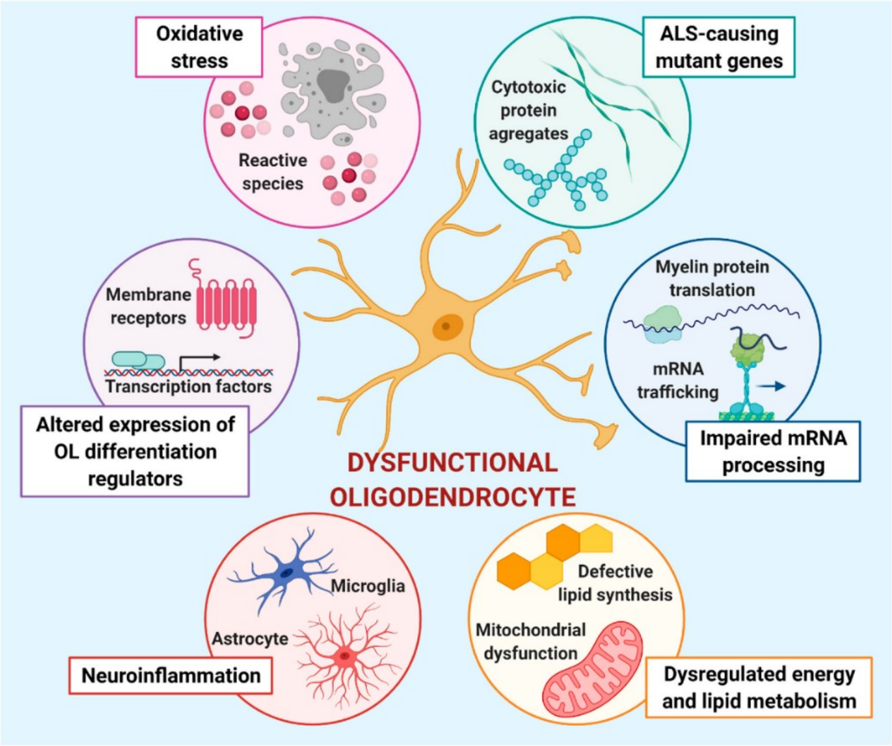

Fig. 8 Overview of the mechanisms contributing to oligodendrocyte dysfunction in ALS. The presence of mutant genes in oligodendrocytes causes issues with mRNA processing resulting in impaired trafficking and translation of myelin-related mRNAs. The other factors influencing the oligodendrocyte functioning are neuroinflammation that prevents maturation, impaired lipid metabolism resulting in different myelin lipid composition and oxidative stress (Raffaele et al., 2021).

1.4 Animal Models of ALS

A general limitation of ALS studies on patients is usually the small number of cases. Furthermore, glial cells change their gene expression during aging (Soreq et al., 2017) and thus the different ages of patients enrolled in such studies could cause bias in the result. Moreover, to thoroughly investigate the pathology, studies mostly rely on the usage of post-mortem tissue, and thus can only provide data from the final stage of the disease. To overcome these issues, research relies heavily on animal models.

ALS animal models are majorly based on the known mutations of causative genes. The first identified gene was in the *SOD1* (Rosen et al., 1994, Rosen et al., 1993) and based on this discovery, (Gurney et al., 1994) generated the first ALS animal model. This model is based on overexpression of the mutant form of human *SOD1* and there are currently many models available, with different mutations in this particular gene. All develop progressive MN degeneration, and a phenotype similar to patients, varying in the onset time point as well as the progression rate. Other characteristic features that were identified in patient samples are also present in the model, suggesting that these mice can be a useful tool in studying ALS pathology. Most studies using the SOD1 model have focused on the pathological processes in the spinal cord and less is known about the motor cortex. There is a debate as to what extent is the cortex affected in this particular model, hence what is the actual relevancy to human pathology. The few existing studies exploring the pathology in the cortex showed contradictory results (Gomez and Germain, 2019, Miller et al., 2018, Rodriguez-Gomez et al., 2020, Niessen et al., 2006).

The other known causative genes have also led to the creation of animal models. The most known are TDP-43 and C9ORF72. The TDP-43 model is based on mutation in the *TARDBP* gene, which is involved in RNA processing and modifications. These animals also exhibit progressive motor dysfunction, astrogliosis and in addition cytoplasmic inclusions positive for TDP-43 and ubiquitin (Tsao et al., 2012). The C9ORF72 animal models are much desired because the excessive hexanucleotide (GGGGCC) repeat expansion in the first intron of C9ORF72 is responsible for approximately 40 % of fALS cases (DeJesus-Hernandez et al., 2011). However, only a few transgenic animals that exhibit ALS symptoms such as motor deficit and neurodegeneration have been developed so far (O'Rourke et al., 2015, Liu et al., 2016).

1.5 Alzheimer´s Disease

Alzheimer´s disease (AD) is a progressive neurodegenerative disorder affecting an ever-increasing number of people and is the main cause of dementia (Scheltens et al., 2021). The degeneration strikes mainly in the prefrontal, entorhinal cortex and hippocampus, which are structures associated with learning and memory, and further linked to the limbic system, thus cognitive and emotional processes (Minati et al., 2009, Kulijewicz-Nawrot et al., 2012). This translates into characteristic symptoms such as memory and learning impairment, apathy, depression, changes in behavior and later on impairment of complex attention, language and even hallucinations, delusions or aggression (Lyketsos et al., 2011, Long and Holtzman, 2019). Most cases occur after age 65, but in some cases, the onset can be early. That is often the case with inherited AD, which is, beside very early onset, accompanied by rapid progression and sometimes also with other neurological symptoms rarely present in sporadic AD (Bateman et al., 2012).

The overall understanding of AD pathology is still incomplete; however, over the years that AD has been studied some biological hallmarks related to neurodegeneration have been identified. These comprise extracellular accumulation of amyloid β (Aβ) in the form of diffuse plaques, tau accumulation as intraneuronal neurofibrillary tangles (NFTs), in the dendrites as threads of neuropil and as senile plaques in axons (Duyckaerts et al., 2009), glial pathology, disruption of ion homeostasis and others (Fig. 9).

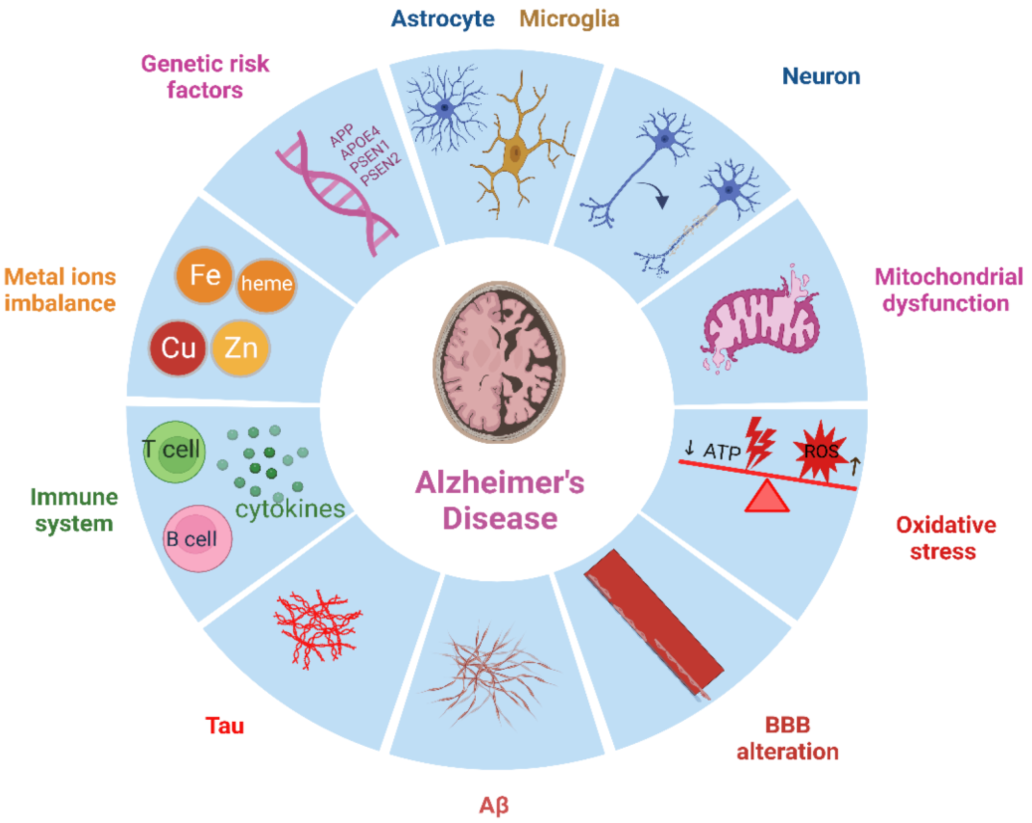

Fig. 9 Depiction of factors involved in Alzheimer´s disease. Besides the well-established tau and aβ pathology, there is also an impairment of BBB integrity. This can lead to neuroinflammation via an influx of peripheral immune cells to the brain. Related to that, the glial cells react to all this, especially microglia and astrocytes that become activated. Associated with astrocyte dysfunction is the imbalance of ions and following mitochondrial dysfunction can lead to eventual oxidative stress (Afsar et al., 2023).

Aβ is produced by the cleavage of β-amyloid precursor protein (APP) by β-secretase and γ-secretase. The Aβ peptides then aggregate into protofibrils and fibrils, which are detectable in the AD brain (Long and Holtzman, 2019). (Hardy and Higgins, 1992) proposed the amyloid cascade hypothesis, stating that the Aβ accumulation is the first step of AD pathology consequently followed by tau accumulation, neuronal loss and cognitive decline. Parts of the hypothesis have been supplemented and revised, but it has been considered a leading model of AD pathogenesis since first posited. It was, among others, supported by the discovery that a rare APP mutation, which reduces the risk of AD development, causes a decrease in Aβ production (Jonsson et al., 2012, Martiskainen et al., 2017). Although the evidence supports the role of Aβ aggregation in promoting the AD cascade, there is minimal relation between amyloid accumulation and degree of cognitive decline (Nelson et al., 2012) or between regions with cerebral amyloid plaques and regions showing hypometabolism on functional neuroimaging (Altmann et al., 2015). Despite years of research, no Aβ-targeting therapy has yet successfully limited the progression of cognitive impairment in symptomatic AD. This suggests that the Aβ deposition might be crucial at the onset of the disease, while other joint processes such as inflammation and tau deposition may drive its actual progression (Long and Holtzman, 2019).

Tau accumulation is another hallmark of AD and a potential driver of neurodegeneration. The protein is coded by microtubule associated protein tau (*MAPT)* gene and primarily expressed by neurons. The physiological role of tau is not fully understood, but several *in vitro* studies reported its role in microtubule assembly, microtubule transport and stabilization of neural axons (Dixit et al., 2008, Weingarten et al., 1975). Tau is post-translationally modified by phosphorylation and acetylation in particular (Marcelli et al., 2018), which can affect the pathology (Hoover et al., 2010, Min et al., 2010, Cook et al., 2014). Unlike Aβ, the tau pathology stage correlates with the cognitive impairment progression (Giannakopoulos et al., 2003, Nelson et al., 2012).

An increasing number of studies now show that besides the above described hallmarks, the AD pathological mechanism also involves glial cells. Reactive astrogliosis and microgliosis are well established pathological features in the AD brain (Long and Holtzman, 2019). Microglia, having a phagocytic role and being able to degrade Aβ were first thought to have a neuroprotective role in AD. Other studies suggested that their role is more dependent on the stage of the disease and that they react to the rate of inflammation caused by Aβ and other changes in the microenvironment. This is in agreement with (Kim and Factora, 2018), who showed that microglia recruited to senile plaques seem to be unable to recognize and degrade Aβ in aged mice. (Felsky et al., 2019) recently published a detailed morphological analysis of microglia from postmortem cortical tissue and found out that the proportion of morphologically activated microglia (PAM) correlates with Aβ deposition, tau-related pathology and the rate of cognitive decline, which also supports the idea of microglia being directly affected by Aβ caused inflammation. Based on a study from (De Strooper and Karran, 2016), changes in microglia and astrocytes can even drive the progression before any cognitive impairment appears, which stresses the importance of their role throughout the disease.

In the last few years, a fair number of transcriptomic studies focusing on microglia and their role in AD have been published. This led to the discovery of several cell populations characterized by a unique expression profile. One of those are DAM (discussed earlier), which were discovered close to neuritic plaques by (Keren-Shaul et al., 2017). Other revealed populations are activated response microglia (ARM) and interferon response microglia, which were discovered in the cortex and hippocampus of an AD mouse model. While ARMs overexpress MHC type II, genes associated with tissue repair (*Dkk2, Gpnmb* and *Spp1*) and are highly enriched with AD risk genes, interferon responsive microglia (IRM) upregulate genes *Ifit2, Ifit3, Ifitm3, Irf7* or Oasl2, which are associated with an innate immune response and interferon type I response pathways (Sala Frigerio et al., 2019).

Back in 1910, A. Alzheimer described pathologically modified astrocytes and discovered that glia are abundant near neuritic plaques (Tagarelli et al., 2006). Later on, astrogliosis became known as a typical morphological feature of AD brains and was detected in human patients as well as in AD animal models (Nagele et al., 2004, Nagele et al., 2003, Rodriguez et al., 2009, Olabarria et al., 2010). Astrogliosis in AD can be triggered by surrounding neurons and glia or by the Aβ plaques. Aβ seems to affect also the physiological properties of astrocytes. Cultured astrocytes exposed to Aβ reacted by spontaneous calcium signaling and calcium oscillations that contributed to their neurotoxicity (Abramov et al., 2003, Abramov et al., 2004). Furthermore, the homeostatic functions of astrocytes are impaired, affecting the glutamate and overall ion homeostasis and leading to an increased release of glutamine, GABA, cytokines and inflammatory mediators (Ben Haim et al., 2015, Hynd et al., 2004).

More recently, (Habib et al., 2020) published a key study characterizing astrocyte reactivity in AD from the point of gene expression. They analyzed the hippocampus of AD mice using single-nucleus RNA-sequencing and were the first to describe a population of so-called diseased-associated astrocytes (DAA). The DAA were similar to the Gfap-high astrocyte population present in control animals, however, they specifically upregulated genes connected to endocytosis, aging, complement and amyloid metabolism. They appeared early during the disease and their number increased with progression. A similar population was then also identified in aged human and mouse brains suggesting that it is not specific to a particular AD model or brain region.

2 AIMS OF THE STUDY

Hypothesis 1.: Cortical glial cells are affected by the ALS pathology in patients, however, the data from the SOD1(G93A) mice model are contradictory. Some studies reported a decreased number of neurons and signs of gliosis (Miller et al., 2018, Gomes et al., 2019, Migliarini et al., 2021), while others suggested that the cortical pathology is limited to the spinal cord (Niessen et al., 2006). We hypothesize that the changes in cortical glia may be minimal and thus difficult to detect. Therefore, the use of advanced methods such as sequencing on a single-cell level can bring better insights into the discussion.

Aim 1.: To assess the extent to which cortical glia are affected by the ALS-like pathology in the SOD1(G93A) model of ALS.

Hypothesis 2: Multiple studies describe the potential pathological or neuroprotective roles of astrocytes in ALS (reviewed in You et al. (2023)). However, despite astrocytes being the primary homeostatic cells in the CNS, there is insufficient information about their homeostatic functions throughout the disease progression. Although there are reports of potassium channel downregulation in the SOD1(G93A) model, studies on the functional impact of this downregulation are lacking. Additionally, potential discrepancies exist between animal models with different genetic backgrounds. We hypothesize that the pathology impairs the ability of astrocytes to maintain ion homeostasis, which in turn can influence the CNS environment and disease progression.

Aim 2.: To unveil the astrocytic capacity to regulate ion homeostasis in the cortex and spinal cord of SOD1(G93A) model on the FVB/N background.

Hypothesis 3.: Under pathological conditions, the ion concentration in the ECS increases significantly (Pasantes-Morales and Vazquez-Juarez, 2012). Astrocytes physiologically sustain ionic/neurotransmitter homeostasis; however, like other cell types, aging can cause a loss/alteration of their normal functions (Palmer and Ousman, 2018). Such change can then add to the progression of AD. We hypothesize that the ability of astrocytes to regulate their volume will decline with age and the progression of AD. Related to that, we expect changes in the composition and structure of the extracellular matrix (ECM) associated with changes in astrocytic volume and morphology. Analysis of astrocytes and ECM at different time points throughout the AD progression will shed more light on aging as an additional risk factor contributing to the disease.

Aim 3.: To characterize the astrocytic ability to control ion uptake and characterize the extracellular composition in the AD mouse model.

3 MATERIALS AND METHODS

3.1 Materials and Methods Common for Aims: 1, 2 and 3

3.1.1 Animals

All experiments involving laboratory animals were performed in accordance with the European Communities Council Directive 24 November 1986 (86/609/EEC) and animal care guidelines approved by the Institute of Experimental Medicine, Academy of Sciences of the Czech Republic (Animal Care Committee (approval number 40/2019). All animals used for experiments were sacrificed using pentobarbital followed by decapitation. To prevent unnecessary suffering during the advanced stage of the disease, mutant mice were euthanized using carbon dioxide shortly after reaching five months of age. All efforts were made to minimize the number of animals used.

For assessing the state of glial cells in the motor cortex of the SOD1(G93A) mouse model, we used transgenic mice expressing high levels of human SOD1(G93A) (JAX Strain: 004435 C57BL/6 J-Tg (SOD1*G93A)1Gur/J) and their non-carrier littermates (Gurney et al., 1994). This strain contains ~ 25 copies of the transgene, and its 50% survival ranges 157 ± 9.3 days (jax.org/strain/004435).

To evaluate the functional properties of astrocytes, we used a transgenic mouse on FVB/N background with fluorescently labeled astrocytes, expressing high levels of human SOD1(G93A). As a control, we used their non-carrier littermates. To generate the mouse, we crossbred C57Bl/6J-Tg (SOD1*G93A)1Gur/J (JAX Strain: 004435) males and GFAP/EGFP (Nolte et al., 2001) females. A visualization of astrocytes in GFAP/EGFP mice is feasible due to the expression of enhanced green fluorescent protein (EGFP) under the control of the human glial fibrillary acidic protein (GFAP) promoter. To obtain the congenic strain, mice were backcrossed to a FVB/N background for at least 10 generations. These animals are further termed as SOD1/GFAP/EGFP and CTRL/GFAP/EGFP.

For the analysis of astrocytes in an AD model, we generated a triple transgenic model of AD with fluorescently labeled astrocytes by crossbreeding mice that contained three mutations associated with familial AD (APP Swedish, MAPT P301L, and PSEN1 M146V) (Oddo et al., 2003) with GFAP/EGFP mouse strain (Nolte et al., 2001). These hybrids (further referred to as 3xTg-AD) enabled the visualization of astrocytes for the use of morphological studies due to the enhanced green fluorescent protein (EGFP), expressed under the control of the human glial fibrillary acidic protein (GFAP) promoter. We worked with 3, 9, 12 and 18-month-old animals (3M, 9M, 12M, and 18M).

3.1.2 Immunohistochemistry

For immunohistochemistry, the animals were deeply anesthetized with pentobarbital (PTB) (100 mg/kg, i.p.) and transcardially perfused with 20 ml of saline solution with heparin (2500 IU/100ml; Zentiva) followed by 20 ml of cooled 4% paraformaldehyde (PFA) in 0.1 M phosphate buffer saline (PBS) and decapitated. The brains and spinal cords were dissected and post-fixed overnight with PFA and treated with a sucrose (Sigma-Aldrich) gradient (ranging from 10 to 30%) for cryoprotection. Coronal 30-μm-thick slices were prepared using a cryostat (Hyrax C50, Zeiss). For the staining, the slices were washed in a PBS followed by blocking of the nonspecific binding sites with 5% Chemiblocker (Millipore, Billerica, MA), and 0.2% Triton X-100 (Sigma-Aldrich) in PBS for 1 hour. The blocking solution was also used as the diluent for the antisera. The slices were incubated with the primary antibodies overnight, and the secondary antibodies were applied for 2 h at 4–8 °C. The primary antibodies used throughout all experiments can be found in Table 1.

Tab. 1 A list of antibodies used for the immunohistochemical analysis

Targeted cell type/structure	Antibody	Species	Dilution	Company
Myelin	MBP	rat	1:500	Biorad
Microglia	Iba-1	rabbit	1:500	Abcam
Apoptotic cells	CC-3	rabbit	1:50	CellSignaling
Oligodendrocytes	APC	mouse	1:200	Merck
Astrocytes	ALDH1L1	rabbit	1:500	Abcam
Kir4.1 channel	Kir 4.1	guinea pig	1:300	Alomone

The secondary antibodies were goat anti-rabbit IgG, goat anti-mouse or chicken anti-rat IgG conjugated with Alexa Fluor 488 (1:500, Invitrogen, Waltham, MA, US) and goat anti-guinea pig conjugated with Cy3 (1:200, Chemicon, Temecula, CA, US). Cell nuclei were visualized by DAPI staining (Merck, Darmstadt, Germany).

3.1.3 Image Analysis

All analyses were done using FIJI image processing software (ImageJ 2.9.0/1.53t) (Schindelin et al., 2012). For the brain slices, confocal images (212 × 212 × 30 μm) were taken from coronal slices (1 mm and 2 mm from bregma), covering the area of the primary and secondary motor and the primary somatosensory cortex (five to six zones per hemisphere). For the spinal cord slices, confocal images (212 × 212 × 30 μm) stitched into tile scans were used, covering the area of the ventral horns. Only slices from the lumbar part of the spinal cord were used.

To quantify the morphology of astrocytes in the SOD1(G93A) model, ALDH1L1 fluorescence intensity was used. We analyzed six animals per group, two slices from each mouse. The thresholding method (Yen method) was used to filter out the background. The mean integrated density limited to the threshold for each animal was calculated.

To quantify the morphology of cortical and spinal astrocytes in the SOD1/GFAP/EGFP mice, we took advantage of their EGFP-labeling. Segmentation was done by thresholding the EGFP channel and the fluorescence-positive area was measured and related to the area of primary and secondary motor and primary somatosensory cortex or spinal ventral horn area. The area corresponding to EGFP reflects the increased number of GFAP-expressing cells and the enlargement of astrocytic soma and the thickening of their processes. A similar segmentation thresholding approach was used also for the Kir4.1 antibody signal. The immunopositive regions were segmented using the threshold dialog and the mean gray values were calculated in the segmented area.

To quantify the morphological changes of microglia, we conducted Sholl analysis on IBA1 positive cells using Sholl analysis plugin (Ferreira et al., 2014) for ImageJ. Six animals per group and two brain slices from each animal were used. For each brain slice, a minimum of eight cells were analyzed. For the Sholl analysis, the consecutive z-stack images were converted to maximum intensity projection and the projection was a thresholder for creating a binary mask. The number of intersections starting from 5 μm from the center of the soma, with a radius step size of 5 μm was measured.

To quantify the adenomatous polyposis coli (APC) and CC3-positive cells, three animals for each group and one slice (1 mm from bregma) from each animal were used for the analysis. The number of APC or CC3-positive cells was determined from superimposed images and expressed as the percentage of marker-expressing cells from the total number of DAPI-positive cells. The percentage of apoptotic cells was then expressed as a ratio of CC3-positive to the previously counted APC-positive cells.

For the analysis of MBP staining, we employed an Olympus FV10i confocal microscope equipped with × 60 oil objective. We used six animals per group and two slices from each animal and scanned 12 zones within each hemisphere. MBP expression density was determined using a custom-written FIJI (ImageJ) macro (available at: https://github.com/jakubzahumensky/JT_paper). In brief, to keep the dimensionality of analyzed images equal, the macro extracted a substack of the 20 brightest frames from each z-stack. This was followed by creating a binary mask of the fibers in each frame and measurement of the frame fraction covered by the mask. Within each sub-stack, the mean of this value was calculated, resulting in the volume fraction taken up by the fibers.

3.2 Materials and Methods Common for Aims 1 and 2

3.2.1 Behavioral Testing

We conducted two types of motor tests - the wire grid hang test and the Rotarod test (Mouse RotaRod NG 47650, Ugo Basile, Italy) to assess muscle strength, function, and coordination throughout the disease. Testing consisted of one three-attempt session for each test every week, beginning at 30 days of age, and lasting for 14 weeks. All animals performed training beforehand. Data are presented as mean or mean ± standard error of the mean (SEM) for n animals. Repeated measures two-way ANOVA with Holm-Sidak's multiple comparison correction was used to analyze the differences between the groups.

During the wire grid hang test the mouse was placed on a custom-made wire lid, approximately 60 cm above a wood chip covered bottom, and the lid was turned upside down. We measured the latency to fall. At the beginning of a testing period, each mouse was trained three consecutive times for at least 180 s. In the experimental session, the mouse had three attempts to hold on to the lid and the best score out of the three with a maximum of 180 s was noted.

The Rotarod testing consisted of placing the mouse on a stationary rod against the direction of rotation. The rod rotation was set to a constant speed of 15 rpm, and we measured the latency to fall. Each mouse was trained three consecutive times of at least 180 s at 5, 10 and 15 rpm speed beforehand. In the experimental session, the mouse had three attempts to remain on the rod. We noted the best score out of the three with a maximum of 180 s.

3.3 Materials and Methods Common for Aims 2 and 3

3.3.1 Preparation of Acute Brain and Spinal Cord Slices

Mice were deeply anesthetized with PTB (100 mg/kg, i.p.), and perfused transcardially with a cold (4–8°C) isolation buffer. Brains and/or spinal cords were dissected and placed into a cold isolation buffer (4–8 °C), oxygenated with Carbogen. The spinal cord was then embedded into the low-melting agarose (Sigma-Aldrich). Brain and spinal cord coronal slices of thickness 300 μm were used for 3D-morphometry and those of 400 μm for the TMA method. They were cut using an HM650 V vibratome (MICROM International GmbH, Waldorf, Germany). The slices were then incubated for 40 minutes at 34 °C in the isolation solution. After the incubation period, the slices were kept at room temperature (23–25 °C) in artificial cerebrospinal fluid (aCSF).

3.3.2 Experimental Solutions

The compositions of all used experimental solutions are listed in Table 2. All solutions were equilibrated with 95% O2 and 5% CO2 (Carbogen, Siad, Branany, Czech Republic) to a final pH of 7.4, while the osmolality was measured using a vapor pressure osmometer (Vapro 5520, Wescor, Logan, USA).

Tab. 2 Content of experimental solutions.

Compounds	aCSF [mM]	Isolation solution [mM]	20mM $aCSF_{K+}$ [mM]	50mM $aCSF_{K+}$ [mM]	$aCSF_{H\text{-}100}$ [mM]
NaCl	122	-	105	75	67
NMDG	-	110	-	-	-
KCl	3	2.5	20	50	3
$NaHCO_3$	28	24.5	28	28	28
Na_2HPO_4	1.25	1.25	1.25	1.25	1.25
Glucose	10	20	10	10	10
$CaCl_2$	1.5	0.5	1.5	1.5	1.5
$MgCl_2$	1.3	7	1.3	1.3	1.3
Osmolality (mOsmol/kg)	~300	~300	~300	~300	~200

3.3.3 Three-dimensional Confocal Morphometry

Time-dependent changes in astrocytic volume and morphology were studied using 3D-confocal morphometry in the motor cortex, the CA1 region of hippocampus and in the ventral horns of spinal cord. Brain or spinal cord slices were carefully placed into the recording chamber and mounted on the stage of a confocal microscope. The slices were held down with a U-shaped platinum wire with a grid of nylon threads. The recording chamber was continuously perfused with recording solutions (aCSF, $aCSF_{H\text{-}100}$ or $aCSF_{K}^{+}$) via a peristaltic pump PCD 31.2 (Kouril, Kyjov, Czech Republic) at a rate of ~7.5 mL/min. The exchange of solutions in the recording chamber took 2 minutes. All measurements were performed at room temperature.

The measurements in the hippocampal slices were carried out as previously described in Chvatal et al. (2007a), Chvatal et al. (2007b). The cells were captured as a series of two-dimensional (2D) sectional images with a resolution of 1024 × 1024 pixels, using an FV1200MPE confocal microscope equipped with a 60× LUMPLFLN water immersion objective (Olympus). EGFP was excited using an Ar laser at 488 nm, and the emitted signal was collected over the range of 488 nm with a DM405/488 filter. Each 3D image of the cell was composed of 65 to 85 sequential 2D images, spaced evenly at 1µm intervals. To prevent the inclusion of damaged cells, especially those with partially damaged processes near the slice surface, we selected cells with processes emerging 20 to 30 µm beneath the surface, as described in our previous work (Benesova et al., 2009).

Image processing and morphometric analysis were conducted using Cell Analyst software, developed at the Department of Cellular Neurophysiology, Institute of Experimental Medicine, Prague, Czech Republic (Chvatal et al., 2007a, Chvatal et al., 2007b). For each time point, four to five mice were used, with two to three slices prepared from the hippocampus of both hemispheres. These half-slices were used for volume quantification of one or two EGFP-positive cells. Changes in total astrocytic volume are reported as mean ± SEM. Statistical significance was assessed using a two-way ANOVA with Tukey's post hoc test. Differences between groups were considered statistically significant when $p < 0.05$, very significant when $p < 0.01$, and extremely significant when $p < 0.001$.

Cortical and spinal cord slices were measured using the protocol described in-depth by Awadova et al. (2018), Pivonkova et al. (2018). Fluorescence images were acquired on a multiphoton laser scanning microscope FV1200MPE (Olympus) with 60× LUMPLFLN water objective (NA = 1.0, WD 2 mm). EGFP fluorescence was excited in a 2-photon absorption mode at 950 nm by a tunable Ti-Sapphire laser system MaiTai DeepSee (Spectra Physics, CA). The GaAsP detector detected a fluorescence signal selected by a 495 – 540-nm band-pass emission filter. Cortical astrocytes (layers II – V of motor cortex) and astrocytes in ventral horns of the spinal cord were imaged in a z-stack with a uniform spacing of 0.5 µm and a resolution of 512 × 512 pixels with a voxel size 0.41 × 0.41 × 0.5 µm. The signal acquisition was set in a way that the cell body did not contain oversaturated pixels.

Measurements of fluorescence intensity (FI) and soma size (Ss) were performed in Fiji image processing software (ImageJ 2.9.0/1.53t) (https://fiji.sc) (Schindelin et al., 2012).

Variations of FI due to cell volume changes were monitored as follows: x-y-z image stacks acquired in each individual time point were reduced to 2D frames by an average intensity projection along the z-axis. These reduced images were composed to a time stack and aligned with StackReg (ImageJ plugin by Philippe Thévenaz, Biomedical Imaging Group, Swiss Federal Institute of Technology, Lausanne). Integral fluorescence intensities within a circular ROI of ~2 µm in diameter located within the cell soma were measured. Average intensity projections of the recorded 3D stacks were segmented by an automatic threshold based on the Isodata Algorithm (Ridler and Calvard, 1978). The cell area in the frame containing the segmented cell body was treated as the 2D measure of the Ss. Soma volume (Vs) is then proportional to √Ss3, assuming isotropic volume changes. For each CNS part (brain or spinal cord) at least 3 mice were used, with a minimum of 2 slices per mouse.

For all 3D-morphometry measurements, the imaging was done as follows: three full 3D stacks of images were acquired in the isotonic aCSF solution. During the cell volume changes induced by various solution treatments, individual 3D images were acquired in 5-minute intervals, 4 times in total. Finally, the cell volume recovery was checked after the re-application of isotonic aCSF solution (washout) after 20 and 40 minutes. Changes in the astrocyte volume are presented as the mean ± SEM. Statistical significance was determined using two-way ANOVA. Differences between the groups were considered statistically significant when $p < 0.05$ (*), very significant when $p < 0.01$ (**), and extremely significant when $p < 0.001$ (***).

3.3.4 Real-time Iontophoretic Method

Incubated slices were placed into the experimental chamber connected with upright Zeiss Axioscope microscope (Zeiss, Germany) and manipulators (Luigs and Neumann, Germany). Measurements were performed at room temperature (22–24°C) in a depth of 200 µm, and the chamber was continuously perfused with aCSF solution enriched with 0.1 mM tetramethylammonium ion (TMA^+) and saturated with carbogen. The stable control values were acquired in the aCSF, followed by a 20 minute application of increased potassium (K^+) concentrations (20mM or 50mM $aCSF_{K+}$) and by 40 minutes wash-out in aCSF. The diffusion curves were captured and analyzed every 5 minutes.

The ECS diffusion parameters, volume fraction α (α = ECS volume/total tissue volume), tortuosity λ (λ^2 = free diffusion coefficient/apparent diffusion coefficient) and nonspecific uptake (k' [s^{-1}]), were measured in acute brain and spinal cord slices using the real-time iontophoretic method (RTI) described in detail in Nicholson and Phillips (1981) and (Sykova and Nicholson, 2008). In brief, the extracellular marker TMA^+ (molecular weight 74.1 Da) was introduced into the tissue through the iontophoretic micropipette. The TMA^+ imitated the diffusion of small ions and molecules in the ECS and its time-dependent changes in the extracellular concentration were measured by double-barreled ion-selective microelectrodes (ISM). The manufacturing of double-barreled TMA^+- ISMs was described in detail previously (Syková, 1992). Briefly, the reference barrel was filled with 150 mM NaCl and the ion-sensitive barrel contained an ion exchanger IE190 (WPI, Inc., Sarasota, USA, RRID: SCR_008593) at the tip and 100 mM TMA^+ solution as a backfilling solution. Before each experiment, the TMA^+-ISMs were calibrated in a series of five different solutions with increasing TMA^+ concentrations: 0.1, 0.3, 1.0, 3.0 and 10.0 in a background of 3 mM KCl and 150 mM NaCl. The TMA^+ signals were fitted to the Nikolski equation to acquire the slope and interference of each ISM (Nicholson, 1993). The iontophoretic micropipettes backfilled with 100 mM TMA chloride were glued to individual ISMs with a tip separation 50-100 μm. Prior to the experimental measurements, the ISMs arrays were calibrated in 0.3% agar gel (Merck, Germany). The 20 nA bias current was continuously applied (Single Channel Iontophoresis Generator ION-100; Dagan Corporation, Minneapolis, Minnesota, USA) to maintain a constant electrode transport number. A current step of 200 nA and 24s duration (stimulator master 8, A.M.P.I, Jerusalem, Israel) generated a diffusion curve. The obtained diffusion curves were analyzed by a non-linear curve fitting simplex algorithm, operating on a modified diffusion equation using the VOLTORO program (kindly provided by C. Nicholson, New York University School of Medicine, USA, unpublished data) to acquire the values of the electrode transport number (n) and the free diffusion coefficient of TMA^+ (D). Knowing the n and D values, the parameters α, λ and k’ could be determined from the measured tissue.

Data are expressed as mean ± SEM, where n represents the number of slices/measurements. Statistical analyses were performed using Graph Pad statistical package (https://www.graphpad.com) - between experimental groups using two-way ANOVA analysis, followed by Sidak's multiple comparison test and one-way ANOVA with Dunnet's multiple comparison test to analyze changes within single group controls (CTRL) and SOD1 separately. Differences between the groups were considered statistically significant when $p < 0.05$ (*), very significant when $p < 0.01$ (**), and extremely significant when $p < 0.001$ (***). The method has been done in cooperation with the Second Faculty of Medicine, Charles University.

3.4 Materials and Methods Specific for Aim 1

3.4.1 The Preparation of Single-cell Suspension

Animals were deeply anaesthetized with PTB (100 mg/kg, i.p.), and perfused transcardially with a cold (4–8 °C) isolation buffer containing (in mM): NaCl 136.0, KCl 5.4, HEPES 10.0, glucose 5.5, osmolality 290 ± 3 mOsmol/kg. The motor and primary somatosensory cortex were isolated and processed according to the Adult Brain dissociation protocol for mice and rats (Milteyni-Biotec, Germany) without the red blood cell removal step. To prevent the activation of immediate early genes (IEGs), we used transcriptional inhibitor actinomycin D (Sigma–Aldrich, St. Louis, MO), 30 μM during enzymatic dissociation and 3 μM in the following steps (Wu et al., 2017). Following the debris removal, the cells were layered on top of 5 ml of ovomucoid inhibitor solution (Worthington, NJ) and harvested by centrifugation (300 × g for 6 min). Potential cell aggregates were removed by 70 μm cell strainers (Becton Dickinson, NJ). The final suspension was labeled with ACSA-2, Cd11b and O4 antibodies conjugated with allophycocyanin and phycoerythrin respectively (4 °C, 10 min; Miltenyi-Biotec, Germany) to allow for the enrichment of targeted cell types: astrocytes, microglia and oligodendrocytes. The cells were enriched using fluorescence activated cell sorting (FACS; BD Influx, San Jose, CA, United States), calibrated to sort ACSA-2+, Cd11b+ and O4+ cells. We used Hoechst 33258 (ThermoFisher Scientific, Waltham, MA) to check viability. Sorted cells were collected into 200 μl of Advanced Dulbecco's Modified Eagle Medium, supplemented with 10% fetal bovine serum (ThermoFisher Scientific Waltham, MA). Four animals per condition were pooled for the preparation of cell suspension. After FACS, the cell suspension was spun down, concentrated, and used for library preparation.

3.4.2 scRNA-seq

Chromium Next GEM Single Cell 3' Reagent Kit v3.1 (10 × Genomics, Pleasanton, CA) was used to prepare the sequencing libraries, and the protocol was performed according to the manufacturer’s instructions. Briefly, we used 10 × Chromium platform to encapsulate individual cells into droplets along with beads covered in cell-specific 10 × Barcodes, unique molecular identifiers (UMIs) and poly(dT) sequences. After reverse transcription, the cDNA libraries were amplified (13–14 cycles), fragmented and ligated to sequencing adaptors. SPRISelect magnetic beads were used for purification of the cDNA suspension and size selection of the fragments. Concentration and quality of the libraries was measured using Qubit dsDNA HS Assay Kit (Invitrogen) and Fragment Analyzer HS NGS Fragment Kit (#DNF-474, Agilent). The libraries were pooled and sequenced in paired-end mode using Illumina NovaSeq 6000 SP Reagent Kit, Read 1 containing a barcode and a UMI, and Read

2 covering the sequence of interest. Sequencing data comprised of approx. 100–200 million reads per sample.

3.4.3 Data Analysis

The sequencing data were aligned to the reference mouse genome GRCm38 and annotated (GENCODE version M8 annotation) by STARsolo (STAR version 2.7.3a) (Dobin et al., 2013). EmptyDrops function (DropletUtils R package) (Lun et al., 2019) with a threshold of 100 UMIs and FDR < = 0.001 was applied to preserve only cell-containing droplets. Cells were counted based on the barcodes specific for each droplet/cell. The final number of detected cells differed among samples and was in the range from approx 2500 to 6800 cells.

The data were then processed using Seurat R package (version 4.1.1) (Hao et al., 2021). First, data from all samples were SCTransformed and integrated (excluding mitochondrial and ribosomal genes, prefixed by mt- or Rps/Rpl, respectively). Uniform Manifold Approximation and Projection (UMAP) was used to visualize 17 principal components (PC), which were then clustered (FindNeighbors and FindClusters functions, UMAP resolution 0.5). Clusters were annotated based on the expression of known marker genes of the expected cell populations, and their correspondence to the markers found by the FindAllMarkers function (at least 80 % cells in the cluster expressing the markers). DoubletFinder (McGinnis et al., 2019) R package was used to identify droplets potentially containing more than one cell. Doublet formation rate was set to 3.9 % as estimated by 10 × Genomics and we processed the data according to the authors' recommendations. Clusters expressing ambiguous markers and containing a higher number of doublets were filtered out of the data set.

Each cell was assigned sex (male, female) based on the expression of genes encoded by X (*Xist*) and Y chromosome, and cells not matching our criteria (male: counts of *Xist* < 1, nFeature_Y > 0; female: counts of *Xist* > 0, nFeature_Y < 2, nCount_Y < 2; nFeature_Y being a number of Y-encoded genes and nCount_Y being a number of transcripts mapping to Y chromosome) were excluded from the dataset. The cells classified as 'Undefined' comprised almost 1/3 of the total number of cells and represented low quality cells.

A specific gene expression profile was used to determine cell cycle phase of each cell (CellCycleScoring Seurat function) to ensure that the cells in all phases are equally distributed among clusters. Individual cell types were filtered based on the number of detected genes (nFeature_RNA), number of counts (nCount_RNA) and amount of mitochondrial RNA (percent.mt). The cut-offs specific for each cell type of interest were the following: astrocytes—nFeature_RNA > 1000, 2000 < nCount_RNA < 10,000, percent.mt < 8; microglia—nFeature_RNA > 700, 1000 < nCount_RNA < 10,000, percent.mt < 5; oligodendrocytes—nFeature_RNA > 1300, 2500 < nCount_RNA < 50,000, percent.mt < 5. Tissue dissociation can induce the expression of IEGs, the first rapid cellular response to stimuli (Wu et al., 2017, Marsh et al., 2022). A set of the IEGs (e. g. *Fos* and *Jun* transcription factors) was projected onto the UMAP using AddModuleScore function to investigate the induction level of these genes by sample preparation. The SoupX R package (version 1.5.2) (Young and Behjati, 2020) was applied to remove the contaminating RNA background. The unfiltered and annotated data were supplied as the input. The contamination fraction was estimated by the automated method and was in the range from 1-2 % for individual samples. The count values were subsequently corrected for the contamination.

To view the overall differences between samples by pseudobulk principal component analysis (PCA), a normalized and scaled data set was used to create a pseudobulk data by summing up the gene counts of cells belonging to the same condition, age, and sex.

3.4.4 Differential Expression Analysis and Gene Set Enrichment Analysis

Differentially expressed genes (DEGs) in the single-cell data set were identified by t-test in Seurat's FindMarkers function. Normalized and scaled data in the RNA assay were used in this analysis. The P-adjusted value (padj) threshold was set to 0.05, and genes with log2 fold change (log2FC) > 1 or < − 1 were considered differentially expressed. We compared males and females at each time point for each cell type and condition. CTRL and SOD1 pairs were tested at each time point and for each cell type. The Gene Set Enrichment Analysis (GSEA) (Subramanian et al., 2005) was performed using clusterProfiler R package (version 4.0.5)33,34. The reference gene set size was limited to 10–800 genes and the significance threshold was set to padj = 0.05. Only results in which more than one gene contributed to the enrichment (core enrichment) were considered relevant.

3.4.5 The Analysis of Cellular Subtypes

Individual cell types of interest (astrocytes, microglia, oligodendrocytes) were analyzed separately. Mitochondrial and ribosomal genes were not included in the subsequent analyses. The filtered, normalized, scaled and SCTransformed data were then subjected to PCA. Within the scope of quality control, several genes were excluded, as they introduced additional undesirable variability in the clustering (*Sod1*, *Gm8566*, *Cmss1*, *Cdk8* and lncRNAs *Xist*, *Gm42418*, *Gm424181*, *Malat1*). 16 PC for microglia and astrocytes, and 17 PC for oligodendrocytes were visualized using UMAP, and clustered at a resolution of 0.2 (FindNeighbors and FindClusters functions). A cluster of male control cells at the 3 M time point was excluded from the astrocyte and oligodendrocyte subsets, as it expressed potentially stress related marker genes (e.g., *Cdkn1a*, *Fkbp5*), which might have been induced during sample preparation.

Markers of the sub-clusters were identified using the default Wilcoxon test in the FindAllMarkers function (at least 10 % cells in a cluster expressing the given marker, log2FC > 0.25). The identity of the sub-clusters was determined by comparison with available gene signatures of various previously described cellular subtypes using the AddModuleScore function and by manual annotation based on the calculated marker genes. Reference gene expression signatures were taken from Habib et al. (2020) (Gfap-Low and Gfap-High astrocytes), Sala Frigerio et al. (2019) (ARM, IRM) and Marques et al. (2016) (MFOL1/2, MOL2, MOL5/6). The intermediate state of astrocytes was visualized using a gene set containing calculated markers of cluster 2 and markers of transition state published by Habib et al. (2020). The signature of homeostatic microglia resulted from the combination of homeostatic markers mentioned in Keren-Shaul et al. (2017), Mathys et al. (2017) and (Butovsky and Weiner, 2018). The top 30 genes were used for the projection in astrocytes, and 20 genes were used in the microglia and oligodendrocytes.

3.5 Materials and Methods Specific for Aim 2

3.5.1 Cerebrospinal Fluid Isolation

The experiment was performed using SOD1/GFAP/EGFP and CTRL/GFAP/EGFP mice at the age of four months. To isolate the cerebrospinal fluid (CSF), we used modified protocol from (Kaur et al., 2023). We used borosilicate glass capillaries (Sutter Instruments, Novato, CA, United States) and P-97 Brown-Flaming puller (Sutter Instruments, Novato, CA, United States) and prepared the capillary, using pulling settings as specified in the protocol. The mice were first anesthetized with 3% isoflurane (Abbot, IL, United States) and maintained at 1-2% isoflurane using a vaporizer (Tec-3, Cyprane Ltd., Keighley, United Kingdom). We did not use a stereotactic instrument but followed the protocol with cisterna magna exposure and then the CSF extraction. We looked for any traces of blood contamination and used only clear samples for further analysis (Fig. 24). The body temperature of the mouse was maintained at 37 ± 1°C using a heating pad throughout the procedure and the mouse was sacrificed immediately after finishing the experiment.

3.5.2 Elemental Analysis

The ion concentration in the cerebrospinal fluid was determined using inductively coupled plasma optical emission spectroscopy (ICP-OES) coupled with an electrothermal evaporation (ETV) unit. The analysis was done in cooperation with the analytical laboratory at IOCB Prague. ICP-OES is a widely used highly sensitive analytical method capable of determining most elements. In brief, a sample in the form of a solution is converted to a fine aerosol, which is then carried by a stream of argon into a high-temperature argon plasma, where evaporation, atomization, and excitation take place. The characteristic radiation emitted by the excited atoms is then processed in the spectrometer. The ETV is an alternative sample introduction system, which allows direct analysis of solid or liquid samples. The sample was weighed in a graphite boat and heated in a graphite furnace using an optimized temperature program in an argon atmosphere, with the maximum achievable temperature of 3000 °C. The addition of a small amount of CCl_2F_2 into the furnace facilitates the conversion of analytes to more volatile forms, thus ensuring complete analyte evaporation. The generated dry aerosol is carried by argon stream directly into the plasma. This approach offers lower detection limits and matrix-independent calibration, thus allowing the analysis of smaller sample amounts, thanks to nearly loss-free transport of the sample directly into the plasma. For analysis, 10 µl of cerebrospinal fluid was pipetted into a graphite boat and the sample amount was checked by weighing it. Due to low sample volumes, only one replica per sample was possible. An Arcos I (Spectro, Kleve, Germany) ICP-OES instrument coupled to an ETV 4000c unit (Spectral Systems, Fürstenfeldbruck, Germany) was used for the analysis.

4 RESULTS

4.1 Characterization of the SOD1(G93A) Mouse Model Phenotype and Pathological Traits in the Motor Cortex

4.1.1 Animal Model Evaluation

First, we aimed to characterize the major turning points of the disease such as the onset, symptomatic phase, and final stage in the used animal model. Based on those data, we set the main time points for future experiments.

To do so, we used two types of behavioral testing—the wire grid hang test and the Rotarod performance test. We tested comparable groups of animals with SOD1(G93A) mutation (SOD1), and non-carrier littermates (CTRL) with even numbers of males and females in each group. The beginning of the testing period was at one month of age and all the animals reached the maximum time (180 s) in both tests. The first noticeable difference between SOD1 and CTRL animals was in the wire grid hang test (Fig.10a), which primarily assesses muscle strength. The difference occurred at two months of age and this point was further on considered an onset of the disease. The performance then slowly declined until a sudden drop at three months of age, which we consider a point of the symptomatic stage. At four months of age, the animals reached the end-stage marked by a serious impairment of motor functions. The motor coordination was measured by the Rotarod (Fig.10c) and was significantly impaired only at the end-stage.

As one of the risk factors of ALS in patients is sex, we were interested to see whether this translates to the animal model. We compared the SOD1 male versus female performance and indeed, the wire grid hang test revealed differences in the symptom onset and the progression in general (Fig. 10b,d). The onset was earlier in males, and they overall performed worse than the females, which agrees with human pathology (McCombe and Henderson, 2010). Despite the later onset, the female´s performance in the symptomatic stage declined faster than the male´s and the results at the end-stage were comparable. The Rotarod measurements did not reveal any significant sex-related differences throughout the progression.

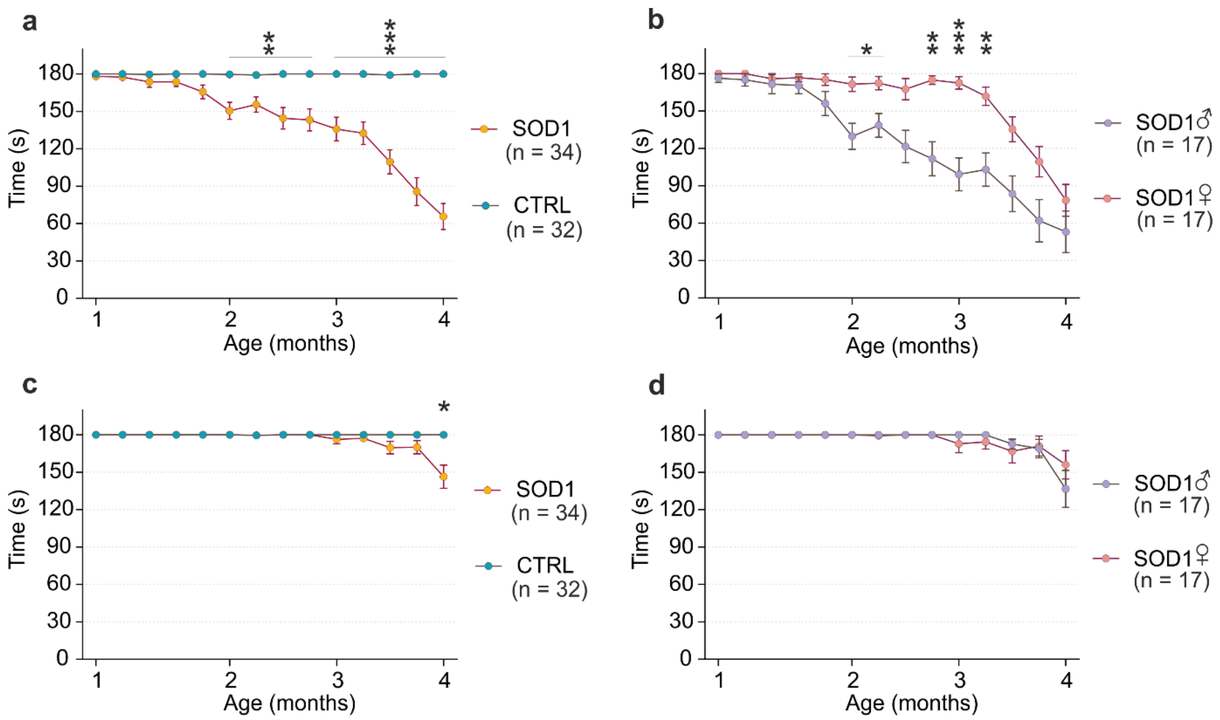

Fig. 10 The cortical pathology evaluation by behavioral testing. A) The hanging wire test confirmed the motor skills decline in SOD1 animals during progression compared to the CTRLs. B) Results from the hanging wire test comparing SOD1 animals divided based on sex revealed phenotypical differences in onset. C, D) The Rotarod results comparing the CTRL and SOD1 animals did not reveal significant changes during the progression until the final stage and did not reveal differences between performance when comparing males and females. Data are presented as mean ± SEM. n = the number of mice.

4.1.2 Identification of Targeted Glial Cell Populations in the Cortex of SOD1 and CTRL Mice

To explore the cellular pathology in the cortex, we employed scRNA-Seq. The experiment was executed as follows: SOD1 and CTRL animals were sacrificed at four time points, representing different stages of the disease progression, with two males and two females used per each condition and at each time point. The cell suspensions were prepared from the motor and somatosensory cortex and enriched for astrocytes, microglia and oligodendrocytes using FACS (Fig. 11a).

The transcriptomic data followed an initial quality control, filtering and clustering. The resulting set of single cells was then annotated using canonical marker gene expression of individual glial cell types (Fig.11b,d). As expected after the enrichment, the most numerous clusters were astrocytes (*Aqp4*, *Aldh1l1*, *Gjb6*), microglia (*Cx3cr1*, *Aif1*), and oligodendrocytes (*Mobp*, *Apod*). Oligodendrocyte precursor cells (OPC) and committed oligodendrocyte precursor cells (COP) clustered separately from mature oligodendrocytes and their marker genes partially overlapped, which indicates a gradual maturation of OPCs into oligodendrocytes (*Emid1*, *Pdgfra*, *Sox6*, *Vcan*, *Plp1*, *Cldn11* and others). We also identified perivascular macrophages, pericytes, and endothelial cells, which were present in the minority.

To observe possible differences related to sex on a cellular level, each cell was assigned a sex identity based on its expression of X and Y chromosome-associated genes. Cells that did not meet the criteria for sex determination were excluded. No cluster was overrepresented in either condition or the male/female samples, thus confirming the cell preparation´s robustness (Fig. 11c). Other evidence for the data quality also included the low proportion of mitochondrial reads and minimal activation of immediate early genes.

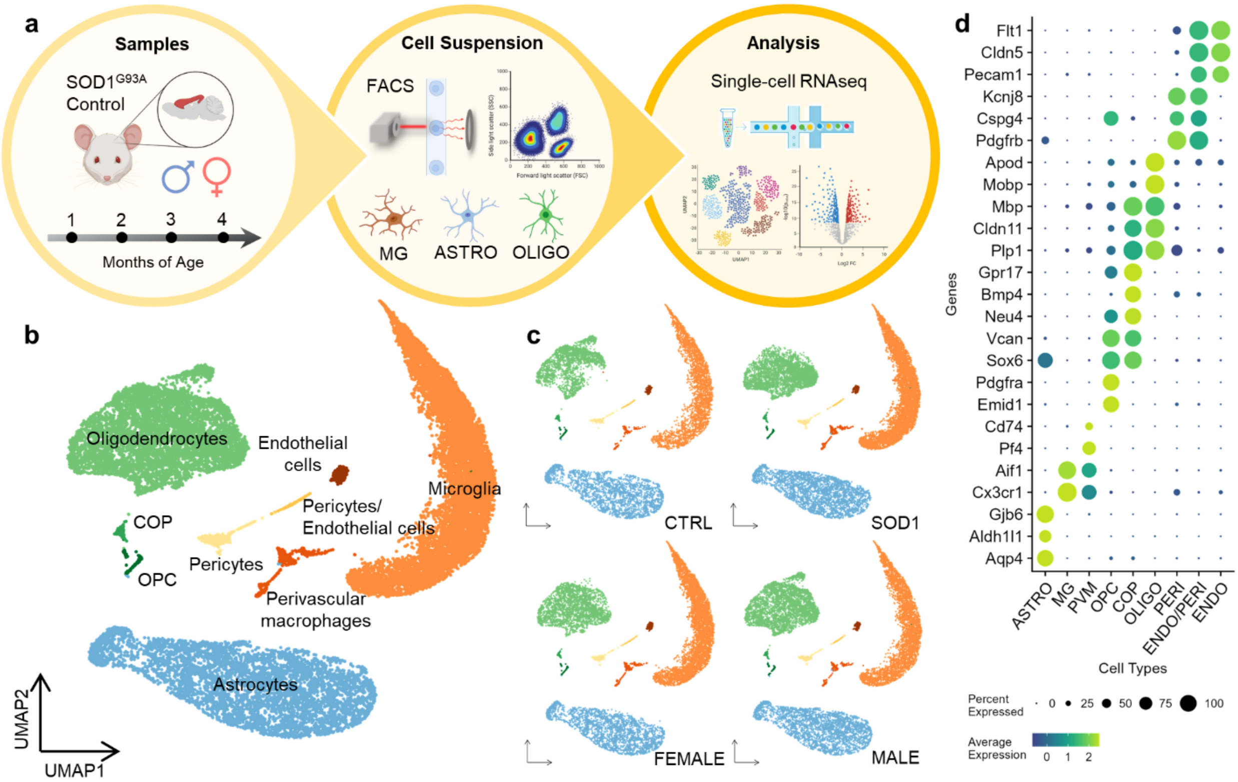

Fig. 11 Single-cell RNA sequencing experiment overview. A) A scheme summarizing the process of the sequencing experiment. (created with biorender.com) B) A UMAP plot visualization of the identified cell clusters, containing cells from all samples. ASTRO n = 5536, MG n = 8429, OLIGO n = 6180, PVM n = 434, OPC n = 165, COP n = 98, PERI n = 395, ENDO n = 235, ENDO/PERI n = 108, total n = 21580. C) A visualization of cluster representation and the prevalence of targeted glia in both conditions and sexes. CTRL n = 7646, SOD1 n = 12499, female n = 10246, male n = 9899. D) A list of canonical marker genes used for identification of cell clusters. ASTRO – astrocytes, MG – microglia, PVM – perivascular macrophages, OPC – oligodendrocyte precursor cells, COP – committed oligodendrocyte precursors, oligo – oligodendrocytes, PERI – pericytes, ENDO – endothelial cells.

4.1.3 Differences of Gene Expression in Cortical Glia at the Final Stage of Pathology

To get a general overview of the gene expression in SOD1 mice, astrocytes, microglia, and oligodendrocytes were subjected to PCA analysis as a pseudobulk (Fig.12). The results revealed only minor changes between the CTRL and SOD1 samples in both sexes during disease progression. The first noticeable shift appeared in microglia and oligodendrocytes in the samples from the final stage of the disease and suggests their reaction to ALS-like pathology. The SOD1 astrocytes remained surprisingly unchanged and clustered with the CTRL samples.

The clustering showed a notable displacement of the three-month-old (3M) male data points, which was the most prominent in astrocytes, where it represented the highest variability source (reflected by separation in PCA1). When we explored this further, we identified a small cluster of cells within astrocytes and oligodendrocytes that was only present in 3M CTRL males. This was characterized by the expression of stress-related genes *Cdkn1a* and *Fkbp5*, which had the most extreme values of loadings in respective PCs in the pseudobulk analysis. This confirmed the effect of this cluster on the displacement of 3M CTRL male data points. Most likely the presence of this cluster is a technical artifact of sample processing and since it has a negligible effect on further analyses, we removed it from the dataset. This finding, though, showed the power of the single-cell analysis to identify even minor changes in cell subpopulations, which might be hard to interpret in the classic bulk analysis.

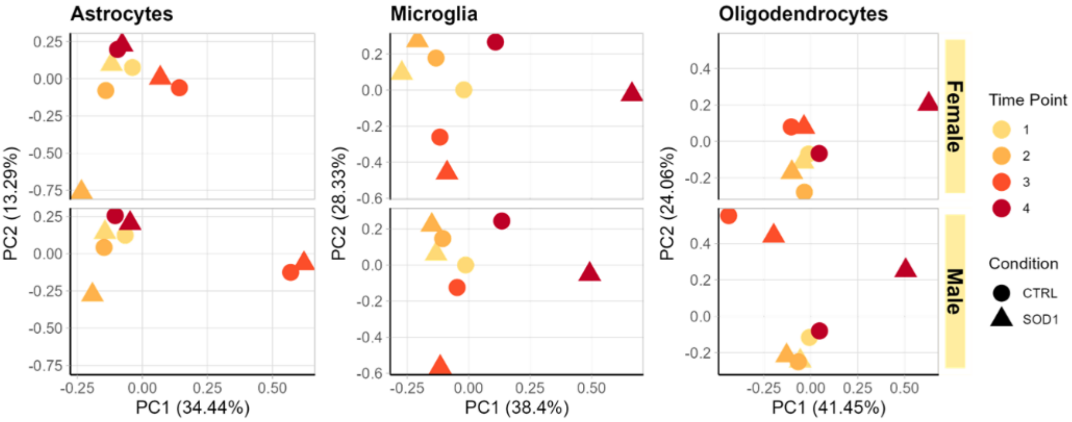

Fig. 12 Pseudobulk PCA clustering comparison of male and female samples showing a shared reaction to the ongoing pathology in microglia and oligodendrocytes at 4M.

Based on the sex-related differences observed in the behavioral test (Fig. 1), we investigated the potential ALS-related gene expression alterations between the sexes by DEA and compared the male and female cells for CTRL and SOD1 separately. Only a few DEGs with a threshold of $|\log_2\text{FC}| > 1$ and $p_{\text{adj}} < 0.05$ were identified. The X chromosome gene *Xist* was significantly upregulated in all three cell types in the females, regardless of genotype. The *Xist* plays a crucial role in the gene dosage compensation in females by silencing one of the X chromosomes, thus is expressed only in female cells (Loda and Heard, 2019). Two genes encoded by chromosome Y (*Eif2s3y*, *Uty*) were upregulated in males, but the different expression only exceeded the threshold in astrocytes (Fig.13). No other dysregulated genes related to sex were found in our data.

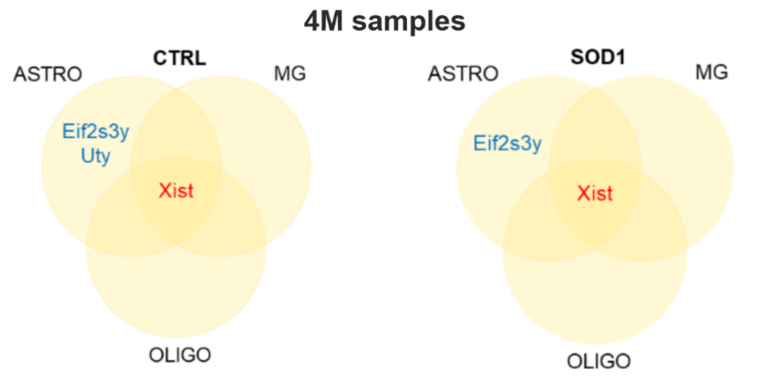

Fig. 13 A visualization of the few differentially expressed genes found dysregulated in males and females in all cell types at the 4M time point. *Xist* clearly distinguishes female cells, whereas *Eif2s3y* and *Uty* are expressed by male chromosome Y.

To investigate ALS-related transcriptional changes, DEA was performed on the comparisons of CTRL and SOD1 samples at each time point and for each cell type, with pooled male and female cells together. The *Sod1* gene was the only significantly upregulated DEG in all measured stages of the disease including the end-stage (Fig.14), which confirms the validity of the animal model. Other dysregulated genes were mostly noncoding or ribosomal transcript that evaded quality control. The end-stage (4M) CTRL samples were also marked by an increased expression of genes *Cdk8* and *Cmss1* across all the cell types. Those two genes were identified in the following analysis as confounders negatively sub-clustering results. Therefore, we concluded they are a biasing factor without connection to the ALS-like pathology. Altogether, our result showed minimal gene expression variation related to ALS progression in the cortex of SOD1 animals regardless of sex, but with indication of some changes in microglia and oligodendrocytes at the end-stage of the disease.

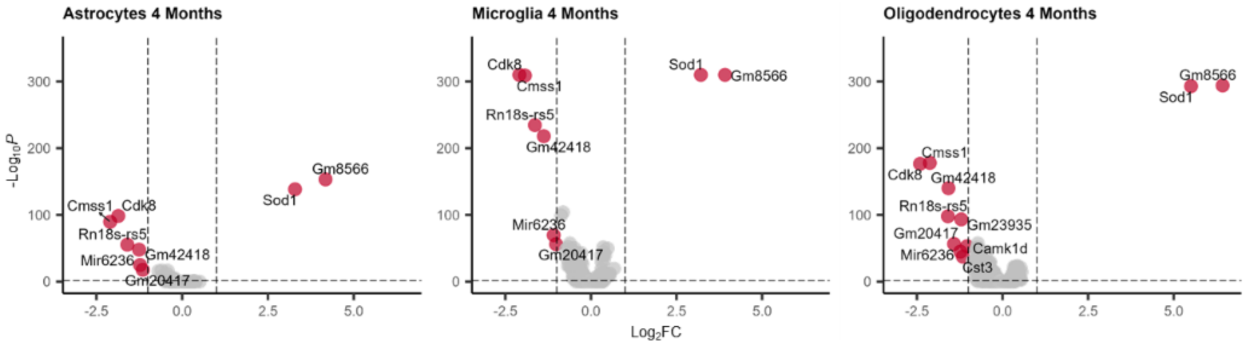

Fig. 14 Results of the DEA comparing CTRL and SOD1 4M samples show a limited number of upregulated and downregulated genes at the final stage.

4.1.4 Gene Set Enrichment Analysis of Altered Mitochondria Functions in Microglia and Oligodendrocytes

We were interested in the biological significance of the changes identified by DEA, so we employed the GSEA (Subramanian et al., 2005) and focused on the most affected time point – the final stage (4M). GSEA considers the information about the expression of all genes, regardless of thresholds in the log2FC or p-value and it is thus able to identify any dysregulated processes, even though the changes of individual involved genes are minimal.

First, we did a meta-analysis and collected the gene signature of glial cells affected by SOD1 mutation from 15 transcriptomic studies published in the last two decades. The GSEA revealed enrichment of a single gene set, reported by Liu et al. (2020) as downregulated in the brainstem oligodendrocytes in 100-day-old SOD1(G93A) mice. Consistent with that, our results showed a negative enrichment in oligodendrocytes ((NES = − 1.32, padj = 6.3 × 10− 3; NES—normalized enrichment score; Fig. 15), indicating small, although significant changes in the cortical oligodendrocytes at the final stage of the disease. We did not identify any gene sets enriched for microglia or astrocytes.

Beside the meta-analysis, we also looked for Gene Ontology (GO) terms (Ashburner et al., 2000) enriched in our data set. Two terms related to mitochondria were upregulated in our data: *mitochondrial envelope* in oligodendrocytes (NES = 1.11, padj = 8.2 × 10–3) and *mitochondrial protein-containing complex* in microglia (NES = 1.73, padj = 1.1 × 10–6) (Fig. 15). In support of our conclusions, mitochondrial dysfunction has been discussed as one of the contributing factors in ALS, not only concerning the *Sod1* gene, but also others (Jankovic et al., 2021).

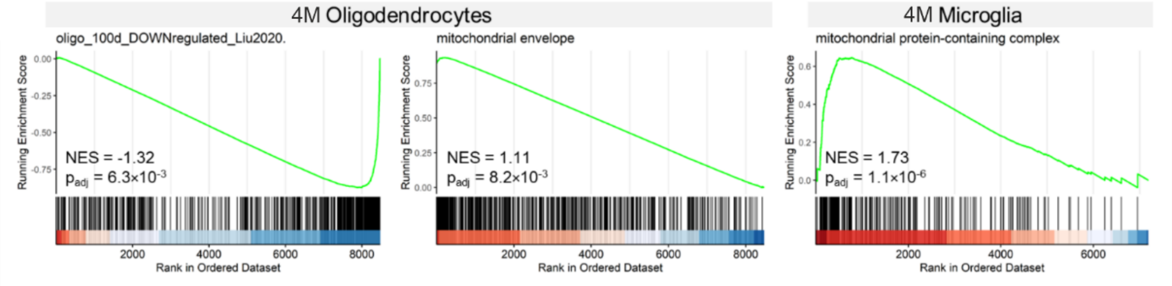

Fig. 15 Enrichment curves visualizing the results of the GSEA at 4M. One reference gene set was enriched among genes downregulated in oligodendrocytes. Analysis of GO terms showed mitochondrial components to be enriched among genes upregulated in oligodendrocytes and microglia.

4.1.5 Subpopulation Analysis of Targeted Glia

As the changes in gene expression were minor, we speculated that they might be represented by a small fraction of cells, hidden at the population level within each cell type. To explore this possibility, we used an in-depth sub-clustering analysis to identify subpopulations potentially playing a role in the disease.

The analysis of astrocytes revealed three clusters present in both CTRL and SOD1 samples in a similar proportion (Fig. 16a). We annotated them based on their marker genes and visualized the gene signature of astrocytic subtypes described by Habib et al. (2020) in the model of AD. They identified two similar subpopulations of astrocytes expressing markers of reactivity – Gfap-High and DAAs. The Gfap-High population was detected in both control and AD samples. DAAs on the other hand, were unique to the AD model and the authors suggested their involvement in the disease. Marker genes of cluster 3 in our data partially overlapped with the Gfap-High cluster (*Mt1, Mt2, Id3, Cd9, Vim*), but we did not find DAAs in SOD1 samples. Cluster 1 shared a profile with Gfap-Low astrocytes (*Luzp2, Trpm3*) and markers of both Gfap-High and Gfap-Low were expressed in Cluster 2, which most likely represents an intermediate state.

As for microglia, they were grouped into four clusters (UMAP plot in Fig.16b). Cluster 1 was marked by the expression of homeostatic genes (Butovsky and Weiner, 2018, Keren-Shaul et al., 2017, Mathys et al., 2017). The signature of clusters 2 and 3 resembled the expression profile of ARMs. ARMs typically downregulate homeostatic genes like *Cx3cr1, P2ry12,* and *Sall1*, which we observed in our data as well (Fig. 16b). Cluster 3 was additionally marked by a higher expression of *Apoe* – a major regulator of microglial neurodegenerative phenotype (Krasemann et al., 2017). Cluster 4 was clearly marked by the expression of *Ifit2, Ifit3* and *Ifit3m*, the genes involved in the interferon response pathway and thus represented IRMs (Sala Frigerio et al., 2019). The IRM proportion though, was very low in both conditions. Overall, we detected a small increase in the activated microglia subpopulation in SOD1 samples (cluster 2), which suggests a starting activation in response to the ongoing pathology.

Oligodendrocytes formed four clusters (Fig. 16c). Cluster 1 gene expression corresponded to the profile of forming oligodendrocytes (MFOL) described by Marques et al. (2016). These cells were present predominantly in the one-month-old (1M) sample (Fig.16d), which coincided with the extensive myelination in rodents in the early weeks after birth (Doretto et al., 2011). Cluster 2 represented mature oligodendrocytes (MOL2) expressing *Klk6*, but also mature oligodendrocyte marker *Apod* and genes typical for myelinating cells *Pmp22, S100b,* and *Apc*. The proportions of clusters 1 and 2 were similar in both conditions. Clusters 3 and 4 had increased expression of several genes detected in mature oligodendrocyte populations MOL5/6 (Floriddia et al., 2020, Marques et al., 2016). Strikingly, cluster 4 was almost exclusively present in the SOD1 samples (Fig.16c) and was characterized by a higher expression of *Il33* and *Apoe*. The *Il33* has been reported in disease-associated oligodendrocytes in an AD model (Kenigsbuch et al., 2022, Lee et al., 2021). *Apoe* was associated with immune oligodendroglia, multiple sclerosis, and chronic demyelination (Jakel et al., 2019). We thus hypothesize that cluster 4 could be damaged or reactive oligodendrocytes, reacting to the pathological processes in the SOD1 cortex. Overall, we were able to identify multiple subpopulations within each studied cell type and recognized gene expression signatures of specific, previously characterized cellular subtypes. However, in contrast with our expectations, we did not find any subpopulations specific to the SOD1 samples, apart from the damaged/activated oligodendrocytes.

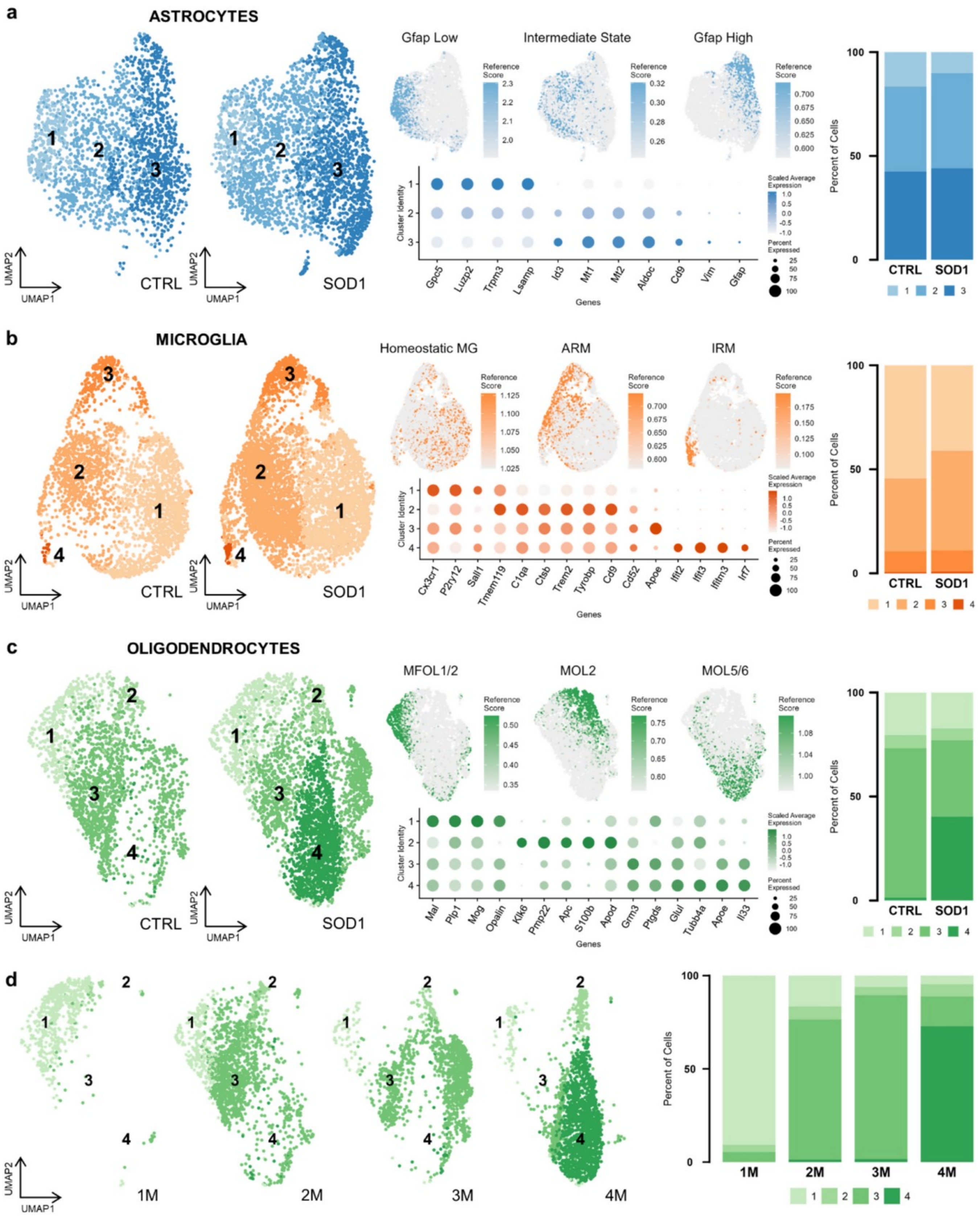

Fig. 16 The subpopulation analysis revealed a unique subpopulation of oligodendrocytes in SOD1 samples. UMAP visualization of subpopulations of astrocytes (n = 5292) A), microglia (n = 8414) B), and oligodendrocytes (n = 5876) C) split to CTRL and SOD1 condition (left), including cells from all four time points. The gene expression signatures of previously described subpopulations are

shown projected onto UMAP (middle-top). A list of representative cluster markers used for their annotation (middle-bottom). Proportions of subpopulations in CTRL and SOD1 (right), including cells from all four time points. D) UMAP visualization of CTRL and SOD1 oligodendrocytes split according to age (1 m: n = 682, 2 m: n = 1697, 3 m: n = 1430, 4 m: n = 2067). Bar plot shows proportions of subpopulations at each time point.

4.1.6 Immunohistochemical Validation of Transcriptomic Data

To validate the conclusions from scRNA-seq of minor glia changes in the cortex, we used immunohistochemical analysis of glia in the motor and primary somatosensory cortex (the identical region used for the sequencing) (Fig.17a). We only investigated animals in the final stage, when the changes were the most pronounced. Since the glial pathology has been confirmed in the spinal cord before, we also stained the lumbar region of the spinal cord at the final stage and used it as a reference for advanced gliosis in the model.

Astrogliosis is typically accompanied by enlargement of the cellular body and shortened, thickened processes. For their visualization, we used ALDH1L1 marker, allowing for the inspection of the whole cell morphology (cell body and processes). We conducted a fluorescence analysis to identify any of those changes, however, similar fluorescence values were observed in both CTRL and SOD1 slices, suggesting no morphological changes associated with astrocytic activation (Fig.17b,c). On the other hand, astrocytes in the lumbar region show an enlarged body with distinctively shortened processes. Results from our fluorescence analysis align with the results from the gene expression level suggesting that there is either very little or no change in cortical astrocytes.

Microglia, similarly to astrocytes, change their morphology in response to pathology. They retract the processes and acquire a typical amoebic shape. We used IBA1 antibody to visualize microglia and again stained both the cortex and lumbar part of the spinal cord. To evaluate the shortening of the processes we employed the Sholl method, which is frequently used to quantify the complexity of cell arborization. Results from this analysis confirmed that the morphology of CTRL and SOD1 microglia did not differ, and we did not detect any signs of shorter processes or reduced branching (Fig. 17d). However, during this analysis, we noticed that some tips of the processes looked bulbous and enlarged (Fig.17e). These are called *bulbous termini* and appear as the first reaction of microglia after injury (Davalos et al., 2005). In our samples, they could represent an initial phase of microglial activation, which would agree with the results we obtained from the transcriptomic data. The microglia in the ventral horns of the lumbar spinal cord adopted the amoebic shape with quite short processes, which is a typical morphological shape of their activation.

The transcriptomic data and subpopulation analysis identified a SOD1-specific oligodendrocyte cluster (cluster 4). As we hypothesized that this cluster could represent damaged cells, we focused on the protein expression changes related to chronic demyelination, necrosis or apoptosis. Therefore, we stained the slices for myelin basic protein (MBP)—a marker of myelination, adenomatous polyposis coli (APC)—a marker of adult oligodendrocytes, and cleaved caspase 3 (CC3)—an apoptotic marker. The quantification of the MBP intensity signal in the cortex as well as the number of APC+ cortical oligodendrocytes excluded the hypothesis of demyelination processes, as there was no decrease of MBP or APC+ cells in the SOD1 compared to CTRLs (Fig.17f). Similarly, the co-staining of CC3+ oligodendrocytes suggests a similar rate of apoptosis for both CTRL and SOD1 (Fig.17f). MBP staining and representative images of a cell positive for APC and CC3 can be found in Fig.17g. Altogether, our data did not suggest significant demyelination or degeneration and it is thus likely, that the cluster 4 does not represent dying or damaged cells.

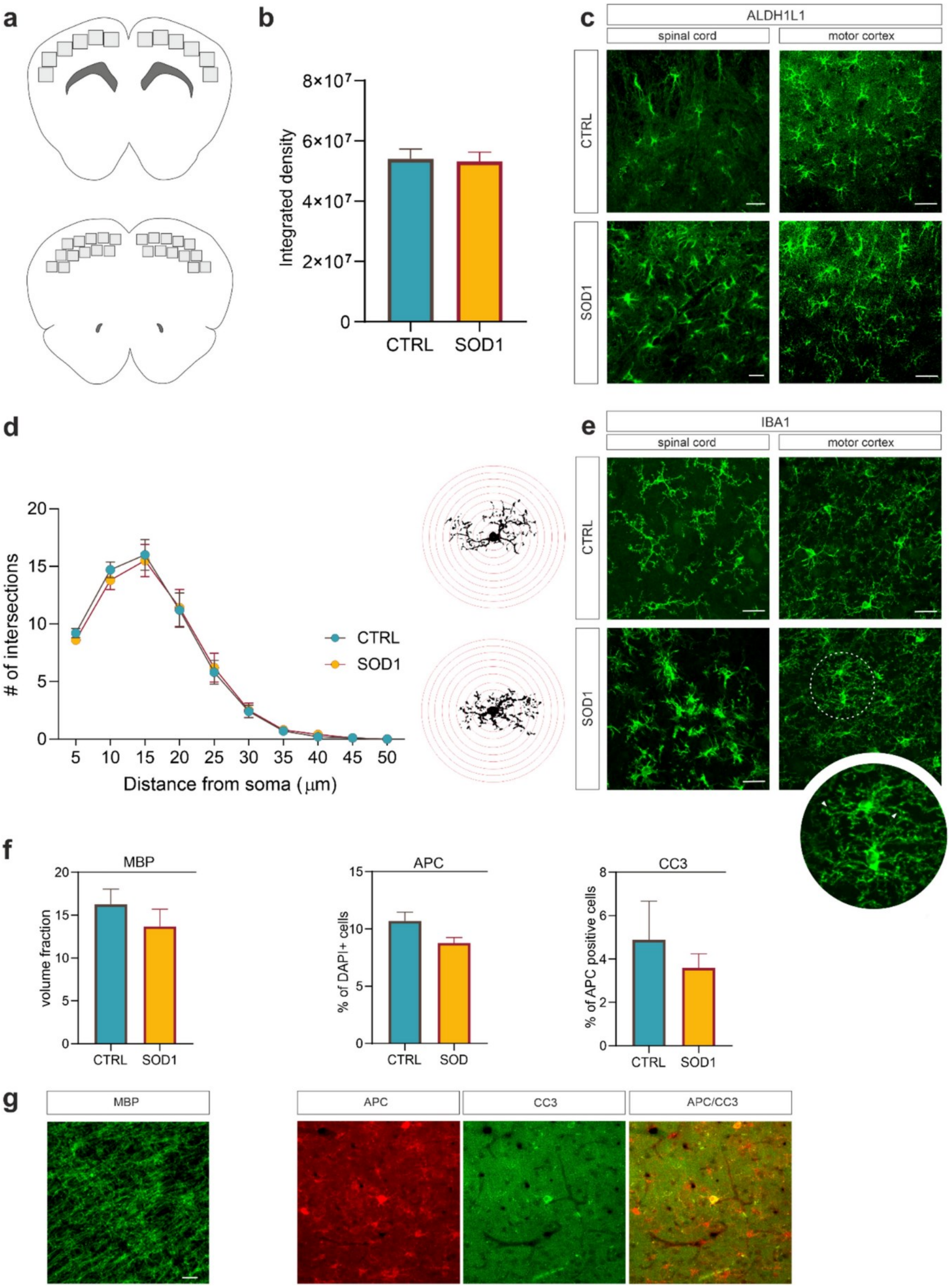

Fig. 17 The immunohistochemistry A) The upper illustration depicts 12 areas scanned for the investigation of morphological changes and quantification of APC and CC3. The lower illustration shows 24 areas scanned for the MBP analysis. B) The bar plot represents results from the fluorescence analysis, which did not reveal any differences in morphology between cortical astrocytes in SOD1 (n = 6) and CTRL (n = 6) animals. C) Representative pictures of ALDH1L1

staining in the cortex and the spinal cord comparing astrocytes, showing the morphological difference between SOD1 and CTRL in the spinal cord but no noticeable difference in the cortex. D) The results of Sholl analysis indicated very similar microglia complexity in both CTRL (n = 6) and SOD1 (n = 6) samples. Scholl masks with red concentric radii depict single-thresholded microglia as they were used for the analysis. E) representative images of cortical and spinal slices stained with IBA1 show evident amoebic morphology of spinal microglia but only subtle morphological changes represented by *bulbous termini* (see close up) in the cortex. F) The quantification of MBP in the cortex revealed no difference between SOD1 (n = 6) and CTRLs (n = 6). The number of APC+ cells was consistent between SOD1 (n = 3) and CTRLs (n = 3) and the number of APC+ cells co-stained with CC3 used as a marker of apoptosis in oligodendrocytes also remained similar, suggesting no apparent oligodendrocyte degenerations. G) Representative images of MBP, APC, and CC3 staining scale bars, 20 µm. The statistical significance was determined using an unpaired t-test. Error bars represent SEM. n states the number of used animals.

4.2 Functional Properties of Astrocytes in the Mouse Model of ALS

4.2.1 Animal Model Evaluation

To assess the functional properties of astrocytes, we took advantage of our crossbred mice with ALS-like pathology and fluorescently labeled astrocytes due to the expression of enhanced green fluorescent protein (EGFP) under the control of the human glial fibrillary acidic protein (GFAP) promoter (Nolte et al., 2001). To confirm the phenotype of the created crossbreed SOD1/GFAP/EGFP, we used the same behavioral tests as previously – the wire grid hang test and Rotarod.

First, we compared the SOD1/GFAP/EGFP (n = 34) and CTRL/GFAP/EGFP (n = 36) mice (Fig. 18a, b). Our findings confirmed that the crossbred mice exhibit classic ALS symptoms, including weakened forelimbs, hind limbs and poor motor coordination (Gurney et al., 1994). Starting at two months of age, mutants performed significantly worse than controls in both tests, which aligns with the typical onset of symptoms in the SOD1(G93A) model (Gerber et al., 2012, Mancuso et al., 2011, Mead et al., 2011). The hanging wire test indicated a progressive decline in strength, with the mice nearly unable to hold onto the grid at the end stage (Fig. 18a). Rotarod testing revealed markedly impaired motor coordination in mutant mice beginning around three months of age (Fig. 18b).

We also compared the performance of our crossbreed with the original SOD1/C57Bl6 strain. Interestingly, we found notable differences in the performance during the symptomatic stage (Fig. 18c, d). Both strains had similar strength in forelimbs and hind limbs until the onset, but SOD1/GFAP/EGFP mice experienced a more rapid decline in overall condition (Fig. 18c). Motor coordination, assessed by the Rotarod test, was also more severely affected in SOD1/GFAP/EGFP mice. By three months, their performance resembled the final stage of SOD1/C57Bl6 mice (Fig. 18d).

Thus, while the onset of symptoms is similar in both strains, the progression of the phenotype differs. SOD1/GFAP/EGFP mice deteriorate more quickly, reaching the "final stage" of the original model about a month earlier. Our data suggest that although genetic background does not influence the onset of the disease, it does affect the rate of progression and overall symptom severity.

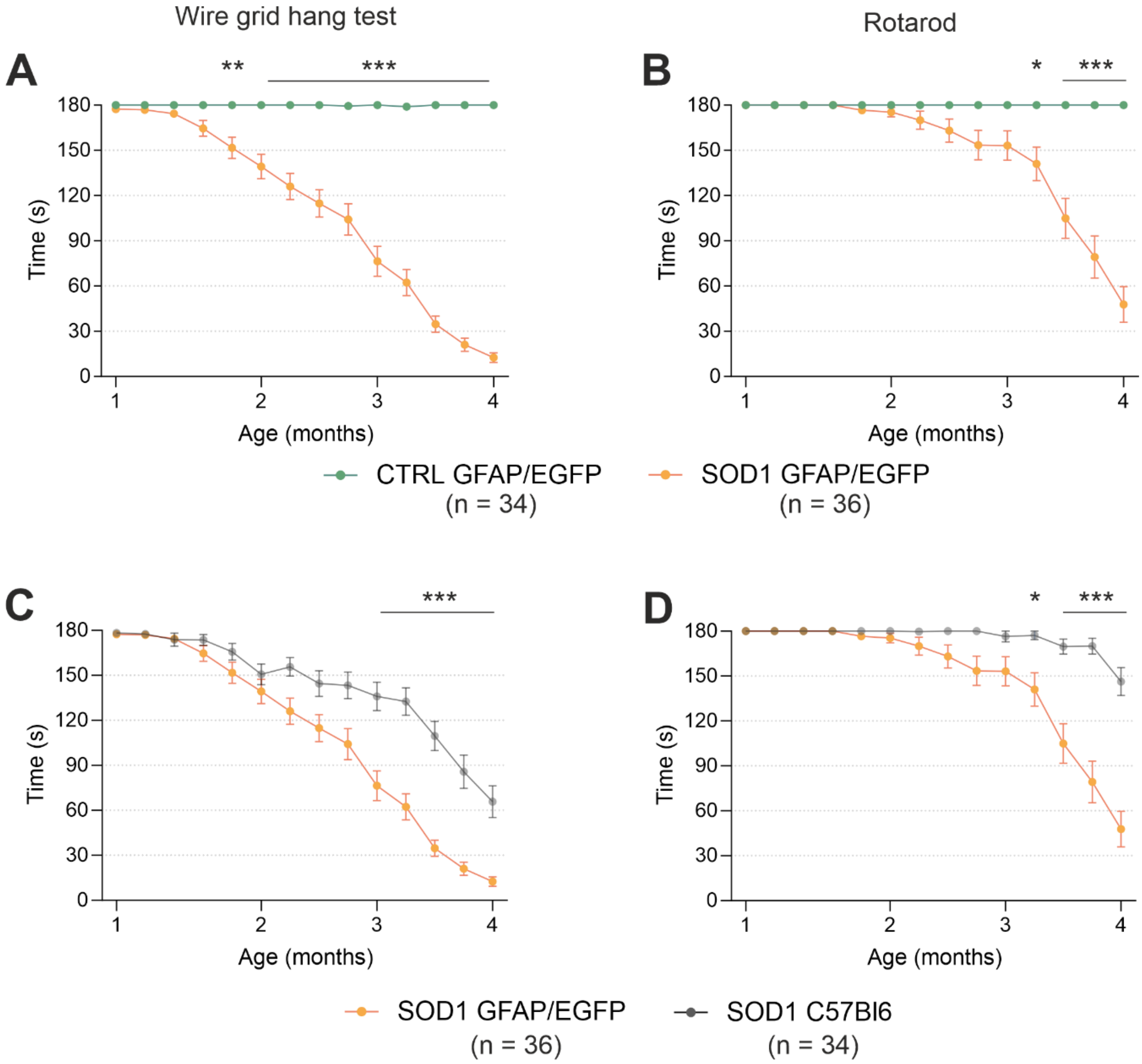

Fig. 18 Evaluation of pathology by behavioral testing A) The hanging wire test confirmed a motor strength decline in SOD1/GFAP/EGFP mice compared to CTRLs. B) Rotarod measurements analysis revealed the decline of motor coordination in SOD1/GFAP/EGFP mice compared to CTRLs thus confirming the ALS phenotype. C) Comparison of motor strength revealed significantly faster progression in SOD1/GFAP/EGFP mice compared to the initial SOD1/C57BL6. D) Similar trends were observed in Rotarod results, showing a faster decrease in motor coordination in SOD1 GFAP/EGFP mice. Data are presented as mean ± SEM. n = the number of mice.

4.2.2 Identification of Astrogliosis and Kir4.1 Downregulation in the Spinal Cord

Astrogliosis was previously described in the spinal cord of the original model (Miller et al., 2017, Guttenplan et al., 2020); however, we did not confirm it in the motor cortex (Filipi et al., 2023). In the SOD1/GFAP/EGFP model, we took advantage of the eGFP-labeling and performed fluorescence analysis in the motor- the somatosensory cortex, and the ventral horns of the lumbar spinal cord, looking for signs of astrogliosis. To ensure that we analyzed the whole area of interest, we employed the tile scanning technique (see Fig. 19a, c). 120 ± 3 days old mice were used for this analysis.

The results from the motor and somatosensory cortex (Fig. 19b) revealed a significantly larger fluorescent area in the SOD1 mice, and we observed the same situation in the ventral horns of the lumbar spinal cord (Fig. 19d). This data suggests a higher GFAP positivity (thus a visible change in morphology and/or increase of GFAP-positive cells) caused by ALS-like pathology, which confirms that astrocytes are activated in both the brain and spinal cord during the disease progression in the SOD1 model on the FVB/N background.

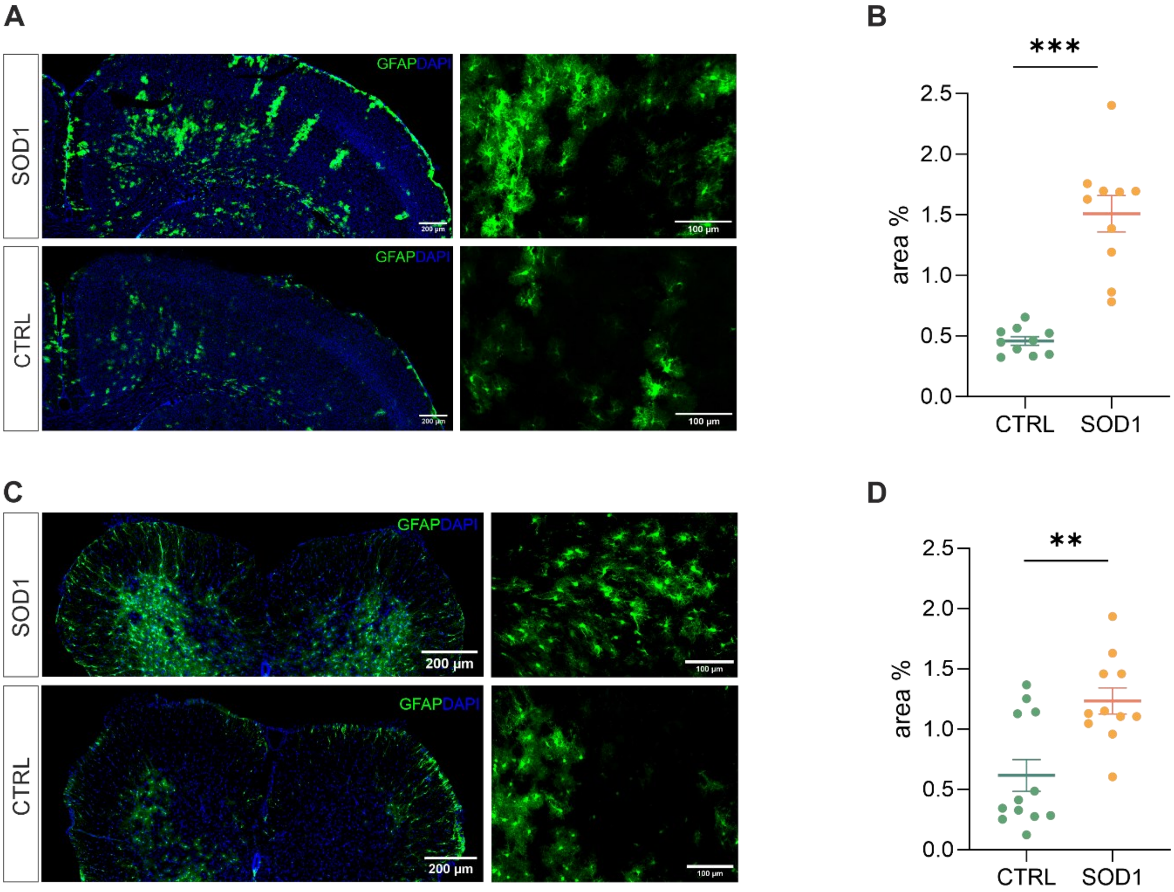

Fig. 19 Assessment of astrocytic reactivity based on GFAP expression levels A) Representative tile scans of the motor cortex used for fluorescence analysis. The SOD1 cortex is showing signs of astrogliosis. B) Fluorescence analysis in the motor and somatosensory cortex of SOD1 and CTRLs

showed a significantly larger fluorescent area in the SOD1 sample, which suggests the presence of astrogliosis and a morphological shift of astrocytes towards a reactive shape in SOD1 mice. C) Representative pictures of astrocytes in the ventral horns of the spinal cord. D) Fluorescence analysis in the spinal cord of SOD1 mice revealed a significantly higher fluorescent area, which suggests astrogliosis and a morphological shift of astrocytes towards a reactive shape. Data are presented as mean ± SEM. n = the number of brain hemispheres or spinal cord slices, respectively. CTRL, control mice on the FVB/N background; SOD1, superoxide dismutase transgenic mice on the FVB/N background.

In addition to morphology, we were interested in the Kir4.1 expression (Fig. 20a). Kir4.1 is predominantly expressed in astrocytes and belongs to the family of Kir channels, which are responsible for maintaining the resting membrane potential and regulating K^+ homeostasis in these cells. This channel undergoes downregulation in numerous CNS pathologies (Wilcock et al., 2009, Harada et al., 2013, Hanani and Spray, 2020) including ALS (Bataveljic et al., 2012). Nevertheless, as the behavioral tests indicated, different genetic backgrounds can cause discrepancies, and we thus employed immunohistochemistry followed by fluorescence analysis to assess the expression in the SOD1/GFAP/EGFP mice. We examined the protein expression in the motor and the somatosensory cortex as well as in the spinal ventral horns of 120 ± 3-day old SOD1/GFAP/EGFP and CTRL/GFAP/EGFP mice.

Our results show that there is no significant difference between Kir4.1 expression in the cortex, as the obtained values were almost equal in both SOD1 and CTRL mice (Fig. 20b). However, the fluorescence analysis in the ventral horns of the spinal cord showed significant downregulation of the Kir4.1 channel (Fig. 20c).

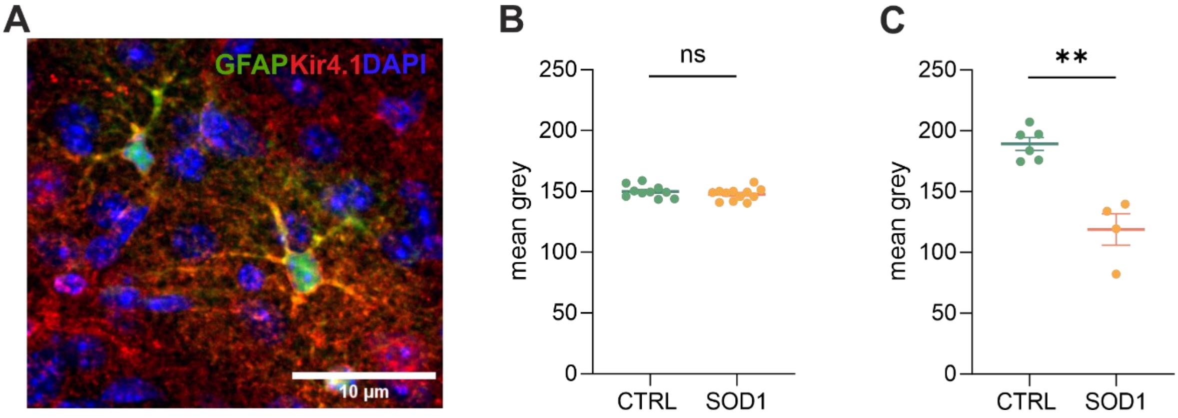

Fig. 20 Immunohistochemical analysis of Kir4.1 expression A) A representative picture of Kir4.1 staining in the motor cortex. B) Fluorescence analysis of Kir4.1 in the primary and secondary motor cortex and somatosensory cortex. C) Fluorescence analysis of Kir4.1 in the ventral horns of the spinal cord. Data are presented as mean ± SEM. n = the number of brain hemispheres or spinal cord slices,

respectively. CTRL, control mice on the FVB/N background; SOD1, superoxide dismutase transgenic mice on the FVB/N background.

4.2.3 Astrocytic Swelling During Hyperkalemia

The analysis of EGFP fluorescence in the SOD1/GFAP/EGFP mice revealed morphological changes in both cortical and spinal astrocytes suggesting their shift towards an activated state. Furthermore, the evaluation of Kir4.1 expression revealed downregulation in the ventral horns; lumbar spinal cord of SOD1 mice. We aimed to explore whether these changes will be associated with astrocytic swelling/volume regulation, specifically during hyperkalemia. As K^+ levels tend to be higher during pathological stages, we thus conducted an experiment measuring astrocytic swelling/volume regulation during exposure to different K^+ concentrations. We used 20 mM and 50 mM $aCSF_{K+}$ solutions to simulate elevated K^+ levels occurring e.g. during closed brain injury and ischemia, respectively (Rossi et al., 2007, Muller and Somjen, 2000, Pietrobon and Moskowitz, 2014). The measurements were done using acute brain and spinal cord slices from SOD1/GFAP/EGFP and CTRL/GFAP/EGFP mice. The slices were exposed to either 20mM or 50mM $aCSF_{K+}$ for 20 minutes followed by a 40-minute application of aCSF (further termed as washout). Changes in astrocytic volume were recorded every 5 minutes during the application and every 20 minutes during the washout (Fig. 21a). Astrocyte volume at $t = 0$ was set to 100 % and the swelling was expressed relative to this baseline as an increase in percentage. 120 ± 3 days old mice were used for the analysis.

Volume changes of cortical astrocytes were measured specifically in the motor and the somatosensory cortex of acute brain slices. Despite the observed astrogliosis, the measurements and following data analysis revealed that SOD1 cortical astrocytes can handle higher K^+ levels with the same efficacy as healthy astrocytes during both 20 and 50mM K^+ application (Fig. 21b, c). After the initial measurements cells swelled up to ~190 % and almost ~340 % respectively. All cells were able to recover their volume in the following 40 minutes, suggesting there is no impairment in K^+ level maintenance.

Spinal astrocytes were measured in the ventral horns of the lumbar spinal cord. The results of our measurements show that the SOD1 spinal astrocytes have unimpaired buffering ability in the 20 mM K^+ environment (Fig. 21d) and sustain homeostasis comparable to healthy cells. However, during the application of the 50 mM $aCSF_{K+}$ the SOD1 astrocytes swelled significantly less than the CTRL astrocytes at each recorded time point during the application (Fig. 21e). While the SOD1 astrocytes swelled up to only ~ 275 %, the CTRL astrocytes swelled to ~400 % of their original volume. The diminished swelling in the high K^+ environment suggests inefficient buffering of the extracellular K^+ level and a potential K^+ homeostasis imbalance in the SOD1 spinal cord.

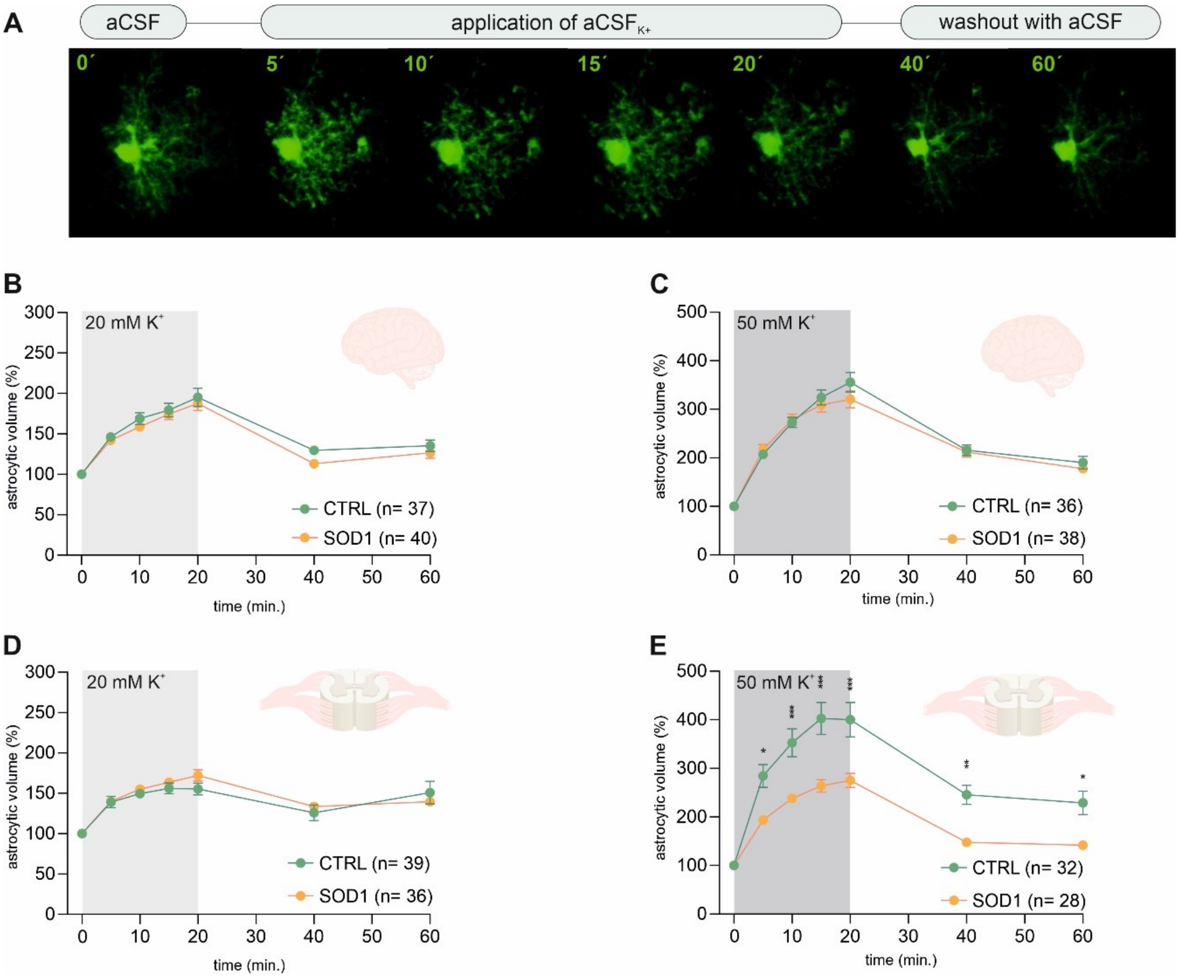

Fig. 21 Swelling of astrocytes in response to different K^+ concentrations A) Superimposed confocal images of an eGFP-labeled cortical astrocyte were recorded throughout the measurement. A control image was taken during the application of artificial cerebrospinal solution (aCSF). The volume of astrocytes was recorded every 5 min during the application of aCSF$_{K+}$ for 20 min. The last 2 stacks of astrocyte images were recorded at an interval of 20 min during 40-min in aCSF. B, C) The time course of volume changes of cortical (B) and spinal (C) astrocytes throughout the measurement in 20mM aCSF$_{K+}$. D, E) time course of volume changes of cortical (D) and spinal (E) astrocytes throughout the measurement in 50mM aCSF$_{K+}$. Data are presented as mean ± SEM. n = number of cells. CTRL, control mice on the FVB/N background; SOD1, superoxide dismutase transgenic mice on the FVB/N background.

4.2.4 Impact of Hyperkalemia on ECS Diffusion Parameters

To investigate alterations in the dynamics of the ECS diffusion properties, we used the RTI method in the brain and spinal cord of 120 ± 3 day old SOD1/GFAP/EGFP mice. We hypothesized that the alterations in astrocyte morphology and their functional properties detected by 3D-morphometry could also be manifested as variations in the ECS parameter values. To address this, we used the same experimental protocol as for the earlier 3D-morphometry (described in detail in Methods). Briefly, brain and spinal cord slices from SOD1/GFAP/EGFP and CTRL/GFAP/EGFP were exposed to two distinct $aCSF_{K+}$ concentrations (20mM and 50mM) separately, for 20 minutes, followed by a 40-minute washout period with aCSF. The ECS parameters were monitored at 5-minute intervals throughout both the application phase (20 minutes) and the subsequent washout period (40 minutes). The quantification of the ECS parameter volume fraction (α) and tortuosity (λ) were carried out in the cerebral milieu of the motor cortex and the ventral horns of the spinal cord.

The initial values measured during physiological conditions (prior to high K^+ application) in the cortex of CTRL mice ($\alpha = 0.189 \pm 0.006$, $\lambda = 1.59 \pm 0.05$, $n = 16$, expressed as mean ± SEM) were not significantly different from those acquired in SOD1 mice ($\alpha = 0.195 \pm 0.006$, $\lambda = 1.64 \pm 0.04$, $n = 18$). The application of 20mM $aCSF_{K+}$ (Fig. 22a, b) then induced cell swelling leading to a shrinkage of the ECS volume, manifested as a compensatory decrease of the ECS volume fraction (α: CTRL 0.122 ± 0.006, SOD1 0.128 ± 0.005, $p < 0.0001$), while no significant changes in tortuosity were detected (λ: CTRL 1.605 ± 0.03, SOD1 1.677 ± 0.03). During the washout, the ECS volume fraction fully recovered to initial values in both the CTRL and SOD1 mice or even exceeded them but no significant differences between groups were found.

The exposure of brain slices to 50mM $aCSF_{K+}$ (Fig. 22c, d) revealed a statistically significant decrease in the volume fraction in both groups ($p < 0.001$) compared to the initial values, with no significant difference observed between CTRL ($\alpha = 0.072 \pm 0.01$, $n = 9$) and SOD1 mice ($\alpha = 0.095 \pm 0.02$, $n = 9$). Tortuosity was not significantly affected by the 50mM $aCSF_{K+}$ application and the maximum values reached in the 20th min of application did not differ between CTRL and SOD1 mice either (λ: 1.73 ± 0.05 and 1.75 ± 0.05, respectively). During the subsequent washout, we observed a complete recovery of the volume fraction in both groups.

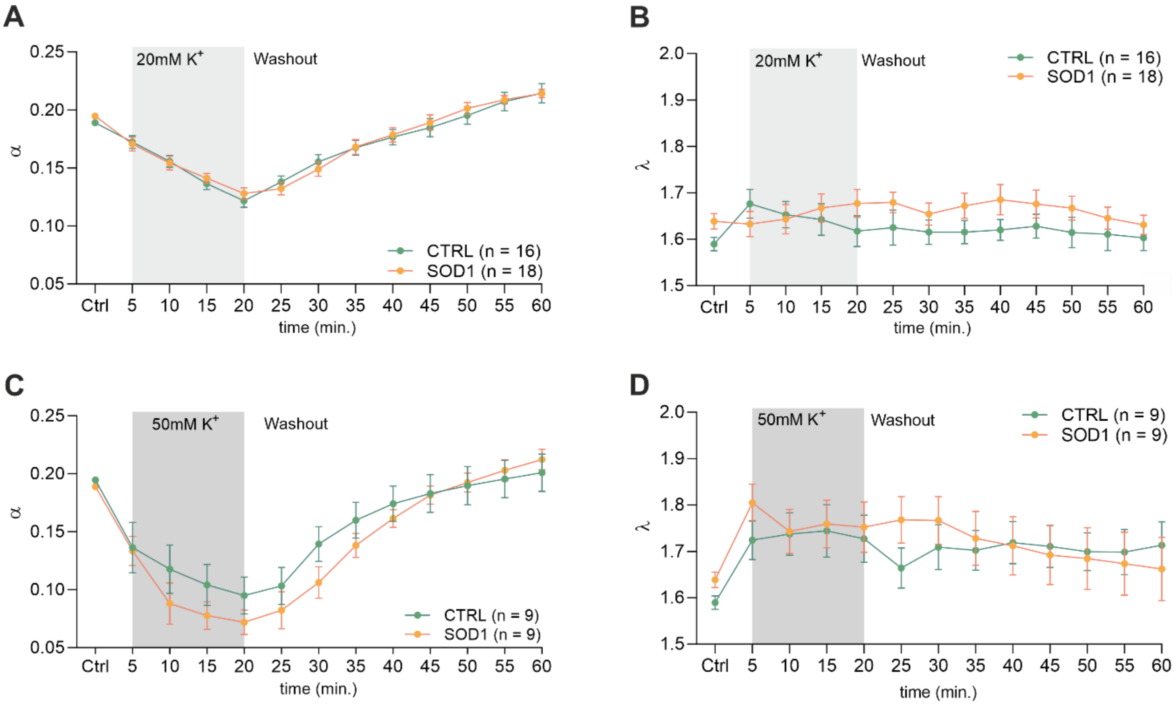

Fig. 22 Measurements of ECS parameters in mouse acute brain slices averaged data of α – volume fraction and λ - tortuosity measured in CTRL and SOD1 mice in resting conditions (22-24°c, CTRL) and at 5-minute intervals during application of 20mM (A, B) or 50mM (C, D) $aCSF_{K+}$ and washout (aCSF). Data are presented as mean ± SEM. n = the number of slices. Ctrl, control (initial measurements); CTRL, control mice on the FVB/N background; SOD1, superoxide dismutase transgenic mice on the FVB/N background.

The initial measurements during physiological conditions (prior to high K^+ application) in the spinal cord showed no differences of the ECS volume fraction or tortuosity between the compared groups (CTRL: $\alpha = 0.193 \pm 0.007$, $\lambda = 1.68 \pm 0.05$; SOD1: $\alpha = 0.196 \pm 0.003$, $\lambda = 1.75 \pm 0.07$). Following exposure of the spinal cord tissue to 20mM $aCSF_{K+}$, the volume fraction decreased from the initial values in both experimental groups (CTRL: $\alpha = 0.164 \pm 0.003$, n = 8, SOD1: $\alpha = 0.151 \pm 0.008$; $p < 0.001$, n = 9) but the maximum decrease reached in the 20th min did not differ between the groups (Fig. 23a, b). No changes from the initial values were detected either in tortuosity (CTRL: $\lambda = 1.76 \pm 0.04$; SOD1: $\lambda = 1.81 \pm 0.02$). The washout resulted in full recovery of the ECS volume in both groups: CTRL ($\alpha = 0.195 \pm 0.004$) and SOD1 ($\alpha = 0.196 \pm 0.009$).

Exposure of the spinal cord slices to 50mM $aCSF_{K+}$ resulted in a significantly more profound decrease in the ECS volume fraction in CTRL (n = 6) compared to SOD1 (n = 6) mice ($\alpha = 0.130 \pm 0.01$ and 0.171 ± 0.008, respectively). In addition, this decrease was faster in CTRL mice ($p < 0.0001$ already in 10th min) than in the SOD1 group ($p = 0.03$ in 20th min) (Fig. 23c). Full recovery of ECS volume fraction was detected in CTRL mice (α =

0.189 ± 0.005), while in SOD1 mice the values at the end of the washout exceeded the initial values, indicating that the ECS volume after washout was larger than before application (α = 0.226± 0.011, *p* = 0.0006). Interestingly, perfusion with 50mM aCSF$_{K+}$ evoked a steep increase in tortuosity values in CTRL mice ($p < 0.0005$), however, there was no significant difference when comparing to tortuosity values obtained from SOD1 (Fig. 23d).

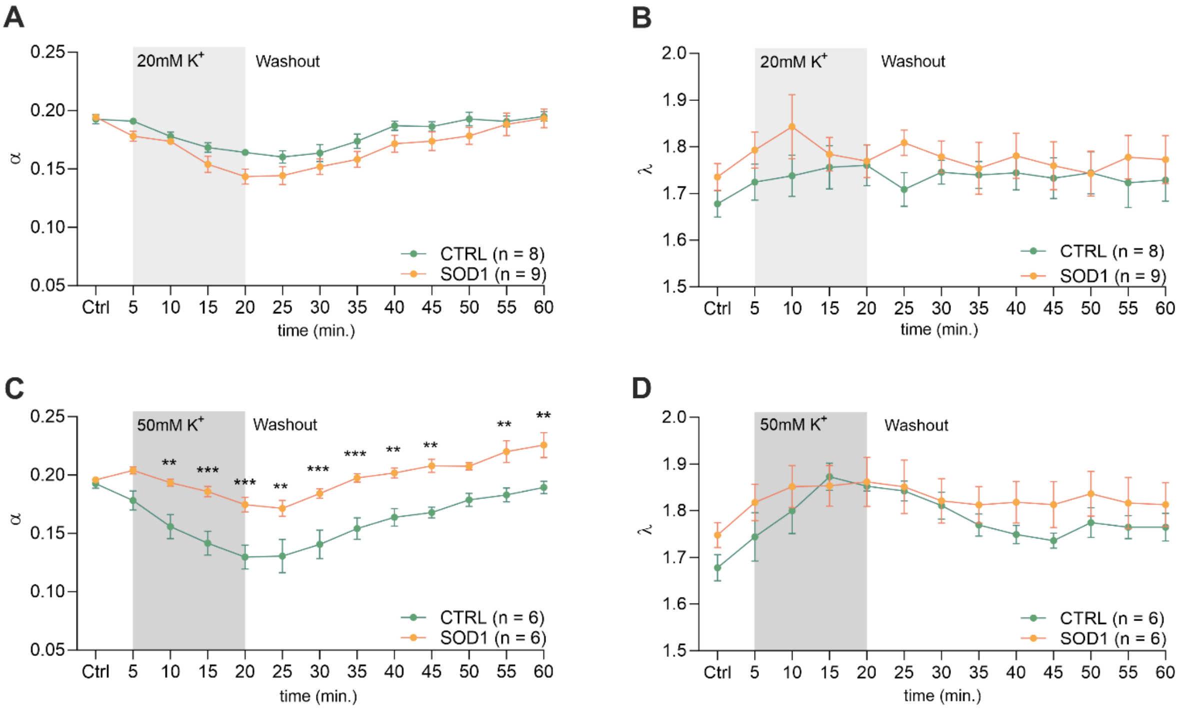

Fig. 23 Measurements of ECS in acute spinal cord slices averaged data of α – volume fraction and λ - tortuosity measured in CTRL and SOD1 mice at resting conditions (22-24°c, Ctrl), and at 5-minute intervals during application of 20mm (A, B) and 50mm (C, D) aCSF$_{K+}$ and washout (aCSF). Data are presented as mean ± SEM. n = the number of slices. Ctrl, control (initial measurements); CTRL, control mice on the FVB/N background; SOD1, superoxide dismutase transgenic mice on the FVB/N background.

4.2.5 Potassium Concentration in the CSF of SOD1/GFAP/EGFP Mice

Altogether, the data from functional measurements and immunohistochemical analysis suggested that the SOD1/GFAP/EGFP mice could suffer from K^+ imbalance. Higher K^+ levels are associated with pathological stages, however, to the best of our knowledge, the actual K^+ concentration in the cerebrospinal fluid of SOD1/C57Bl6 or the SOD1/GFAP/EGFP mouse model is not yet known. To determine the extracellular K^+ concentration and reveal possible ion deregulation, we examined the concentration of potassium and other elements in the cerebrospinal fluid (CSF) of the 120 ± 3 day old SOD1/GFAP/EGFP mice. Specifically, we employed electrothermal vaporization (ETV) coupled with inductively coupled plasma optical emission spectrometry (ICP-OES) and measured CSF samples collected from CTRL and SOD1 mice. The CSF was isolated using a protocol adapted from (Kaur et al., 2023), and only clear samples without any traces of blood (Fig. 24a) were processed and analyzed. In addition to K, we also analyzed Ca, Fe, Mg, Na, P and S (Table 3). The K^+ concentration in the CSF from SOD1 mice was comparable to values in CTRLs (Fig. 24b) and both were within the range of the physiological concentration, which can vary slightly depending on factors like age or experimental condition, but is typically ~3 mmol/l (Larsen et al., 2016). Interestingly, we detected a significantly lower concentration of magnesium in the CSF of SOD1 mice (Fig. 24c). Magnesium is among others involved in muscle function and neuronal signaling, and a lower magnesium concentration has been reported in post mortem analysis of ALS patients previously (Yasui et al., 1997). Concentrations of other tested elements did not differ between the controls and mutated mice.

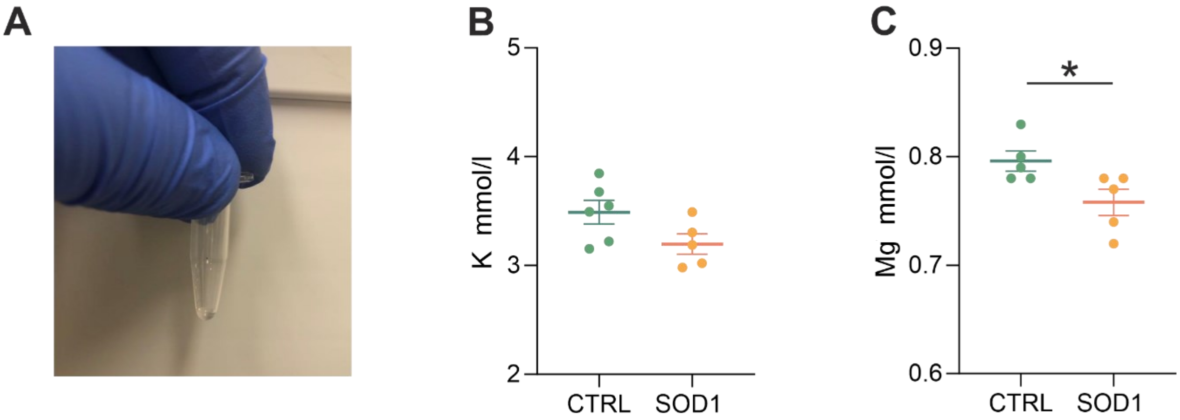

Fig. 24 Elemental analysis of CSF isolated from GFAP/EGFP mice A) a sample of CSF demonstrating the purity of all samples used for the analysis. B) A comparison of K concentrations in the CSF of control vs. SOD1 mice. C) A comparison of Mg levels in the CSF of control vs. SOD1 mice. Data are presented as mean ± SEM. n = the number of mice. CTRL, control mice on the FVB/N background; SOD1, superoxide dismutase transgenic mice on the FVB/N background.

Tab. 3 Concentration of elements in the CSF of GFAP/EGFP mice

mM/l	SOD1	CTRL
Ca	1.12 ± 0.1	1.25 ± 0.05
Fe	0.01 ± 0.01	0.01 ± 0.01
K	3.20 ± 0.21	3.49 ± 0.26
Mg	0.76 ± 0.03	0.81 ± 0.05
Na	152.20 ± 2.53	149.73 ± 7.64
P	1.38 ± 0.24	1.45 ± 0.14

S	0.68 ± 0.25	0.83 ± 0.2

4.3 Functional Properties of Astrocytes in the Model of Alzheimer´s disease

The swelling of ALS astrocytes was disrupted during hyperkalemia and the cells were generally affected by the pathology and became reactive. ALS and AD share some pathological features such as the presence of a specific disease-associated subpopulation (Keren-Shaul et al., 2017) and the activation of astrocytes, especially in the proximity of Aβ plaques. We were therefore also interested in the functional properties of astrocytes in the model of AD.

We tested the ability of astrocytes to regulate their volume and swell in acute brain slices from 3M, 9M, 12M and 18M mice exposed to either hypotonic solution (aCSF$_{H-100}$) to evoke a hypo-osmotic stress or a potassium solution (aCSF$_{K+}$) to evoke a severe hyperkalemia. The 20-min exposure was followed by a 40-min application of aCSF (further termed washout). Changes in the total astrocytic volume (ΔVc) were recorded every 5 minutes throughout the aCSF$_{H-100}$ or aCSF$_{K+}$ application and every 20 minutes during the washout. The astrocyte volume was set to 100 % before the application and the astrocytic swelling was expressed relative to this baseline as a percentual increase/decrease.

Kolenicova et al. (2020) showed that the swelling of astrocytes induced by hyperkalemia varies with age. While in 3 and 12M animals astrocytes swelled distinctly (up to a maximum of ~170 % in 3M old mice), in 9- and 18M mice, the swelling was lower (maximum ~140 % in 18M old mice) (Figure 25 a, d). Such differences were not observed under exposure to hypo-osmotic stress, reflecting that hyperkalemia activates different mechanisms responsible for astrocyte swelling than hypo-osmotic stress. In addition, we did not detect any age-dependent cell volume variations in 3xTg-AD astrocytes in response to hyperkalemia. We only observed minor differences between the age groups (Figure 25). Similar to physiological aging, hypo-osmotic stress did not reveal any age-related differences in the swelling of 3xTg-AD astrocytes (Figure 25)

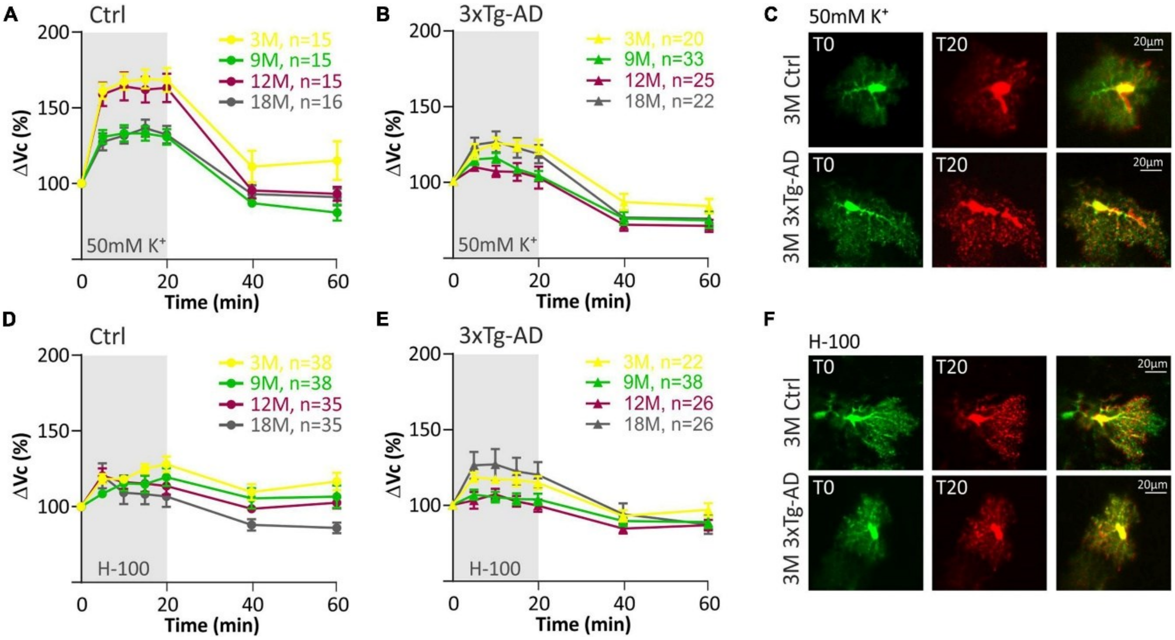

Fig. 25 Swelling of hippocampal astrocytes in response to severe hyperkalemia (50 mM K^+) or hypo-osmotic stress in aging controls and 3xTg-AD mice. A, B) time course of the total volume changes (δvc) in EGFP-positive cells during a 20-min application of $aCSF_{k+}$ and a 40-min washout. Note that in controls (left) the astrocyte swelling is comparable in 3M- and 12M- and in 9M- and 18M-old animals. No such age-related changes were observed in 3xTg-AD mice (right). C) Representative images of EGFP-expressing astrocytes before (T0, green) and after the 20-minute exposure to 50 mm K^+ (T20, red). Overlays show merged images of cells with their initial volume (green) and swollen cells (red). The red area represents swelling induced by 50 mM k^+. D, E) time course of the total volume changes (δv_c) in EGFP-positive cells during a 20-min application of $aCSF_{h-100}$ and a 40-min washout. No changes were observed between age groups in either controls or 3xTg-AD. F) Representative images of EGFP-expressing astrocytes before (T0, green) and after the 20-min exposure to H-100 (T20, red). Overlays show merged images of cells with their initial volume (green) and swollen cells (red). The red area represents swelling induced by H-100. Data are presented as mean ± SEM. Statistical significance was determined by two-way ANOVA test with Tukey's *post hoc* test. n, number of cells.

The volume changes evoked by the hypo-osmotic stress in 3M and 18M 3xTg-AD animals did not differ from their age-matched controls. In 3M mice ΔVc reached the maximal values of ~120 % in the controls, and ~121 % in the 3xTg-AD (Figure 26a). In 18M mice it was ~118 % in the controls and ~121 % in 3xTg-AD mice (Figure 26d). However, significant differences between the controls and 3xTg-AD mice were observed in both 9- and 12M. In 9M mice, the astrocyte volume increased to ~128 % in the controls, while it reached only ~108 % in 3xTg-AD after 20 minutes of $aCSF_{H-100}$ application (Figure 26b). In 12M mice, the volume increased to the maximum values of ~119 % in the controls and ~109 % in 3xTg-AD (Figure 26c).

Overall, we discovered that astrocyte swelling caused by both hypo-osmotic stress and hyperkalemia was lower in the 3xTg-AD animals than in their age-matched controls. In addition, the astrocytic swelling in the AD model did not change with increasing age.

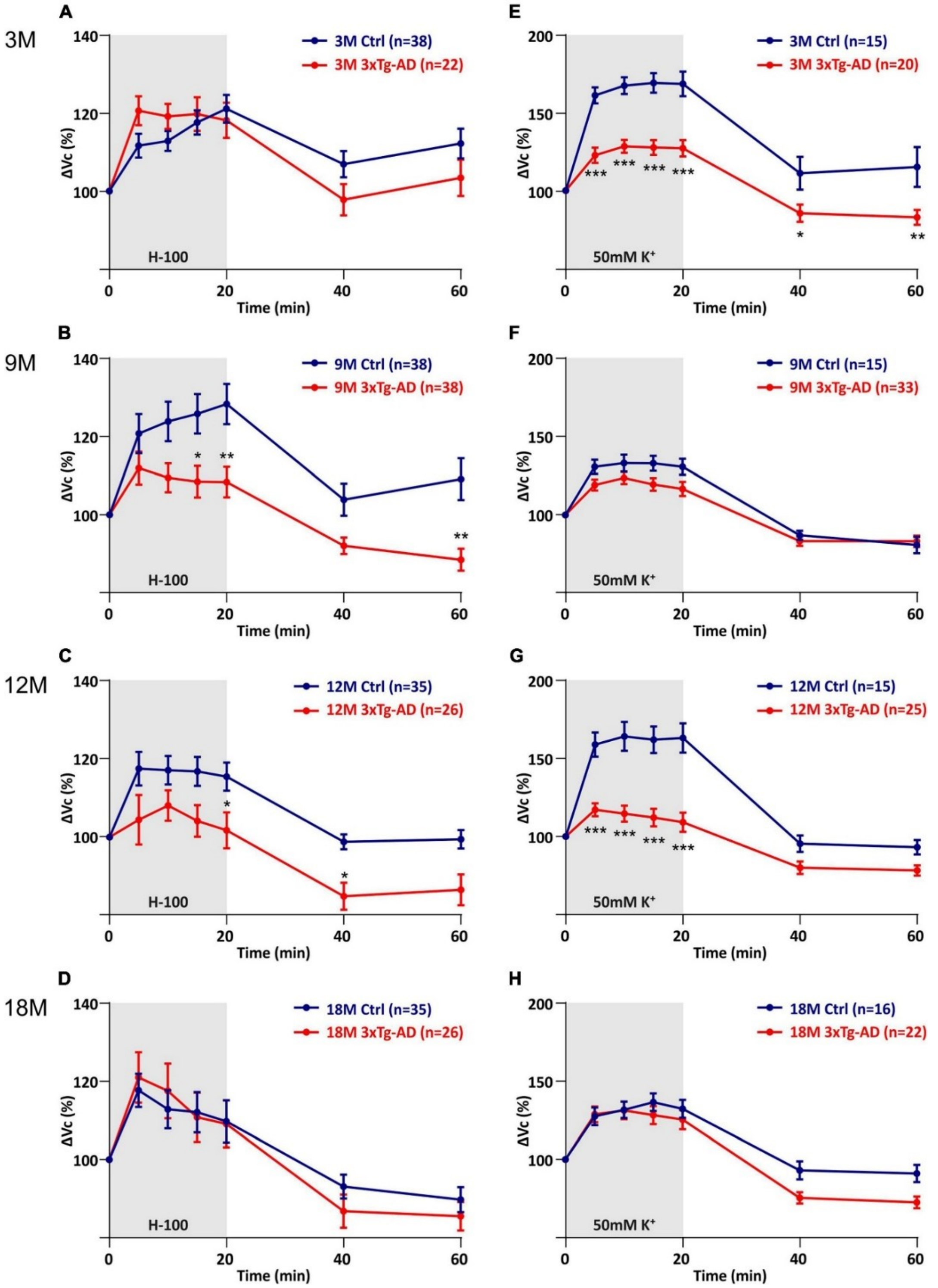

Fig. 26 Comparison of astrocytic swelling in controls and 3xTg-AD during exposure to hypo-osmotic stress or hyperkalemia (50 mM K^+). A–D**)** Time course of the total volume changes (ΔVc) in EGFP-

positive cells during a 20-min application of $aCSF_{H-100}$ and a 40-min washout. Note that the astrocyte swelling is comparable in 3M- and 18M-old animals, while the astrocytic swelling in 9M- and 12M-old controls significantly exceeded the swelling in 3xTg-AD. E–H) Time course of the total volume changes (ΔVc) in EGFP-positive cells during a 20-min application of $aCSF_{K+}$ and a 40-min washout. Note that the astrocyte swelling is comparable in 9M- and 18M-old animals, while the astrocytic swelling in 3M- and 12M-old controls significantly exceeded the swelling in 3xTg-AD. Data are presented as mean ± SEM. Statistical significance was determined by two-way ANOVA with Tukey's multiple comparison test. Asterisks indicate significant differences ($^*p < 0.05$, $^{**}p < 0.01$, $^{***}p < 0.001$). n, number of cells.

4.3.1 Diffusion Parameters in the Hippocampus of AD Mouse Model

We wondered whether morphological changes of individual cellular elements or changes in the composition of the ECM during AD, might affect the volume and diffusion properties of ECS. To test the hypothesis, we performed measurements of the extracellular diffusion parameters in the CA1 region of hippocampal slices by the RTI method during exposure to the pathological models of hypo-osmotic stress and hyperkalemia.

First, we aimed to establish diffusion parameters in the hippocampus of mice aging physiologically (CTRL) and in 3xTg-AD mice. We identified a significant and continuous decrease of volume fraction (α) during physiological aging in the hippocampal CA1 region (3M - ~0.212; 9M - ~0.188; 12M - ~0.169; 18M - ~0.123); however, we did not detect an age-related decrease of α in 3xTg-AD mice (3M - ~0.212; 9M - ~0.188; 12M - ~0.199; 18M - ~0.197) (Figure 27a).

The values of λ had an increasing tendency to correlate with aging. In 18M mice, an additional increase of λ was detected and the value was significantly higher in comparison with all other age groups (3M - ~1.491; 9M - ~1.543; 12M - ~1.560 ± 0.017; 18M - ~1.695 ± 0.016). The data of the 3xTg-AD mice also showed that λ increases with age (Figure 27b). This increase was faster than in the control animals, and most pronounced in 12M and 18M mice (3M - ~1.511; 9M - ~1.562; 12M - ~1.650; 18M - ~1.736).

When comparing physiological aging with the AD animal model, the differences of α were not significant until 12 months of age and later, at 18M of age, the difference became extremely significant (Figure 27c). The λ was also significantly higher in 12M 3xTg-AD animals compared to age-matched controls; however, the difference disappeared in 18M (Figure 27c). Overall, physiological aging was accompanied by a decrease in ECS volume fraction, while this tendency was completely lost during AD progression. However, an increase in the number of obstacles observed in AD progression occurred earlier than in physiological aging.

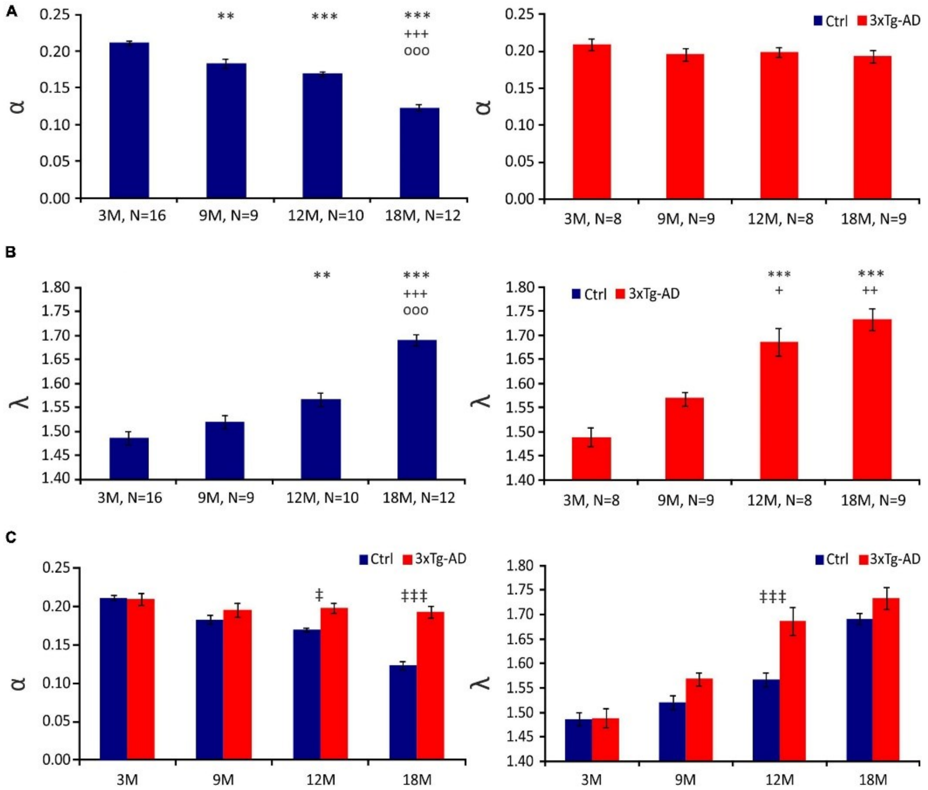

Fig. 27 Diffusion parameters of extracellular space during aging of CTRL and 3xTg-AD mice at 3, 9, 12 and 18M. Average values of the volume fraction α (A) and tortuosity λ (B) during aging in CTRL (left) and 3xTg-AD mice (right). Note the continuous decrease in α during physiological aging which is missing in 3xTg mice. A marked increase in λ occurred in 3xTg-AD animals earlier than in CTRL mice. C) Comparison of values of α (left) and λ (right) between CTRL and age-matched 3xTg-AD mice. Data are expressed as mean ± SEM. Statistical significance was determined by student's *t*-test with the Benjamini-Hochberg post-hoc test. Asterisks, crosses, circles and double daggers indicate significant differences ($p < 0.05$ [*/+/o/‡ significant]; $p < 0.01$[**/++/oo/‡‡ very significant]; $p < 0.001$ [***/+++/ooo/‡‡‡ extremely significant]). N, number of animals.

4.3.2 Impact of Hypo-osmotic Stress and Hyperkalemia on the Diffusion Parameters in the Hippocampus of AD Mouse Model

To further inspect the differences between 3xTg-AD mice and CTRLs, we evoked experimental cell swelling in brain slices by exposure to hypo-osmotic stress or severe hyperkalemia. The ECS diffusion parameters were determined during basal conditions and during a 20-min perfusion, followed by a 40-min washout. As the basal values of α and λ varied, we evaluated both the absolute and relative changes of the ECS parameters. To estimate the relative changes, the control values were set to 100 %, and the relative changes were calculated.

In all ages and groups, the hypo-osmotic stress induced a significant decrease in α with a complete or partial recovery during washout (Figure 28). Significant difference between the control and 3xTg-AD mice; however, occurred during the $aCSF_{H-100}$ application (the 20th minute) only in the 3M old animals, with α being lower in the control mice (~0.072) compared to 3xTg-AD mice (~0.116). At 18M of age, the basal value of α in 3xTg-AD mice was significantly higher than in controls but the difference disappeared during the application and reappeared only in the final three measurements during washout. During the washout in the CTRL animals, we detected a complete recovery of α in ages 3M, 9M, and 12M. For the 18M group the recovery was only partial. In 3xTg-AD mice, α fully recovered to basal values in 3M and 9M animals and partially recovered in 12M and 18M old mice.

To analyze the volume fraction recovery during the washout period further, we expressed the data as a percentage of volume increase/decrease in relation to the value of α reached in the 20th minute of application, which was set as 0 %. This analysis revealed a significant difference between the control and 3xTg-AD mice in the 20th minute of washout in 9M animals and the 40th minute of washout in 12M animals (Figure 28). These results indicate a slower and compromised recovery in the 3xTg-AD animals in 9M and 12M groups. Tortuosity increased during the application of $aCSF_{H-100}$ and returned to the basal values during washout in all tested groups. Altogether, changes in ECS volume fraction and tortuosity evoked by hypo-osmotic stress were comparable between the 3xTg-AD mice and their age-matched controls, but the recovery of ECS volume fraction in the 3xTg-AD mice was compromised in 9M and 12M animals.

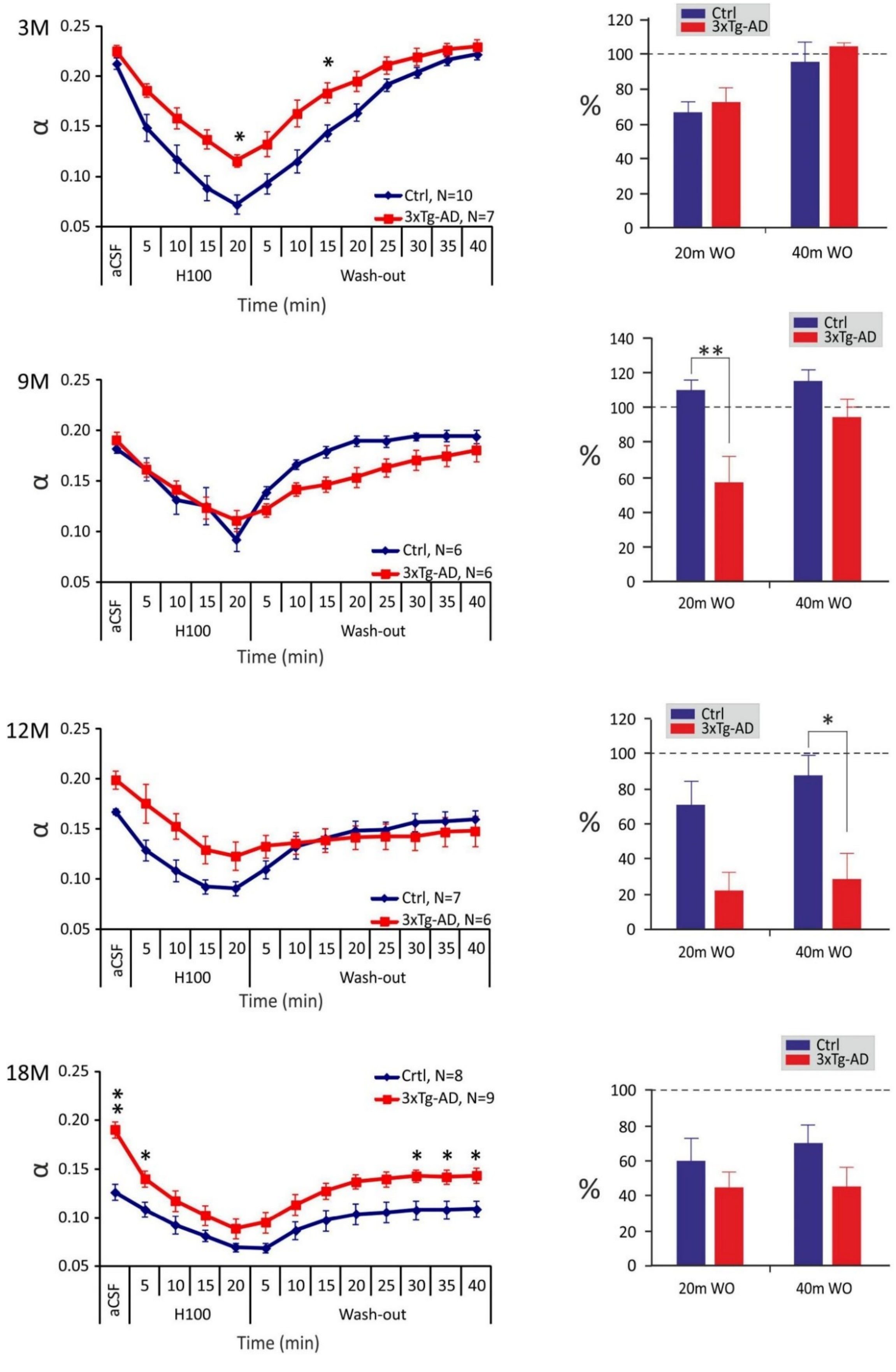

Fig. 28 Age-dependent changes of the absolute values of the ECS diffusion parameters in CTRL and 3xTg-AD mice evoked by hypo-osmotic stress. The left side: time course of the volume fraction (α) changes during aCSF$_{h-100}$ application and washout in 3-, 9-, 12- and 18M-old control animals and

age-matched 3xTg-AD mice. The right side: volume fraction recovery during washout at 20 min intervals expressed as changes in the values reached in the 20th min of application, set as 0%. Data are presented as mean ± SEM. Statistical significance was determined by two-way ANOVA test with Tukey's *post hoc* test. Asterisks indicate significant differences between ctrl and 3xtg-ad mice ($^{*}p < 0.05$, $^{**}p < 0.01$).

The application of the $aCSF_{K+}$ solution evoked a significant decrease of α in all the experimental groups, followed by a partial recovery towards basal values during washout. Interestingly, the ESC of 18M old control mice maintained the lower values of volume fraction even during washout and we did not detect any signs of recovery (Figure 29). We also did not see any significant differences at any time point during application, when comparing controls and 3xTg-AD mice. The analysis of recovery revealed a significant difference between controls and 3xTg-AD animals in the 20th and 40th min of washout in 18M animals (Figure 29). While the volume fraction in the oldest control animals did not recover at all, we detected partial recovery in the 3xTg-AD mice, presumably due to the higher initial α value. Severe hyperkalemia evoked an increase of λ in all experimental groups, followed by a recovery to basal values during washout. Overall, the changes in ECS volume fraction and tortuosity evoked by hyperkalemia, observed between the 3xTg-AD mice and their age-matching controls within 3 – 12M of age were comparable. However, in 18M 3xTg-AD mice, we detected a better recovery than in controls, but it was likely due to the higher initial ECS volume fraction value.

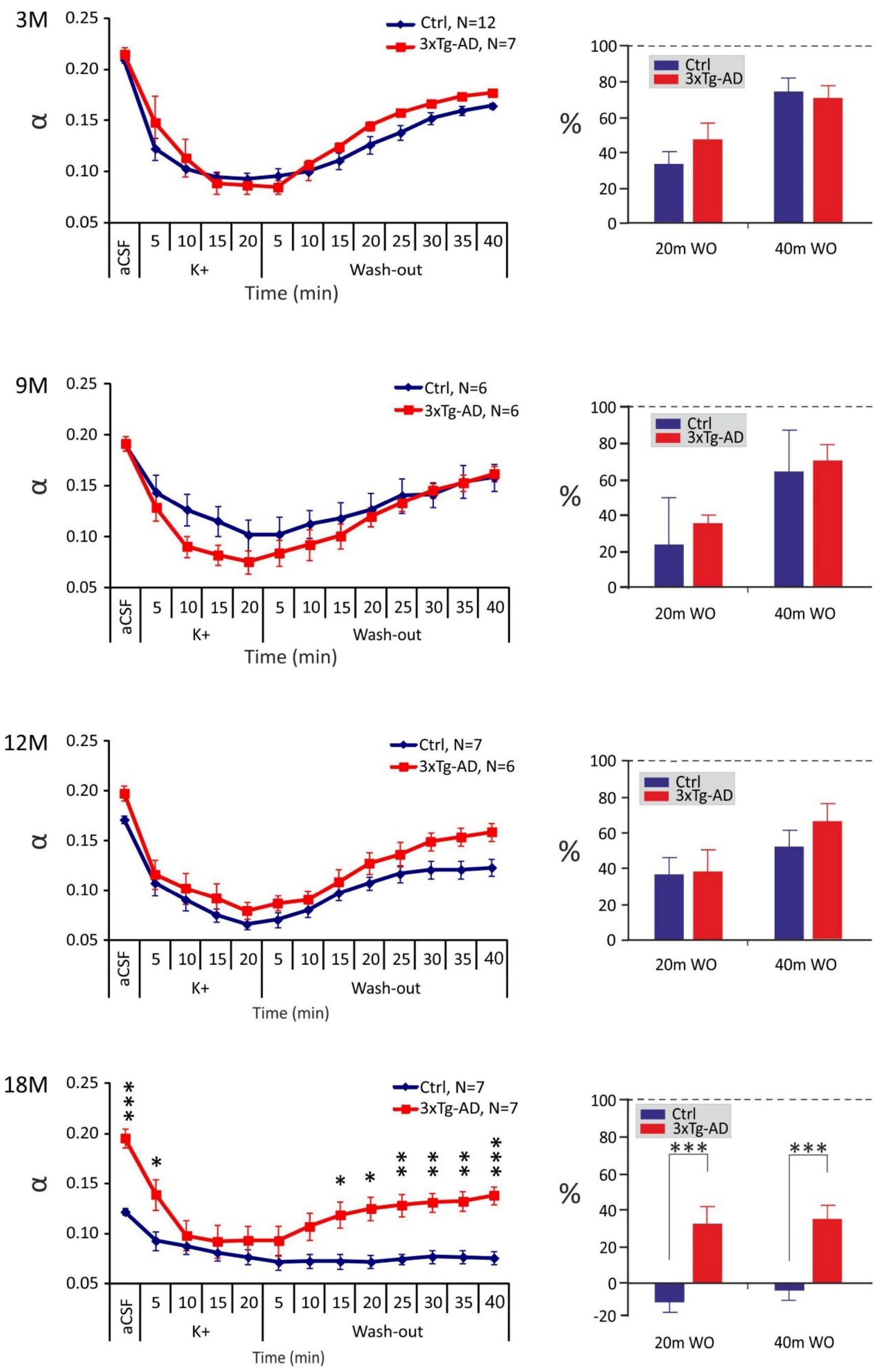

Fig. 29 Age-dependent changes of the absolute values of the ECS diffusion parameters in CTRL and 3xTg-AD mice evoked by severe hyperkalemia (50 mM K$^+$). The left side: time course of the volume fraction (α) changes during aCSF$_{K+}$ application and washout in 3-, 9-, 12- and 18M-old control

animals and age-matched 3xTg-AD mice. The right side: volume fraction recovery during washout at 20 min intervals expressed as changes in the values reached in the 20th min of application, set as 0%. Data are presented as mean ± SEM. Statistical significance was determined by two-way ANOVA test with Tukey's *post hoc* test. Asterisks indicate significant differences between CTRL and 3xTg-ad mice (*$p < 0.05$, $^{**}p < 0.01$, $^{***}p < 0.001$).

5 DISCUSSION

5.1 Characterization of the SOD1(G93A) Mouse Model Phenotype and Pathological Traits in the Motor Cortex

ALS is a fatal neurodegenerative disease with rapid progression and no efficient therapeutic strategies thus far. Over the years, various experimental models have been created to investigate the disease mechanisms, as well as to enable the search for possible therapeutic targets. The SOD1(G93A) stands out as the most used and thoroughly characterized mouse model in ALS research. However, despite its extensive use, the effect of pathological changes across different CNS regions remains incompletely understood.

Since ALS was first described, cortical pathological changes have been documented in patients, and monitoring cortical structural abnormalities has become a standard diagnostic procedure for this disease (Vucic et al., 2021). In addition to the death of cortical motor neurons, changes in glial cells have been observed, including microgliosis (Nolan et al., 2020, Jara et al., 2017, Dols-Icardo et al., 2020, Limone et al., 2024), accompanied by a DAM-like gene expression signature (Dols-Icardo et al., 2020), demyelination (Kang et al., 2013), and a shift in oligodendrocyte function from myelination to a neuro-supportive role (Limone et al., 2024).

While in humans the cortical changes are quite well-documented, less is known about the impact of ALS-like pathology on the cortex in the SOD1 mouse model. A study by Ozdinler et al. (2011) and others reported early cortical motor neuron degeneration, along with changes in glial cells (Miller et al., 2018, Gomes et al., 2019, Migliarini et al., 2021). Miller et al. (2018), Gomes et al. (2019), Gomes et al. (2020) discovered that reactive astrocytes in the SOD1(G93A) cortex differ from their spinal counterparts, yet still exhibit a toxic effect on neurons. However, Gomes et al. (2019) also reported no significant gene expression changes in microglia or oligodendrocytes. Additionally, some studies suggested that pathology in the SOD1 model is restricted to spinal and bulbar motor neurons, not affecting the motor cortex at all (Niessen et al., 2006). These conflicting findings raise questions about the extent to which the cortex is affected in the SOD1 mouse model and how accurately this model represents the cortical pathology ongoing in humans. We thus employed single-cell RNA-sequencing supported by immunohistochemistry to identify gene expression changes, the presence of disease-associated cell populations and morphological/pathological modifications in cortical glia that accompany the ALS-like pathology in the SOD1(G93A) model.

The ALS-like phenotype was confirmed through behavioral testing, highlighting sex-dependent differences in the disease progression, which were also confirmed by McCombe and Henderson (2010). The single-cell profiling focused on glial cells revealed minor changes in microglia and oligodendrocytes, but no significant ALS-related shifts in astrocytes, which contrasts with several studies that reported a reactive astrocyte phenotype (Miller et al., 2018, Gomes et al., 2019, Gomes et al., 2020). Although the only significantly dysregulated gene in the SOD1(G93A) model was the *Sod1*, gene set enrichment analysis (GSEA) indicated mitochondrial dysfunction in microglia and oligodendrocytes. Similar findings were recently observed by Liu et al. (2020) in oligodendrocytes isolated from the brainstem of 100-day-old SOD1 mice, suggesting potential dysregulation of energetic pathways.

Our data generated within the motor and primary somatosensory cortex regions, representing the end-point of the corticospinal tract affected by ALS, allowed us to also address questions regarding the site of origin and direction of ALS progression. Two main hypotheses exist, both supported by evidence (reviewed in van den Bos et al. (2019)). The 'dying forward' hypothesis suggests that ALS originates in the cortex and spreads towards the spinal cord MNs, whereas the 'dying back' hypothesis proposes that ALS begins within muscles or neuromuscular junctions. Considering the advanced ALS-like phenotype in end-stage SOD1 mice accompanied by the more pronounced changes observed in the brainstem and spinal cord, the milder cortical changes indicated by our data support the 'dying back' hypothesis in SOD1(G93A) mice. Interestingly, this contrasts with a report by Burg et al. (2020), which suggests that the cortex is the initiating point of ALS in SOD1(G86R) mice. These contradictory data emphasize the potential variability between different ALS models and might imply a differential effect of specific point mutations on the disease's character, necessitating further investigation.

The prior studies investigating the impact of the SOD1 mutation on the motor cortex have relied on measuring a limited number of genes and proteins (Gomes et al., 2019, Migliarini et al., 2021, Jara et al., 2017), or on analyzing bulk cell populations (Miller et al., 2018, Phatnani et al., 2013). This approach reduces the sensitivity of the analysis and limits the interpretability of the data. In our data, we utilized high-throughput scRNA-seq, enabling an in-depth analysis of small cell populations that bulk approaches cannot distinguish. Recent seminal studies using scRNA-seq have identified various disease-associated glial populations that play significant roles in disease progression (Keren-Shaul et al., 2017, Sala Frigerio et al., 2019, Habib et al., 2020, Falcao et al., 2018). Interestingly, many of these populations are present in multiple diseases, suggesting common mechanisms used by glial cells in response to pathological stimuli. For instance, a DAM-like population was identified not only in Alzheimer's disease but also in the spinal cord of the SOD1(G93A) mouse (Keren-Shaul et al., 2017) and in a spinal cord injury model (Matson et al., 2021). We searched for these populations, but without success, which confirms the minimal changes observed at the bulk transcriptional level and by immunohistochemistry. Generally, we found a largely similar cellular composition between control and SOD1(G93A) animals, with some exceptions in microglia and oligodendrocytes. We observed a slight increase in the proportion of activated microglia, suggesting an early phase of their activation, which was supported by immunohistochemistry, specifically by *bulbous termini* on microglial processes. More pronounced changes were observed in oligodendrocytes, where the sub-clustering analysis revealed a unique population characterized by increased expression of *Apoe* and *Il33*, specifically enriched in 4-month-old SOD1 samples. Considering the absence of significant oligodendrocyte loss or higher apoptotic rates in immunohistochemistry, we speculate about the active role of this oligodendrocyte population in disease progression. This would align with recent evidence suggesting an active role for oligodendrocytes in the progression of multiple sclerosis (Falcao et al., 2018) and in aging white matter (Kaya et al., 2022), which contrasts with their traditionally perceived passive role. However, we did not observe any expression patterns similar to previously reported disease-associated oligodendrocytes (Falcao et al., 2018, Kenigsbuch et al., 2022, Lee et al., 2021, Jakel et al., 2019), except for *Apoe* and *Il33*. This might however be due to the overall mild changes in gene expression observed throughout our data.

5.2 Functional Properties of Astrocytes in the Mouse Model of ALS

As aforementioned, glial cells play an active role in ALS onset and progression, which makes them promising targets for future therapeutic interventions. Astrocytes in particular, hold significant potential due to their crucial role in maintaining neural function and regulating the homeostasis of ions and neurotransmitters. To identify the best therapeutic strategy however, it is first essential to understand the changes in astrocytic functions caused by ALS pathology.

To better understand how functional properties are affected, we generated a mouse with ALS-like symptoms and fluorescently labeled astrocytes, which is advantageous for astrocyte-focused ALS studies. A similar strain has only recently become commercially available (https://www.jax.org/strain/013199), although without the labeled astrocytes. Our mice have FVB/N background, while the original SOD1(G93A) mice have C57Bl6 background. As mentioned previously, different backgrounds or point mutations seem to cause variability in the phenotype and indeed, our behavioral testing revealed notable differences in the disease progression between the original SOD1 model and the FVB/N background strain. Specifically, the animals on the FVB/N background experienced faster motor decline than those on the C57Bl/6 on both behavioral tests – wire grid hang and Rotarod. The researchers who provided this model to Jackson Laboratory also observed this. It is very likely that the genetic background is responsible for these differences, though the exact mechanisms remain unclear. Prior studies have shown that various ALS models exhibit phenotypic variations affecting disease progression, possibly due to factors such as microglia-mediated neuroinflammation (Heiman-Patterson et al., 2011, Nikodemova and Watters, 2011) or metabolic hyperactivity. Jackson Laboratory has reported hyperactive metabolism in the B6SJL background, including increased oxygen consumption, abnormal energy expenditure, and reduced circulating insulin levels (https://www.jax.org/strain/002726). Despite these differences, our SOD1/GFAP/EGFP mice still displayed hallmark ALS symptoms, making them a valuable model for further ALS research.

Since the different background affected the phenotype, we again performed fluorescence analysis to investigate the astrocytic morphology. The analysis confirmed ALS-like pathology at the cellular level, showing astrogliosis in both the ventral horns of the spinal cord and in the motor and somatosensory cortex. While astrocytic activation in the spinal cord was expected and is well-documented in the original SOD1/C57Bl6 model (Baker et al., 2015, Nagai et al., 2007), cortical astrocytes remain controversial. Some studies have confirmed astrocyte activation in the motor cortex of SOD1 mice (Gomes et al., 2019, Gomes et al., 2020, Miller et al., 2018), while others (Niessen et al., 2006) including us, did not observe any pathological changes, suggesting that the pathology might be confined to spinal and bulbar motor neurons in this model. To the best of our knowledge, no studies have examined astrocyte activation in the SOD1 model on an FVB/N background, limiting direct comparisons. However, given the faster disease progression observed in our model, it is possible that the astrogliosis was more pronounced and thus easier to detect than in the animals on the C57Bl/6 background.

Beyond changes in morphology, astrocytes in ALS exhibit alterations in gene expression associated with their key functions such as glutamate uptake and potassium buffering (Baker et al., 2015, Ferraiuolo et al., 2011, Miller et al., 2018). To explore the latter, we took advantage of the fluorescently labeled astrocytes in our model and measured the swelling during exposure to elevated extracellular potassium. The swelling reflects astrocytic ability to uptake K^+, which contributes to maintaining the potassium homeostasis. Under normal physiological conditions, potassium concentration in the nervous system is ~3 mM, but it increases during pathological conditions such as ischemic stroke, traumatic brain injury, and epileptic seizures (Ohno et al., 2021). These increases are primarily due to cellular damage, ion pump dysfunction, excitotoxicity, or blood-brain barrier disruption (David et al., 2009, Janigro, 2012, Keep et al., 1999, Lapilover et al., 2012, Larsen et al., 2016). If not properly regulated, disruptions in potassium homeostasis can further impair neuronal activity and exacerbate damage.

Alterations in astrocytic potassium regulation have been implicated in neurodegenerative diseases such as Huntington’s and Alzheimer’s disease, as well as ALS (Ding et al., 2024, Khakh et al., 2017, Ohno et al., 2021). Recently, studies have reported a reduced potassium clearance rate in the motor cortex of SOD1/C57Bl6 mice, correlating with motor neuron loss (Ding et al., 2024, Stevenson et al., 2023). However, our data revealed comparable swelling in both control and SOD1 cortical astrocytes, suggesting that potassium uptake remains intact in the cortex of SOD1/GFAP/EGFP mice despite significant astrogliosis. The uptake is however, only one of the intricate clearance mechanisms. Recently, Stevenson et al. (2023) proposed a possible interpretation of the divergence in our data. They explain the reduced clearance by reduced coupling of astrocytes, which prevents spatial buffering rather than by a changed K^+ uptake. The uptake is closely associated with the potassium channels and ion transporters. The pivotal channels responsible for K^+ removal are Kir4.1. They are expressed primarily in astrocytes and their altered expression has been previously reported in SOD1(G93A) rats and mice (Bataveljic et al., 2012, Kaiser et al., 2006) in the spinal cord but not in the cortex. This aligns with our results from immunohistochemistry, showing no difference in Kir4.1 expression in the cortical astrocytes and we associate this with the non-different swelling.

In contrast to the cortex, SOD1 spinal astrocytes exhibited significantly less swelling during exposure to elevated (50 mM) potassium concentrations, suggesting a dysfunction in the uptake mechanism. We hypothesized that this weaker response in SOD1 astrocytes may be related to alterations in potassium channels or ion co-transporters. The immunohistochemistry confirmed significantly decreased expression of the Kir4.1 channel, which could explain the diminished swelling. Nevertheless, it needs to be mentioned that the increased K^+ can affect activity of other transport mechanisms, for example glutamate transporters and since the rise in K^+ concentration causes depolarization of astrocyte membranes (Du et al., 2018) other voltage-dependent cellular processes are also likely to be affected. Therefore, we cannot rule out the possibility that reduced astrocyte swelling observed under high K^+ exposure is not only due to changes in Kir4.1 expression, but also reflects changes in the expression/function of glutamate transporters or ion co- transporters.

Both astrogliosis and the swelling we studied are closely related to the ECS diffusion parameters. To analyze those parameters, we used the RTI method and conducted measurements on brain and spinal cord slices during exposure to high (20 mM and 50 mM) K^+. Both potassium levels led to a noticeable reduction in ECS volume fraction, suggesting a shrinkage of the ECS due to cell swelling or swelling of their components. Our data showed that the lower potassium concentration (20 mM) did not produce significant differences in the typical time course of ECS parameter changes between CTRL and SOD1 mice, in either the brain or spinal cord. The higher potassium concentration (50 mM) did not trigger inter-group differences in the cortex either. However, in the spinal cord, 50 mM K^+ had a stronger effect and the exposure led to a significant reduction in ECS volume fraction in CTRLs compared to SOD1 mice, along with a significant rise in tortuosity in CTRL mice. It is worth noting that tortuosity values in the spinal cord can be influenced by the presence and density of myelinated fibers, which act as significant barriers to diffusion (Thorne et al., 2005), contributing to the higher initial tortuosity values in the spinal cord compared to the brain. The increased tortuosity seen in CTRL mice may be partly due to the tighter alignment of myelin fibers caused by cellular swelling and a greater reduction in extracellular space, compared to SOD1 mice. Earlier studies from our laboratory demonstrated that changes in ECS volume fraction and tortuosity are heavily influenced by dynamic alterations in the extracellular matrix (ECM) (Sucha et al., 2020, Zamecnik et al., 2012, Zamecnik et al., 2004). Several studies on SOD1 rats have confirmed alterations in ECM composition, reporting disorganized or damaged perineuronal nets around spinal motor neurons and varying expression profiles of chondroitin sulfate proteoglycans (CSPGs) (Cheung et al., 2024, Forostyak et al., 2020, Forostyak et al., 2014). We initially hypothesized that ECM changes in SOD1 tissue might influence the ECS diffusion parameters, but we did not find any differences in the baseline values of volume fraction and tortuosity between CTRL and SOD1 mice in either the brain or spinal cord.

A comparison between the RTI measurements and analyses of astrocytic swelling revealed similar responses to increased K^+ levels, with both techniques identifying astrocyte swelling and the accompanying compensatory shrinkage of ECS volume, followed by a similar recovery during the washout period. As noted in earlier studies, such consistency between RTI and 3D morphometry results is rare, given that RTI captures volume changes across all cell types, not just astrocytes (Kolenicova et al., 2020, Tureckova et al., 2021). These findings highlight the pivotal role that astrocytes play in hyperkalemia-induced cell swelling. Furthermore, they are in line with the study by Walch et al. (2020), who demonstrated that glial cells, particularly astrocytes, are highly susceptible to potassium-induced alterations, whereas neurons are relatively resistant to such changes.

In addition to K^+, other ions, such as Ca^{2+} (Alexianu et al., 1994), Na^+ (Kuo et al., 2004, Kuo et al., 2005, Pieri et al., 2009), and Mg^{2+}, are also dysregulated in ALS. We examined the CSF for K^+, Ca^{2+}, Na^+, Fe^{2+}, P and S and we only found a notable decrease in magnesium levels in SOD1 mice. Magnesium is crucial for muscle function, cellular antioxidant mechanisms, and neuronal signaling, particularly in preventing excitotoxicity by inhibiting NMDA receptors (Shindo et al., 2020). The decrease we revealed aligns with previous findings in postmortem samples from ALS patients (Yasui et al., 1997), suggesting that magnesium deficiency could be a potential risk factor for ALS. This translated into further research focusing on magnesium supplementation as a potential modifier of the disease progression. Nevertheless, at least in the SOD1 mouse model, (Pamphlett et al., 2003) no increased survival or delayed disease onset was reported after higher magnesium supplementation.

Interestingly, we did not identify elevated levels of K^+ during the analysis. Potassium levels were previously determined in ALS mice by (Ding et al., 2024) using *in vivo* recording with K^+- sensitive electrodes. They reported a significant rise in the level of K^+ in the cortex of SOD1 mice. A possible explanation of why we did not find any difference is the different methodological approach. As (Stevenson et al., 2023) recently showed, the rate of potassium clearance and concentration can differ even within parts of the cortex. Therefore, analysis of CSF would not detect any region-specific potassium level alterations.

5.3 Functional Properties of Astrocytes in the Model of Alzheimer´s Disease

We primarily focused on the astrocytes and their functional properties in ALS. However, ALS and AD share some pathways of neurodegeneration, although, manifested in different clinical symptoms. Astrocytic activation has been described in both pathologies and the activation is closely associated with functional changes including homeostasis maintenance. Vitvitsky et al. (2012) reported compromised ion homeostasis in the AD, which together with potentially compromised uptake and/or loss of astrocytic ability to regulate their volume could add to the progression. Furthermore, in the recent study of Kolenicova et al. (2020), it was demonstrated that the volume of single astrocytes changes under exposure to high K^+ concentration and that these changes alter with aging, a natural neurodegenerative process. We thus aimed to combine the model of pathology with physiological aging, as it is one of the biggest risk factors for the AD development.

We compared age-related changes with those caused by pathological processes typical of AD during hyperkalemia and observed that changes associated with aging occurred earlier in the 3xTg-AD mouse model. These mice exhibited lower volume changes than CTRLs, and these changes were consistent across different age groups. Conversely, volume changes induced by hypo-osmotic stress showed no aging-related differences in the previous study (Kolenicova et al., 2020), but 3xTg-AD astrocytes swelled significantly less than controls, similar to the response to hyperkalemia. These findings suggest that mechanisms for the uptake or extrusion of osmotically active substances, such as ions and neurotransmitters, as well as water transport, are impaired in 3xTg-AD mice. We hypothesized that these defects could stem from altered expression of channels and transporters previously linked to astrocyte swelling under hypo-osmotic stress or ischemic conditions. The data from single-cell RT-qPCR analysis of such genes in (Tureckova et al., 2021) showed that even in young, 3M 3xTg-AD mice, the expression of some homeostatic genes was significantly lower compared to controls. In 9M 3xTg-AD mice, the expression of these genes increased and remained stable until 18 months of age. We hypothesized that such late overexpression could be a compensatory mechanism in response to the deterioration of astrocyte homeostatic functions.

The measurements of ECS diffusion parameters revealed a gradual age-related decrease of volume fraction and increase in tortuosity in the hippocampus of aging mice (here used as CTRLs) in our data and in Kolenicova et al. (2020). Unlike physiological aging, we observed no age-related decline in volume fraction in 3xTg-AD mice. This result aligns with findings from another AD model, APP23 mice (Sykova et al., 2005), and could be linked to amyloid deposits in the ECS, which would prevent the reduction of ECS volume in aged tissue. Furthermore, other factors, such as astrocyte atrophy (Rodriguez-Arellano et al., 2016) or alterations in ECM composition (Morawski et al., 2012, Sethi and Zaia, 2017), should be considered as well, particularly during the earlier stages of aging.

The comparison of tortuosity revealed more hindered extracellular diffusion (higher λ values) in the 12M 3xTg-AD mice compared to age-matched controls. Notably, the increase in tortuosity typically seen with physiological aging was accelerated in the 3xTg-AD mice, with a significant "jump" occurring between 9 and 12 months of age, while a similar rise in tortuosity was observed between 12 and 18 months in the control group. We hypothesize that factors, such as morphological changes in glial cells and/or increased ECM expression, must contribute to the observed tortuosity increase. Indeed, some studies showed (Roitbak and Sykova, 1999, Vegh et al., 2014, Zamecnik et al., 2004) that during various pathological conditions, the increase in ECS volume and/or tortuosity are aligned with the ECM overexpression. Conversely, the decrease in those values is associated with decreased ECM content or lack of core ECM molecules (Bekku et al., 2010, Sykova et al., 2005). Furthermore, AD-related reactive astrogliosis, involving morphological changes in astrocytic processes, along with elevated expression of various ECM molecules, has been documented during the advanced stages of AD progression (Morawski et al., 2012, Rodriguez-Arellano et al., 2016, Vegh et al., 2014).

Similar to the situation in ALS, we observed a diminished swelling in response to hyperkalemia in 3xTg-AD mice, specifically at 3M and 12M time points, and to hypo-osmotic stress at 9M and 12M. However, we did not detect corresponding changes in the ESC parameters. This variability between the ECS volume changes and astrocytic swelling was already observed in other studies from our laboratory (Anderova et al., 2014, Dmytrenko et al., 2013, Kolenicova et al., 2020) and is likely caused by the methodical approach, as the RTI measurements reflect volume changes of all cell types, not just astrocytes. Another cell type with a large swelling capacity is comprised by neurons and as Genocchi et al. (2020) showed, the proportion between neuronal and astrocytic swelling can be changed due to different expression of channels and transporters. Based on results from gene profiling in (Tureckova et al., 2021), we could assume that the swelling proportion between astrocytes and neurons or other cell types differs between 3xTg-AD mice and CTRLs and contributes to the inconsistency between the RTI method and 3D-morphometry.

We also analyzed the recovery of the ECS values during the washout and observed that it was generally only partial in the older groups. This contrasts with the astrocytic volume measurements, where we saw a full recovery or even undershoot in all tested groups after hypo-osmotic stress or hyperkalemia. Again, this discrepancy is likely due to the involvement of other cell types contributing to the changes of the volume fraction. Additionally, no recovery was observed during physiological aging in the 18M animals. The lack of recovery may indicate irreversible tissue damage caused by severe depolarization from the 50 mM K^+, potentially more pronounced in older animals with already reduced basal ECS volume (Vorisek and Sykova, 1997). In a smaller space, the concentration of glutamate or other toxic substances in the interstitial fluid can become extremely high, leading to irreversible cytotoxic damage to the tissue.

6 CONCLUSIONS

In the presented work, we focused on the role and involvement of glial cells in ALS mouse models and then further inspected the astrocytes also in the model of AD as they share some pathological features. We used multiple animal models and several methods looking at the mRNA, protein and functional level to get a complex outlook on the topic.

First, we investigated the cortical glia in the animal model that is used to study ALS the most – the SOD1(G93A) mouse. We confirmed the model´s phenotype using behavioral testing, including identification of differences between males and females. Furthermore, we focused on the changes on the molecular level. The transcriptomic analysis revealed that cortical astrocytes are not affected by the pathology, microglia display features of starting activation and oligodendrocytes seemed to be affected the most as we identified a SOD1-specific oligodendroglial population. The immunohistochemistry then confirmed our assumptions that the overall impact of ALS-like pathology on the cortex is minimal in this model, and it does not reliably mimic the patients´ pathology; however, the presence of the SOD1-specific oligodendrocytes adds to the growing evidence of their active involvement in neurodegeneration.

Even though astrocytes did not exhibit any ALS-related changes in the cortex of the SOD1(G93A) mouse model, they are an important element in the disease due to their homeostatic functions, which we aimed to investigate further. Results of our experiments using the SOD1(G93A) animal model on FVB/N background revealed astrocytic activation in both the cortex and spinal cord and overall worse gross phenotype of the mice, which was most likely caused by the different genetic background. The functional measurements of swelling showed diminished K^+ uptake of spinal astrocytes during hyperkalemia, which was confirmed also by the RTI method showing an increase in ECS volume fraction. Based on the results from immunohistochemical analysis of Kir4.1 expression, we assume the inefficient uptake could be associated with a lower expression of this channel as it was downregulated in the spinal cord only.

The analysis of astrocytic functional properties and the ECS in AD revealed an increase in the diffusion barriers that occurred earlier in AD mice compared to the age-matched controls. These changes are most likely associated with the structural shifts caused by the pathology. However, we proved that they do not affect the ECS shrinkage during application of hyperkalemia or hypo-osmotic stress. On the other hand, they seem to affect the astrocytic ability of K^+ uptake as we have observed a diminished swelling during hyperkalemia in 3M and 12M animals.

Altogether, glial cells are an important component in ALS as they are essential for proper CNS functioning. When affected by pathology, they acquire activated morphology accompanied by alterations in their transcriptional profile as well as protein expression. These lead to changes in glial functions, which can in turn further influence the CNS environment and contribute to neurodegeneration. Our results provided new insights especially into the homeostatic abilities of astrocytes in ALS as well as in AD, but also highlighted the importance of working with a reliable disease model in order to further understand the pathology and advance in efforts to find a suitable therapeutic approach.

7 SUMMARY

7.1 Characterization of the SOD1(G93A) Mouse Model Phenotype and Pathological Traita in the Motor Cortex

We studied the ALS-pathology in the cortex of SOD1(G93A) animals throughout the disease progression and looked for pathological changes in glial cells using scRNA-seq and immunohistochemistry. Our analyses revealed no alterations in astrocytes and only minor changes in microglia and oligodendrocytes at the final stage. The results indicate early stages of activation, but the degree of these changes does not align with those observed in human tissue, supporting the argument against using this model to study ALS pathology in the cortex.

7.2 Functional Properties of Astrocytes in a Mouse Model of Amyotrophic lateral sclerosis

To continue revealing the role of glial cells in the ALS, we focused on astrocytes and their ability to maintain ion homeostasis. We confirmed variability between animal models caused by a different genetic background and observed astrocytic activation in the cortex as well as in the spinal cord. Our functional measurements revealed a spinal cord-specific impairment of astrocytic K^+ uptake during hyperkalemia, manifested also as changes of ECS values. Based on immunohistochemistry, this impairment is likely associated with a reduction of Kir4.1 expression.

7.3 Functional Properties of Astrocytes in a Model of Alzheimer´s Disease

To extend the knowledge about astrocytic functioning during pathology, we examined their swelling/volume regulation ability together with ECS values assessment also in the model of AD. Our results revealed an increase in diffusion barriers in AD mice, which further influenced astrocytic uptake of ions manifested as reduced swelling in response to hypo-osmotic stress or hyperkalemia. Overall, our data suggest that from the standpoint of astrocytic uptake and water regulation, AD can be understood as an accelerated form of physiological aging.

8 SOUHRN

8.1 Charakterizace fenotypu a patologie v mozkové kůře myšího modelu SOD1(G93A)

V této práci jsme studovali ALS patologii v mozkové kůře SOD1(G93A) myší v průběhu progrese onemocnění a soustředili jsme se na patologické změny gliových buněk s využitím sekvenování na úrovni jedné buňky a imunohistochemie. Naše experimenty neodhalily žádné změny v případě astrocytů a pouze mírné změny u mikroglií a oligodendrocytů ve finálním stádiu onemocnění. Tyto výsledky sice naznačují počínající aktivaci, ale nejsou v souladu se závažností změn, která byla v tomto stádiu pozorována u pacientů, což podporuje spekulace, že by tento model neměl být využíván pro studium ALS patologie v mozkové kůře.

8.2 Funkční vlastnosti astrocytů v myším modelu Amyotrofické laterální sklerózy

V rámci dalšího zkoumání role glií v ALS, jsme se zaměřili na astrocyty a homeostatické vlastnosti při udržování homeostázy iontů. Potvrdili jsme variabilitu mezi myšími modely způsobenou rozdílným genetickým pozadím a pozorovali jsme aktivaci astrocytů jak v mozkové kůře, tak v míše. Naše funkční měření odhalila nedostatečné vychytávání K^+ iontů během hyperkalémie u míšních astrocytů, což se projevilo také změnami v extracelulárním prostoru. K tomuto nedostatečnému vychytávání dochází pravděpodobně v důsledku snížené exprese kanálu Kir4.1, která byla zjištěna pomocí imunohistochemické analýzy.

8.3 Funkční vlastnosti astrocytů v myším modelu Alzheimerovy choroby

Abychom rozšířili znalosti o fungování astrocytů během patologií, zkoumali jsme jejich schopnost regulovat objem společně se změnami extracelulárního prostředí také v modelu AD. Naše výsledky ukázaly zvýšené množství difúzních bariér u myší s AD, což ovlivnilo schopnost astrocytů vychytávat ionty a projevilo se sníženým ‚swellingem' a to jak v prostředí hyperkalémie, tak během hypoosmotického stresu. Celkově naše data naznačují, že z pohledu objemové regulace astrocytů lze patologické procesy spojené s AD chápat jako zrychlenou formu fyziologického stárnutí.

9 REFERENCES

1. ABRAMOV, A. Y., CANEVARI, L. & DUCHEN, M. R. 2003. Changes in intracellular calcium and glutathione in astrocytes as the primary mechanism of amyloid neurotoxicity. *J Neurosci,* 23**,** 5088-95.
2. ABRAMOV, A. Y., CANEVARI, L. & DUCHEN, M. R. 2004. Beta-amyloid peptides induce mitochondrial dysfunction and oxidative stress in astrocytes and death of neurons through activation of NADPH oxidase. *J Neurosci,* 24**,** 565-75.
3. AFSAR, A., CHACON CASTRO, M. D. C., SOLADOGUN, A. S. & ZHANG, L. 2023. Recent Development in the Understanding of Molecular and Cellular Mechanisms Underlying the Etiopathogenesis of Alzheimer's Disease. *Int J Mol Sci,* 24.
4. ALEXIANU, M. E., HO, B. K., MOHAMED, A. H., LA BELLA, V., SMITH, R. G. & APPEL, S. H. 1994. The role of calcium-binding proteins in selective motoneuron vulnerability in amyotrophic lateral sclerosis. *Ann Neurol,* 36**,** 846-58.
5. ALTMANN, A., NG, B., LANDAU, S. M., JAGUST, W. J., GREICIUS, M. D. & ALZHEIMER'S DISEASE NEUROIMAGING, I. 2015. Regional brain hypometabolism is unrelated to regional amyloid plaque burden. *Brain,* 138**,** 3734-46.
6. ANDEROVA, M., BENESOVA, J., MIKESOVA, M., DZAMBA, D., HONSA, P., KRISKA, J., BUTENKO, O., NOVOSADOVA, V., VALIHRACH, L., KUBISTA, M., DMYTRENKO, L., CICANIC, M. & VARGOVA, L. 2014. Altered astrocytic swelling in the cortex of alpha-syntrophin-negative GFAP/EGFP mice. *PLoS One,* 9**,** e113444.
7. ASHBURNER, M., BALL, C. A., BLAKE, J. A., BOTSTEIN, D., BUTLER, H., CHERRY, J. M., DAVIS, A. P., DOLINSKI, K., DWIGHT, S. S., EPPIG, J. T., HARRIS, M. A., HILL, D. P., ISSEL-TARVER, L., KASARSKIS, A., LEWIS, S., MATESE, J. C., RICHARDSON, J. E., RINGWALD, M., RUBIN, G. M. & SHERLOCK, G. 2000. Gene ontology: tool for the unification of biology. The Gene Ontology Consortium. *Nat Genet,* 25**,** 25-9.
8. AUGUSTO-OLIVEIRA, M., ARRIFANO, G. P., LOPES-ARAÚJO, A., SANTOS-SACRAMENTO, L., TAKEDA, P. Y., ANTHONY, D. C., MALVA, J. O. & CRESPO-LOPEZ, M. E. 2019. What Do Microglia Really Do in Healthy Adult Brain? doi:10.3390/cells8101293. *Cells 2073-4409,* 8**,** 1293.
9. AWADOVA, T., PIVONKOVA, H., HERMANOVA, Z., KIRDAJOVA, D., ANDEROVA, M. & MALINSKY, J. 2018. Cell volume changes as revealed by fluorescence microscopy: Global vs local approaches. *J Neurosci Methods,* 306**,** 38-44.
10. AZEVEDO, F. A., CARVALHO, L. R., GRINBERG, L. T., FARFEL, J. M., FERRETTI, R. E., LEITE, R. E., JACOB FILHO, W., LENT, R. & HERCULANO-HOUZEL, S. 2009. Equal numbers of neuronal and nonneuronal cells make the human brain an isometrically scaled-up primate brain. *J Comp Neurol,* 513**,** 532-41.
11. BAKER, D. J., BLACKBURN, D. J., KEATINGE, M., SOKHI, D., VISKAITIS, P., HEATH, P. R., FERRAIUOLO, L., KIRBY, J. & SHAW, P. J. 2015. Lysosomal and phagocytic activity is increased in astrocytes during disease progression in the SOD1 (G93A) mouse model of amyotrophic lateral sclerosis. *Front Cell Neurosci,* 9**,** 410.
12. BATAVELJIC, D., NIKOLIC, L., MILOSEVIC, M., TODOROVIC, N. & ANDJUS, P. R. 2012. Changes in the astrocytic aquaporin-4 and inwardly rectifying potassium channel expression in the brain of the amyotrophic lateral sclerosis SOD1(G93A) rat model. *Glia,* 60**,** 1991-2003.

13. BATEMAN, R. J., XIONG, C., BENZINGER, T. L., FAGAN, A. M., GOATE, A., FOX, N. C., MARCUS, D. S., CAIRNS, N. J., XIE, X., BLAZEY, T. M., HOLTZMAN, D. M., SANTACRUZ, A., BUCKLES, V., OLIVER, A., MOULDER, K., AISEN, P. S., GHETTI, B., KLUNK, W. E., MCDADE, E., MARTINS, R. N., MASTERS, C. L., MAYEUX, R., RINGMAN, J. M., ROSSOR, M. N., SCHOFIELD, P. R., SPERLING, R. A., SALLOWAY, S., MORRIS, J. C. & DOMINANTLY INHERITED ALZHEIMER, N. 2012. Clinical and biomarker changes in dominantly inherited Alzheimer's disease. *N Engl J Med,* 367**,** 795-804.
14. BATIUK, M. Y., MARTIROSYAN, A., WAHIS, J., DE VIN, F., MARNEFFE, C., KUSSEROW, C., KOEPPEN, J., VIANA, J. F., OLIVEIRA, J. F., VOET, T., PONTING, C. P., BELGARD, T. G. & HOLT, M. G. 2020. Identification of region-specific astrocyte subtypes at single cell resolution. *Nat Commun,* 11**,** 1220.
15. BATTAGLIA, G., RIOZZI, B., BUCCI, D., DI MENNA, L., MOLINARO, G., PALLOTTINO, S., NICOLETTI, F. & BRUNO, V. 2015. Activation of mGlu3 metabotropic glutamate receptors enhances GDNF and GLT-1 formation in the spinal cord and rescues motor neurons in the SOD-1 mouse model of amyotrophic lateral sclerosis. *Neurobiol Dis,* 74**,** 126-36.
16. BAYRAKTAR, O. A., BARTELS, T., HOLMQVIST, S., KLESHCHEVNIKOV, V., MARTIROSYAN, A., POLIOUDAKIS, D., BEN HAIM, L., YOUNG, A. M. H., BATIUK, M. Y., PRAKASH, K., BROWN, A., ROBERTS, K., PAREDES, M. F., KAWAGUCHI, R., STOCKLEY, J. H., SABEUR, K., CHANG, S. M., HUANG, E., HUTCHINSON, P., ULLIAN, E. M., HEMBERG, M., COPPOLA, G., HOLT, M. G., GESCHWIND, D. H. & ROWITCH, D. H. 2020. Astrocyte layers in the mammalian cerebral cortex revealed by a single-cell in situ transcriptomic map. *Nat Neurosci,* 23**,** 500-509.
17. BEERS, D. R., ZHAO, W., LIAO, B., KANO, O., WANG, J., HUANG, A., APPEL, S. H. & HENKEL, J. S. 2011. Neuroinflammation modulates distinct regional and temporal clinical responses in ALS mice. *Brain Behav Immun,* 25**,** 1025-35.
18. BEKKU, Y., VARGOVA, L., GOTO, Y., VORISEK, I., DMYTRENKO, L., NARASAKI, M., OHTSUKA, A., FASSLER, R., NINOMIYA, Y., SYKOVA, E. & OOHASHI, T. 2010. Bral1: its role in diffusion barrier formation and conduction velocity in the CNS. *J Neurosci,* 30**,** 3113-23.
19. BEN HAIM, L., CEYZERIAT, K., CARRILLO-DE SAUVAGE, M. A., AUBRY, F., AUREGAN, G., GUILLERMIER, M., RUIZ, M., PETIT, F., HOUITTE, D., FAIVRE, E., VANDESQUILLE, M., ARON-BADIN, R., DHENAIN, M., DEGLON, N., HANTRAYE, P., BROUILLET, E., BONVENTO, G. & ESCARTIN, C. 2015. The JAK/STAT3 pathway is a common inducer of astrocyte reactivity in Alzheimer's and Huntington's diseases. *J Neurosci,* 35**,** 2817-29.
20. BENARROCH, E. E. 2013. Microglia: Multiple roles in surveillance, circuit shaping, and response to injury. *Neurology,* 81**,** 1079-88.
21. BENDOTTI, C., TORTAROLO, M., SUCHAK, S. K., CALVARESI, N., CARVELLI, L., BASTONE, A., RIZZI, M., RATTRAY, M. & MENNINI, T. 2001. Transgenic SOD1 G93A mice develop reduced GLT-1 in spinal cord without alterations in cerebrospinal fluid glutamate levels. *Journal of Neurochemistry,* 79**,** 737-746.
22. BENESOVA, J., HOCK, M., BUTENKO, O., PRAJEROVA, I., ANDEROVA, M. & CHVATAL, A. 2009. Quantification of astrocyte volume changes during ischemia in situ reveals two populations of astrocytes in the cortex of GFAP/EGFP mice. *J Neurosci Res,* 87**,** 96-111.
23. BOILLÉE, S., YAMANAKA, K., LOBSIGER, C. S., COPELAND, N. G., JENKINS, N. A., KASSIOTIS, G., KOLLIAS, G. & CLEVELAND, D. W. 2006.

Onset and Progression in Inherited ALS Determined by Motor Neurons and Microglia. *Science,* 312**,** 1389-1392.

24. BONFANTI, E., BONIFACINO, T., RAFFAELE, S., MILANESE, M., MORGANTE, E., BONANNO, G., ABBRACCHIO, M. P. & FUMAGALLI, M. 2020. Abnormal Upregulation of GPR17 Receptor Contributes to Oligodendrocyte Dysfunction in SOD1 G93A Mice. *Int J Mol Sci,* 21.
25. BRADL, M. & LASSMANN, H. 2010. Oligodendrocytes: biology and pathology. *Acta Neuropathol,* 119**,** 37-53.
26. BRUIJN, L. I., BECHER, M. W., LEE, M. K., ANDERSON, K. L., JENKINS, N. A., COPELAND, N. G., SISODIA, S. S., ROTHSTEIN, J. D., BORCHELT, D. R., PRICE, D. L. & CLEVELAND, D. W. 1997. ALS-Linked SOD1 Mutant G85R Mediates Damage to Astrocytes and Promotes Rapidly Progressive Disease with SOD1-Containing Inclusions. *Neuron,* 18**,** 327-338.
27. BURG, T., BICHARA, C., SCEKIC-ZAHIROVIC, J., FISCHER, M., STUART-LOPEZ, G., BRUNET, A., LEFEBVRE, F., CORDERO-ERAUSQUIN, M. & ROUAUX, C. 2020. Absence of Subcerebral Projection Neurons Is Beneficial in a Mouse Model of Amyotrophic Lateral Sclerosis. *Ann Neurol,* 88**,** 688-702.
28. BUTOVSKY, O. & WEINER, H. L. 2018. Microglial signatures and their role in health and disease. *Nat Rev Neurosci,* 19**,** 622-635.
29. BUTT, A. M., PAPANIKOLAOU, M. & RIVERA, A. 2019. Physiology of Oligodendroglia. *Adv Exp Med Biol,* 1175**,** 117-128.
30. CABRAL-COSTA, J. V. & KOWALTOWSKI, A. J. 2023. Mitochondrial Ca2+ handling as a cell signaling hub: lessons from astrocyte function. *Essays Biochem,* 67**,** 63-75.
31. CHEUNG, S. W., BHAVNANI, E., SIMMONS, D. G., BELLINGHAM, M. C. & NOAKES, P. G. 2024. Perineuronal nets are phagocytosed by MMP-9 expressing microglia and astrocytes in the SOD1(G93A) ALS mouse model. *Neuropathol Appl Neurobiol,* 50**,** e12982.
32. CHIU, I. M., MORIMOTO, E. T., GOODARZI, H., LIAO, J. T., O'KEEFFE, S., PHATNANI, H. P., MURATET, M., CARROLL, M. C., LEVY, S., TAVAZOIE, S., MYERS, R. M. & MANIATIS, T. 2013. A neurodegeneration-specific gene-expression signature of acutely isolated microglia from an amyotrophic lateral sclerosis mouse model. *Cell Rep,* 4**,** 385-401.
33. CHVATAL, A., ANDEROVA, M., HOCK, M., PRAJEROVA, I., NEPRASOVA, H., CHVATAL, V., KIRCHHOFF, F. & SYKOVA, E. 2007a. Three-dimensional confocal morphometry reveals structural changes in astrocyte morphology in situ. *J Neurosci Res,* 85**,** 260-71.
34. CHVATAL, A., ANDEROVA, M. & KIRCHHOFF, F. 2007b. Three-dimensional confocal morphometry - a new approach for studying dynamic changes in cell morphology in brain slices. *J Anat,* 210**,** 671-83.
35. CLEMENT, A. M., NGUYEN, M. D., ROBERTS, E. A., GARCIA, M. L., BOILLEE, S., RULE, M., MCMAHON, A. P., DOUCETTE, W., SIWEK, D., FERRANTE, R. J., BROWN, R. H., JR., JULIEN, J. P., GOLDSTEIN, L. S. & CLEVELAND, D. W. 2003. Wild-type nonneuronal cells extend survival of SOD1 mutant motor neurons in ALS mice. *Science,* 302**,** 113-7.
36. COLONNA, M. & BUTOVSKY, O. 2017. Microglia Function in the Central Nervous System During Health and Neurodegeneration. *Annu Rev Immunol,* 35**,** 441-468.
37. COLONNA, M. & WANG, Y. 2016. TREM2 variants: new keys to decipher Alzheimer disease pathogenesis. *Nat Rev Neurosci,* 17**,** 201-7.

38. CONNOR, J. R. & MENZIES, S. L. 1996. Relationship of iron to oligodendrocytes and myelination. *Glia,* 17**,** 83-93.
39. COOK, C., CARLOMAGNO, Y., GENDRON, T. F., DUNMORE, J., SCHEFFEL, K., STETLER, C., DAVIS, M., DICKSON, D., JARPE, M., DETURE, M. & PETRUCELLI, L. 2014. Acetylation of the KXGS motifs in tau is a critical determinant in modulation of tau aggregation and clearance. *Hum Mol Genet,* 23**,** 104-16.
40. CUI, Q. L., KUHLMANN, T., MIRON, V. E., LEONG, S. Y., FANG, J., GRIS, P., KENNEDY, T. E., ALMAZAN, G. & ANTEL, J. 2013. Oligodendrocyte progenitor cell susceptibility to injury in multiple sclerosis. *Am J Pathol,* 183**,** 516-25.
41. DANBOLT, N. C. 2001. Glutamate uptake. *Prog Neurobiol,* 65**,** 1-105.
42. DAVALOS, D., GRUTZENDLER, J., YANG, G., KIM, J. V., ZUO, Y., JUNG, S., LITTMAN, D. R., DUSTIN, M. L. & GAN, W. B. 2005. ATP mediates rapid microglial response to local brain injury in vivo. *Nat Neurosci,* 8**,** 752-8.
43. DAVID, Y., CACHEAUX, L. P., IVENS, S., LAPILOVER, E., HEINEMANN, U., KAUFER, D. & FRIEDMAN, A. 2009. Astrocytic dysfunction in epileptogenesis: consequence of altered potassium and glutamate homeostasis? *J Neurosci,* 29**,** 10588-99.
44. DE STROOPER, B. & KARRAN, E. 2016. The Cellular Phase of Alzheimer's Disease. *Cell,* 164**,** 603-15.
45. DEJESUS-HERNANDEZ, M., MACKENZIE, I. R., BOEVE, B. F., BOXER, A. L., BAKER, M., RUTHERFORD, N. J., NICHOLSON, A. M., FINCH, N. A., FLYNN, H., ADAMSON, J., KOURI, N., WOJTAS, A., SENGDY, P., HSIUNG, G. Y., KARYDAS, A., SEELEY, W. W., JOSEPHS, K. A., COPPOLA, G., GESCHWIND, D. H., WSZOLEK, Z. K., FELDMAN, H., KNOPMAN, D. S., PETERSEN, R. C., MILLER, B. L., DICKSON, D. W., BOYLAN, K. B., GRAFF-RADFORD, N. R. & RADEMAKERS, R. 2011. Expanded GGGGCC hexanucleotide repeat in noncoding region of C9ORF72 causes chromosome 9p-linked FTD and ALS. *Neuron,* 72**,** 245-56.
46. DENG, Y., XIE, D., FANG, M., ZHU, G., CHEN, C., ZENG, H., LU, J. & CHARANJIT, K. 2014. Astrocyte-derived proinflammatory cytokines induce hypomyelination in the periventricular white matter in the hypoxic neonatal brain. *PLoS One,* 9**,** e87420.
47. DING, F., SUN, Q., LONG, C., RASMUSSEN, R. N., PENG, S., XU, Q., KANG, N., SONG, W., WEIKOP, P., GOLDMAN, S. A. & NEDERGAARD, M. 2024. Dysregulation of extracellular potassium distinguishes healthy ageing from neurodegeneration. *Brain,* 147**,** 1726-1739.
48. DIXIT, R., ROSS, J. L., GOLDMAN, Y. E. & HOLZBAUR, E. L. 2008. Differential regulation of dynein and kinesin motor proteins by tau. *Science,* 319**,** 1086-9.
49. DMYTRENKO, L., CICANIC, M., ANDEROVA, M., VORISEK, I., OTTERSEN, O. P., SYKOVA, E. & VARGOVA, L. 2013. The impact of alpha-syntrophin deletion on the changes in tissue structure and extracellular diffusion associated with cell swelling under physiological and pathological conditions. *PLoS One,* 8**,** e68044.
50. DOBIN, A., DAVIS, C. A., SCHLESINGER, F., DRENKOW, J., ZALESKI, C., JHA, S., BATUT, P., CHAISSON, M. & GINGERAS, T. R. 2013. STAR: ultrafast universal RNA-seq aligner. *Bioinformatics,* 29**,** 15-21.
51. DOLS-ICARDO, O., MONTAL, V., SIRISI, S., LOPEZ-PERNAS, G., CERVERA-CARLES, L., QUEROL-VILASECA, M., MUNOZ, L., BELBIN, O., ALCOLEA, D., MOLINA-PORCEL, L., PEGUEROLES, J., TURON-SANS, J., BLESA, R., LLEO, A., FORTEA, J., ROJAS-GARCIA, R. & CLARIMON, J. 2020. Motor

cortex transcriptome reveals microglial key events in amyotrophic lateral sclerosis. *Neurol Neuroimmunol Neuroinflamm,* 7.

52. DORETTO, S., MALERBA, M., RAMOS, M., IKRAR, T., KINOSHITA, C., DE MEI, C., TIROTTA, E., XU, X. & BORRELLI, E. 2011. Oligodendrocytes as regulators of neuronal networks during early postnatal development. *PLoS One,* 6**,** e19849.
53. DU, Y., WANG, W., LUTTON, A. D., KIYOSHI, C. M., MA, B., TAYLOR, A. T., OLESIK, J. W., MCTIGUE, D. M., ASKWITH, C. C. & ZHOU, M. 2018. Dissipation of transmembrane potassium gradient is the main cause of cerebral ischemia-induced depolarization in astrocytes and neurons. *Exp Neurol,* 303**,** 1-11.
54. DUYCKAERTS, C., DELATOUR, B. & POTIER, M. C. 2009. Classification and basic pathology of Alzheimer disease. *Acta Neuropathol,* 118**,** 5-36.
55. ESCARTIN, C., GALEA, E., LAKATOS, A., O'CALLAGHAN, J. P., PETZOLD, G. C., SERRANO-POZO, A., STEINHAUSER, C., VOLTERRA, A., CARMIGNOTO, G., AGARWAL, A., ALLEN, N. J., ARAQUE, A., BARBEITO, L., BARZILAI, A., BERGLES, D. E., BONVENTO, G., BUTT, A. M., CHEN, W. T., COHEN-SALMON, M., CUNNINGHAM, C., DENEEN, B., DE STROOPER, B., DIAZ-CASTRO, B., FARINA, C., FREEMAN, M., GALLO, V., GOLDMAN, J. E., GOLDMAN, S. A., GOTZ, M., GUTIERREZ, A., HAYDON, P. G., HEILAND, D. H., HOL, E. M., HOLT, M. G., IINO, M., KASTANENKA, K. V., KETTENMANN, H., KHAKH, B. S., KOIZUMI, S., LEE, C. J., LIDDELOW, S. A., MACVICAR, B. A., MAGISTRETTI, P., MESSING, A., MISHRA, A., MOLOFSKY, A. V., MURAI, K. K., NORRIS, C. M., OKADA, S., OLIET, S. H. R., OLIVEIRA, J. F., PANATIER, A., PARPURA, V., PEKNA, M., PEKNY, M., PELLERIN, L., PEREA, G., PEREZ-NIEVAS, B. G., PFRIEGER, F. W., POSKANZER, K. E., QUINTANA, F. J., RANSOHOFF, R. M., RIQUELME-PEREZ, M., ROBEL, S., ROSE, C. R., ROTHSTEIN, J. D., ROUACH, N., ROWITCH, D. H., SEMYANOV, A., SIRKO, S., SONTHEIMER, H., SWANSON, R. A., VITORICA, J., WANNER, I. B., WOOD, L. B., WU, J., ZHENG, B., ZIMMER, E. R., ZOREC, R., SOFRONIEW, M. V. & VERKHRATSKY, A. 2021. Reactive astrocyte nomenclature, definitions, and future directions. *Nat Neurosci,* 24**,** 312-325.
56. FALCAO, A. M., VAN BRUGGEN, D., MARQUES, S., MEIJER, M., JAKEL, S., AGIRRE, E., SAMUDYATA, FLORIDDIA, E. M., VANICHKINA, D. P., FFRENCH-CONSTANT, C., WILLIAMS, A., GUERREIRO-CACAIS, A. O. & CASTELO-BRANCO, G. 2018. Disease-specific oligodendrocyte lineage cells arise in multiple sclerosis. *Nat Med,* 24**,** 1837-1844.
57. FAULKNER, J. R., HERRMANN, J. E., WOO, M. J., TANSEY, K. E., DOAN, N. B. & SOFRONIEW, M. V. 2004. Reactive astrocytes protect tissue and preserve function after spinal cord injury. *J Neurosci,* 24**,** 2143-55.
58. FELSKY, D., ROOSTAEI, T., NHO, K., RISACHER, S. L., BRADSHAW, E. M., PETYUK, V., SCHNEIDER, J. A., SAYKIN, A., BENNETT, D. A. & DE JAGER, P. L. 2019. Neuropathological correlates and genetic architecture of microglial activation in elderly human brain. *Nat Commun,* 10**,** 409.
59. FERRAIUOLO, L., HIGGINBOTTOM, A., HEATH, P. R., BARBER, S., GREENALD, D., KIRBY, J. & SHAW, P. J. 2011. Dysregulation of astrocyte-motoneuron cross-talk in mutant superoxide dismutase 1-related amyotrophic lateral sclerosis. *Brain,* 134**,** 2627-41.
60. FERREIRA, T. A., BLACKMAN, A. V., OYRER, J., JAYABAL, S., CHUNG, A. J., WATT, A. J., SJOSTROM, P. J. & VAN MEYEL, D. J. 2014. Neuronal morphometry directly from bitmap images. *Nat Methods,* 11**,** 982-4.

61. FILIPI, T., HERMANOVA, Z., TURECKOVA, J., VANATKO, O. & ANDEROVA, A. M. 2020. Glial Cells-The Strategic Targets in Amyotrophic Lateral Sclerosis Treatment. *J Clin Med,* 9.
62. FILIPI, T., MATUSOVA, Z., ABAFFY, P., VANATKO, O., TURECKOVA, J., BENESOVA, S., KUBISKOVA, M., KIRDAJOVA, D., ZAHUMENSKY, J., VALIHRACH, L. & ANDEROVA, M. 2023. Cortical glia in SOD1(G93A) mice are subtly affected by ALS-like pathology. *Sci Rep,* 13**,** 6538.
63. FLORIDDIA, E. M., LOURENCO, T., ZHANG, S., VAN BRUGGEN, D., HILSCHER, M. M., KUKANJA, P., GONCALVES DOS SANTOS, J. P., ALTINKOK, M., YOKOTA, C., LLORENS-BOBADILLA, E., MULINYAWE, S. B., GRAOS, M., SUN, L. O., FRISEN, J., NILSSON, M. & CASTELO-BRANCO, G. 2020. Distinct oligodendrocyte populations have spatial preference and different responses to spinal cord injury. *Nat Commun,* 11**,** 5860.
64. FORBES, T. A. & GALLO, V. 2017. All Wrapped Up: Environmental Effects on Myelination. *Trends Neurosci,* 40**,** 572-587.
65. FOROSTYAK, S., FOROSTYAK, O., KWOK, J. C. F., ROMANYUK, N., REHOROVA, M., KRISKA, J., DAYANITHI, G., RAHA-CHOWDHURY, R., JENDELOVA, P., ANDEROVA, M., FAWCETT, J. W. & SYKOVA, E. 2020. Transplantation of Neural Precursors Derived from Induced Pluripotent Cells Preserve Perineuronal Nets and Stimulate Neural Plasticity in ALS Rats. *Int J Mol Sci,* 21.
66. FOROSTYAK, S., HOMOLA, A., TURNOVCOVA, K., SVITIL, P., JENDELOVA, P. & SYKOVA, E. 2014. Intrathecal delivery of mesenchymal stromal cells protects the structure of altered perineuronal nets in SOD1 rats and amends the course of ALS. *Stem Cells,* 32**,** 3163-72.
67. FRAKES, A. E., FERRAIUOLO, L., HAIDET-PHILLIPS, A. M., SCHMELZER, L., BRAUN, L., MIRANDA, C. J., LADNER, K. J., BEVAN, A. K., FOUST, K. D., GODBOUT, J. P., POPOVICH, P. G., GUTTRIDGE, D. C. & KASPAR, B. K. 2014. Microglia induce motor neuron death via the classical NF-kappaB pathway in amyotrophic lateral sclerosis. *Neuron,* 81**,** 1009-1023.
68. FÜNFSCHILLING, U., SUPPLIE, L. M., MAHAD, D., BORETIUS, S., SAAB, A. S., EDGAR, J., BRINKMANN, B. G., KASSMANN, C. M., TZVETANOVA, I. D., MÖBIUS, W., DIAZ, F., MEIJER, D., SUTER, U., HAMPRECHT, B., SEREDA, M. W., MORAES, C. T., FRAHM, J., GOEBBELS, S. & NAVE, K.-A. 2012. Glycolytic oligodendrocytes maintain myelin and long-term axonal integrity. *Nature,* 485**,** 517-521.
69. GAO, C., JIANG, J., TAN, Y. & CHEN, S. 2023. Microglia in neurodegenerative diseases: mechanism and potential therapeutic targets. *Signal Transduct Target Ther,* 8**,** 359.
70. GENOCCHI, B., CUNHA, A., JAIN, S., HYTTINEN, J., LENK, K. & ELLINGSRUD, A. J. 2020. Parametric exploration of cellular swelling in a computational model of cortical spreading depression. *Annu Int Conf IEEE Eng Med Biol Soc,* 2020**,** 2491-2495.
71. GERBER, Y. N., SABOURIN, J. C., RABANO, M., VIVANCO, M. & PERRIN, F. E. 2012. Early functional deficit and microglial disturbances in a mouse model of amyotrophic lateral sclerosis. *PLoS One,* 7**,** e36000.
72. GIANNAKOPOULOS, P., HERRMANN, F. R., BUSSIERE, T., BOURAS, C., KOVARI, E., PERL, D. P., MORRISON, J. H., GOLD, G. & HOF, P. R. 2003. Tangle and neuron numbers, but not amyloid load, predict cognitive status in Alzheimer's disease. *Neurology,* 60**,** 1495-500.

73. GINHOUX, F., GRETER, M., LEBOEUF, M., NANDI, S., SEE, P., GOKHAN, S., MEHLER, M. F., CONWAY, S. J., NG, L. G., STANLEY, E. R., SAMOKHVALOV, I. M. & MERAD, M. 2010. Fate mapping analysis reveals that adult microglia derive from primitive macrophages. *Science,* 330**,** 841-5.
74. GOMES, C., CUNHA, C., NASCIMENTO, F., RIBEIRO, J. A., VAZ, A. R. & BRITES, D. 2019. Cortical Neurotoxic Astrocytes with Early ALS Pathology and miR-146a Deficit Replicate Gliosis Markers of Symptomatic SOD1G93A Mouse Model. *Mol Neurobiol,* 56**,** 2137-2158.
75. GOMES, C., SEQUEIRA, C., BARBOSA, M., CUNHA, C., VAZ, A. R. & BRITES, D. 2020. Astrocyte regional diversity in ALS includes distinct aberrant phenotypes with common and causal pathological processes. *Exp Cell Res,* 395**,** 112209.
76. GOMEZ, M. & GERMAIN, D. 2019. Cross talk between SOD1 and the mitochondrial UPR in cancer and neurodegeneration. *Mol Cell Neurosci,* 98**,** 12-18.
77. GONG, Z., BA, L. & ZHANG, M. 2022. Dysfunction of the oligodendrocytes in amyotrophic lateral sclerosis. *J Biomed Res,* 36**,** 336-342.
78. GORDON, P. H., MITSUMOTO, H. & HAYS, A. P. 2003. Amyotrophic Lateral Sclerosis. *Science of Aging Knowledge Environment,* 2003**,** dn2-dn2.
79. GURNEY, M. E., PU, H., CHIU, A. Y., DAL CANTO, M. C., POLCHOW, C. Y., ALEXANDER, D. D., CALIENDO, J., HENTATI, A., KWON, Y. W., DENG, H. X. & ET AL. 1994. Motor neuron degeneration in mice that express a human Cu,Zn superoxide dismutase mutation. *Science,* 264**,** 1772-5.
80. GUTTENPLAN, K. A., WEIGEL, M. K., ADLER, D. I., COUTHOUIS, J., LIDDELOW, S. A., GITLER, A. D. & BARRES, B. A. 2020. Knockout of reactive astrocyte activating factors slows disease progression in an ALS mouse model. *Nat Commun,* 11**,** 3753.
81. HABIB, N., MCCABE, C., MEDINA, S., VARSHAVSKY, M., KITSBERG, D., DVIR-SZTERNFELD, R., GREEN, G., DIONNE, D., NGUYEN, L., MARSHALL, J. L., CHEN, F., ZHANG, F., KAPLAN, T., REGEV, A. & SCHWARTZ, M. 2020. Disease-associated astrocytes in Alzheimer's disease and aging. *Nat Neurosci,* 23**,** 701-706.
82. HALL, E. D., OOSTVEEN, J. A. & GURNEY, M. E. 1998. Relationship of microglial and astrocytic activation to disease onset and progression in a transgenic model of familial ALS. *Glia,* 23**,** 249-56.
83. HANANI, M. & SPRAY, D. C. 2020. Emerging importance of satellite glia in nervous system function and dysfunction. *Nat Rev Neurosci,* 21**,** 485-498.
84. HAO, Y., HAO, S., ANDERSEN-NISSEN, E., MAUCK, W. M., 3RD, ZHENG, S., BUTLER, A., LEE, M. J., WILK, A. J., DARBY, C., ZAGER, M., HOFFMAN, P., STOECKIUS, M., PAPALEXI, E., MIMITOU, E. P., JAIN, J., SRIVASTAVA, A., STUART, T., FLEMING, L. M., YEUNG, B., ROGERS, A. J., MCELRATH, J. M., BLISH, C. A., GOTTARDO, R., SMIBERT, P. & SATIJA, R. 2021. Integrated analysis of multimodal single-cell data. *Cell,* 184**,** 3573-3587 e29.
85. HARADA, Y., NAGAO, Y., SHIMIZU, S., SERIKAWA, T., TERADA, R., FUJIMOTO, M., OKUDA, A., MUKAI, T., SASA, M., KURACHI, Y. & OHNO, Y. 2013. Expressional analysis of inwardly rectifying Kir4.1 channels in Noda epileptic rat (NER). *Brain Res,* 1517**,** 141-9.
86. HARDY, J. A. & HIGGINS, G. A. 1992. Alzheimer's disease: the amyloid cascade hypothesis. *Science,* 256**,** 184-5.
87. HASEL, P., ROSE, I. V. L., SADICK, J. S., KIM, R. D. & LIDDELOW, S. A. 2021. Neuroinflammatory astrocyte subtypes in the mouse brain. *Nat Neurosci,* 24**,** 1475-1487.

88. HAUKEDAL, H. & FREUDE, K. 2019. Implications of Microglia in Amyotrophic Lateral Sclerosis and Frontotemporal Dementia. *J Mol Biol,* 431**,** 1818-1829.
89. HEIMAN-PATTERSON, T. D., SHER, R. B., BLANKENHORN, E. A., ALEXANDER, G., DEITCH, J. S., KUNST, C. B., MARAGAKIS, N. & COX, G. 2011. Effect of genetic background on phenotype variability in transgenic mouse models of amyotrophic lateral sclerosis: a window of opportunity in the search for genetic modifiers. *Amyotroph Lateral Scler,* 12**,** 79-86.
90. HERCULANO-HOUZEL, S. 2014. The glia/neuron ratio: how it varies uniformly across brain structures and species and what that means for brain physiology and evolution. *Glia,* 62**,** 1377-91.
91. HERRMANN, J. E., IMURA, T., SONG, B., QI, J., AO, Y., NGUYEN, T. K., KORSAK, R. A., TAKEDA, K., AKIRA, S. & SOFRONIEW, M. V. 2008. STAT3 is a Critical Regulator of Astrogliosis and Scar Formation after Spinal Cord Injury. *The Journal of Neuroscience,* 28**,** 7231.
92. HOL, E. M. & PEKNY, M. 2015. Glial fibrillary acidic protein (GFAP) and the astrocyte intermediate filament system in diseases of the central nervous system. *Curr Opin Cell Biol,* 32**,** 121-30.
93. HOOVER, B. R., REED, M. N., SU, J., PENROD, R. D., KOTILINEK, L. A., GRANT, M. K., PITSTICK, R., CARLSON, G. A., LANIER, L. M., YUAN, L. L., ASHE, K. H. & LIAO, D. 2010. Tau mislocalization to dendritic spines mediates synaptic dysfunction independently of neurodegeneration. *Neuron,* 68**,** 1067-81.
94. HOWLAND, D. S., LIU, J., SHE, Y., GOAD, B., MARAGAKIS, N. J., KIM, B., ERICKSON, J., KULIK, J., DEVITO, L., PSALTIS, G., DEGENNARO, L. J., CLEVELAND, D. W. & ROTHSTEIN, J. D. 2002a. Focal loss of the glutamate transporter EAAT2 in a transgenic rat model of SOD1 mutant-mediated amyotrophic lateral sclerosis (ALS). *Proceedings of the National Academy of Sciences of the United States of America,* 99**,** 1604-1609.
95. HOWLAND, D. S., LIU, J., SHE, Y., GOAD, B., MARAGAKIS, N. J., KIM, B., ERICKSON, J., KULIK, J., DEVITO, L., PSALTIS, G., DEGENNARO, L. J., CLEVELAND, D. W. & ROTHSTEIN, J. D. 2002b. Focal loss of the glutamate transporter EAAT2 in a transgenic rat model of SOD1 mutant-mediated amyotrophic lateral sclerosis (ALS). *Proceedings of the National Academy of Sciences,* 99**,** 1604-1609.
96. HUXLEY, A. F. & STAMPFLI, R. 1949. Evidence for saltatory conduction in peripheral myelinated nerve fibres. *J Physiol,* 108**,** 315-39.
97. HYND, M. R., SCOTT, H. L. & DODD, P. R. 2004. Glutamate-mediated excitotoxicity and neurodegeneration in Alzheimer's disease. *Neurochem Int,* 45**,** 583-95.
98. JAKEL, S., AGIRRE, E., MENDANHA FALCAO, A., VAN BRUGGEN, D., LEE, K. W., KNUESEL, I., MALHOTRA, D., FFRENCH-CONSTANT, C., WILLIAMS, A. & CASTELO-BRANCO, G. 2019. Altered human oligodendrocyte heterogeneity in multiple sclerosis. *Nature,* 566**,** 543-547.
99. JANA, M. & PAHAN, K. 2005. Redox regulation of cytokine-mediated inhibition of myelin gene expression in human primary oligodendrocytes. *Free Radic Biol Med,* 39**,** 823-31.
100. JANIGRO, D. 2012. Are you in or out? Leukocyte, ion, and neurotransmitter permeability across the epileptic blood-brain barrier. *Epilepsia,* 53 Suppl 1**,** 26-34.
101. JANKOVIC, T., DOLENEC, P., RAJIC BUMBER, J., GRZETA, N., KRIZ, J., ZUPAN, G. & PILIPOVIC, K. 2021. Differential Expression Patterns of TDP-43 in Single Moderate versus Repetitive Mild Traumatic Brain Injury in Mice. *Int J Mol Sci,* 22.

102. JARA, J. H., GENC, B., STANFORD, M. J., PYTEL, P., ROOS, R. P., WEINTRAUB, S., MESULAM, M. M., BIGIO, E. H., MILLER, R. J. & OZDINLER, P. H. 2017. Evidence for an early innate immune response in the motor cortex of ALS. *J Neuroinflammation,* 14**,** 129.

103. JONSSON, T., ATWAL, J. K., STEINBERG, S., SNAEDAL, J., JONSSON, P. V., BJORNSSON, S., STEFANSSON, H., SULEM, P., GUDBJARTSSON, D., MALONEY, J., HOYTE, K., GUSTAFSON, A., LIU, Y., LU, Y., BHANGALE, T., GRAHAM, R. R., HUTTENLOCHER, J., BJORNSDOTTIR, G., ANDREASSEN, O. A., JONSSON, E. G., PALOTIE, A., BEHRENS, T. W., MAGNUSSON, O. T., KONG, A., THORSTEINSDOTTIR, U., WATTS, R. J. & STEFANSSON, K. 2012. A mutation in APP protects against Alzheimer's disease and age-related cognitive decline. *Nature,* 488**,** 96-9.

104. KAISER, M., MALETZKI, I., HULSMANN, S., HOLTMANN, B., SCHULZ-SCHAEFFER, W., KIRCHHOFF, F., BAHR, M. & NEUSCH, C. 2006. Progressive loss of a glial potassium channel (KCNJ10) in the spinal cord of the SOD1 (G93A) transgenic mouse model of amyotrophic lateral sclerosis. *J Neurochem,* 99**,** 900-12.

105. KANG, S. H., LI, Y., FUKAYA, M., LORENZINI, I., CLEVELAND, D. W., OSTROW, L. W., ROTHSTEIN, J. D. & BERGLES, D. E. 2013. Degeneration and impaired regeneration of gray matter oligodendrocytes in amyotrophic lateral sclerosis. *Nat Neurosci,* 16**,** 571-9.

106. KAUR, A., SHUKEN, S., YANG, A. C. & IRAM, T. 2023. A protocol for collection and infusion of cerebrospinal fluid in mice. *STAR Protoc,* 4**,** 102015.

107. KAWAMATA, H., NG, S. K., DIAZ, N., BURSTEIN, S., MOREL, L., OSGOOD, A., SIDER, B., HIGASHIMORI, H., HAYDON, P. G., MANFREDI, G. & YANG, Y. 2014. Abnormal intracellular calcium signaling and SNARE-dependent exocytosis contributes to SOD1G93A astrocyte-mediated toxicity in amyotrophic lateral sclerosis. *J Neurosci,* 34**,** 2331-48.

108. KAYA, T., MATTUGINI, N., LIU, L., JI, H., CANTUTI-CASTELVETRI, L., WU, J., SCHIFFERER, M., GROH, J., MARTINI, R., BESSON-GIRARD, S., KAJI, S., LIESZ, A., GOKCE, O. & SIMONS, M. 2022. CD8(+) T cells induce interferon-responsive oligodendrocytes and microglia in white matter aging. *Nat Neurosci,* 25**,** 1446-1457.

109. KEEP, R. F., ULANSKI, L. J., 2ND, XIANG, J., ENNIS, S. R. & LORRIS BETZ, A. 1999. Blood-brain barrier mechanisms involved in brain calcium and potassium homeostasis. *Brain Res,* 815**,** 200-5.

110. KELLEY, K. W., BEN HAIM, L., SCHIRMER, L., TYZACK, G. E., TOLMAN, M., MILLER, J. G., TSAI, H. H., CHANG, S. M., MOLOFSKY, A. V., YANG, Y., PATANI, R., LAKATOS, A., ULLIAN, E. M. & ROWITCH, D. H. 2018. Kir4.1-Dependent Astrocyte-Fast Motor Neuron Interactions Are Required for Peak Strength. *Neuron,* 98**,** 306-319 e7.

111. KENIGSBUCH, M., BOST, P., HALEVI, S., CHANG, Y., CHEN, S., MA, Q., HAJBI, R., SCHWIKOWSKI, B., BODENMILLER, B., FU, H., SCHWARTZ, M. & AMIT, I. 2022. A shared disease-associated oligodendrocyte signature among multiple CNS pathologies. *Nat Neurosci,* 25**,** 876-886.

112. KEREN-SHAUL, H., SPINRAD, A., WEINER, A., MATCOVITCH-NATAN, O., DVIR-SZTERNFELD, R., ULLAND, T. K., DAVID, E., BARUCH, K., LARA-ASTAISO, D., TOTH, B., ITZKOVITZ, S., COLONNA, M., SCHWARTZ, M. & AMIT, I. 2017. A Unique Microglia Type Associated with Restricting Development of Alzheimer's Disease. *Cell,* 169**,** 1276-1290 e17.

113. KETTENMANN, H. & RANSOM, B. R. 2004. The concept of neuroglia: a historical perspective. *Neuroglia.* Oxford University Press.

114. KETTENMANN, H. & ZOREC, R. 2012. Release of Gliotransmitters and Transmitter Receptors in Astrocytes. *In:* KETTENMANN, H. & RANSOM, B. R. (eds.) *Neuroglia.* Oxford University Press %[7/9/2024 %U https://doi.org/10.1093/med/9780199794591.003.0017 %1 Oxford Academic.

115. KHAKH, B. S., BEAUMONT, V., CACHOPE, R., MUNOZ-SANJUAN, I., GOLDMAN, S. A. & GRANTYN, R. 2017. Unravelling and Exploiting Astrocyte Dysfunction in Huntington's Disease. *Trends Neurosci,* 40**,** 422-437.

116. KIM, L. D. & FACTORA, R. M. 2018. Alzheimer dementia: Starting, stopping drug therapy. *Cleve Clin J Med,* 85**,** 209-214.

117. KIRBY, L. & CASTELO-BRANCO, G. 2021. Crossing boundaries: Interplay between the immune system and oligodendrocyte lineage cells. *Semin Cell Dev Biol,* 116**,** 45-52.

118. KOLENICOVA, D., TURECKOVA, J., PUKAJOVA, B., HARANTOVA, L., KRISKA, J., KIRDAJOVA, D., VORISEK, I., KAMENICKA, M., VALIHRACH, L., ANDROVIC, P., KUBISTA, M., VARGOVA, L. & ANDEROVA, M. 2020. High potassium exposure reveals the altered ability of astrocytes to regulate their volume in the aged hippocampus of GFAP/EGFP mice. *Neurobiol Aging,* 86**,** 162-181.

119. KRASEMANN, S., MADORE, C., CIALIC, R., BAUFELD, C., CALCAGNO, N., EL FATIMY, R., BECKERS, L., O'LOUGHLIN, E., XU, Y., FANEK, Z., GRECO, D. J., SMITH, S. T., TWEET, G., HUMULOCK, Z., ZRZAVY, T., CONDE-SANROMAN, P., GACIAS, M., WENG, Z., CHEN, H., TJON, E., MAZAHERI, F., HARTMANN, K., MADI, A., ULRICH, J. D., GLATZEL, M., WORTHMANN, A., HEEREN, J., BUDNIK, B., LEMERE, C., IKEZU, T., HEPPNER, F. L., LITVAK, V., HOLTZMAN, D. M., LASSMANN, H., WEINER, H. L., OCHANDO, J., HAASS, C. & BUTOVSKY, O. 2017. The TREM2-APOE Pathway Drives the Transcriptional Phenotype of Dysfunctional Microglia in Neurodegenerative Diseases. *Immunity,* 47**,** 566-581 e9.

120. KULIJEWICZ-NAWROT, M., VERKHRATSKY, A., CHVATAL, A., SYKOVA, E. & RODRIGUEZ, J. J. 2012. Astrocytic cytoskeletal atrophy in the medial prefrontal cortex of a triple transgenic mouse model of Alzheimer's disease. *J Anat,* 221**,** 252-62.

121. KUO, J. J., SCHONEWILLE, M., SIDDIQUE, T., SCHULTS, A. N., FU, R., BAR, P. R., ANELLI, R., HECKMAN, C. J. & KROESE, A. B. 2004. Hyperexcitability of cultured spinal motoneurons from presymptomatic ALS mice. *J Neurophysiol,* 91**,** 571-5.

122. KUO, J. J., SIDDIQUE, T., FU, R. & HECKMAN, C. J. 2005. Increased persistent Na(+) current and its effect on excitability in motoneurones cultured from mutant SOD1 mice. *J Physiol,* 563**,** 843-54.

123. LAPILOVER, E. G., LIPPMANN, K., SALAR, S., MASLAROVA, A., DREIER, J. P., HEINEMANN, U. & FRIEDMAN, A. 2012. Peri-infarct blood-brain barrier dysfunction facilitates induction of spreading depolarization associated with epileptiform discharges. *Neurobiol Dis,* 48**,** 495-506.

124. LARSEN, B. R., STOICA, A. & MACAULAY, N. 2016. Managing Brain Extracellular K(+) during Neuronal Activity: The Physiological Role of the Na(+)/K(+)-ATPase Subunit Isoforms. *Front Physiol,* 7**,** 141.

125. LAURIAT, T. L. & MCINNES, L. A. 2007. EAAT2 regulation and splicing: relevance to psychiatric and neurological disorders. *Mol Psychiatry,* 12**,** 1065-78.

126. LAWSON, L. J., PERRY, V. H., DRI, P. & GORDON, S. 1990. Heterogeneity in the distribution and morphology of microglia in the normal adult mouse brain. *Neuroscience,* 39**,** 151-170.

127. LEE, S. H., REZZONICO, M. G., FRIEDMAN, B. A., HUNTLEY, M. H., MEILANDT, W. J., PANDEY, S., CHEN, Y. J., EASTON, A., MODRUSAN, Z., HANSEN, D. V., SHENG, M. & BOHLEN, C. J. 2021. TREM2-independent oligodendrocyte, astrocyte, and T cell responses to tau and amyloid pathology in mouse models of Alzheimer disease. *Cell Rep,* 37**,** 110158.

128. LEE, Y., MORRISON, B. M., LI, Y., LENGACHER, S., FARAH, M. H., HOFFMAN, P. N., LIU, Y., TSINGALIA, A., JIN, L., ZHANG, P. W., PELLERIN, L., MAGISTRETTI, P. J. & ROTHSTEIN, J. D. 2012. Oligodendroglia metabolically support axons and contribute to neurodegeneration. *Nature,* 487**,** 443-8.

129. LI, K., JAVED, E., HALA, T. J., SANNIE, D., REGAN, K. A., MARAGAKIS, N. J., WRIGHT, M. C., POULSEN, D. J. & LEPORE, A. C. 2015. Transplantation of glial progenitors that overexpress glutamate transporter GLT1 preserves diaphragm function following cervical SCI. *Mol Ther,* 23**,** 533-48.

130. LI, T. & ZHANG, S. 2016. Microgliosis in the Injured Brain: Infiltrating Cells and Reactive Microglia Both Play a Role. *Neuroscientist,* 22**,** 165-70.

131. LIAO, B., ZHAO, W., BEERS, D. R., HENKEL, J. S. & APPEL, S. H. 2012. Transformation from a neuroprotective to a neurotoxic microglial phenotype in a mouse model of ALS. *Exp Neurol,* 237**,** 147-52.

132. LIM, J. L., VAN DER POL, S. M., BARON, W., MCCORD, J. M., DE VRIES, H. E. & VAN HORSSEN, J. 2016. Protandim Protects Oligodendrocytes against an Oxidative Insult. *Antioxidants (Basel),* 5.

133. LIMONE, F., MORDES, D. A., COUTO, A., JOSEPH, B. J., MITCHELL, J. M., THERRIEN, M., GHOSH, S. D., MEYER, D., ZHANG, Y., GOLDMAN, M., BORTOLIN, L., COBOS, I., STEVENS, B., MCCARROLL, S. A., KADIU, I., BURBERRY, A., PIETILÄINEN, O. & EGGAN, K. 2024. Single-nucleus sequencing reveals enriched expression of genetic risk factors in extratelencephalic neurons sensitive to degeneration in ALS. *Nature Aging*.

134. LIU, H., LEAK, R. K. & HU, X. 2016. Neurotransmitter receptors on microglia. *Stroke Vasc Neurol,* 1**,** 52-58.

135. LIU, W., VENUGOPAL, S., MAJID, S., AHN, I. S., DIAMANTE, G., HONG, J., YANG, X. & CHANDLER, S. H. 2020. Single-cell RNA-seq analysis of the brainstem of mutant SOD1 mice reveals perturbed cell types and pathways of amyotrophic lateral sclerosis. *Neurobiol Dis,* 141**,** 104877.

136. LODA, A. & HEARD, E. 2019. Xist RNA in action: Past, present, and future. *PLoS Genet,* 15**,** e1008333.

137. LONG, J. M. & HOLTZMAN, D. M. 2019. Alzheimer Disease: An Update on Pathobiology and Treatment Strategies. *Cell,* 179**,** 312-339.

138. LONGINETTI, E. & FANG, F. 2019. Epidemiology of amyotrophic lateral sclerosis: an update of recent literature. *Curr Opin Neurol,* 32**,** 771-776.

139. LUN, A. T. L., RIESENFELD, S., ANDREWS, T., DAO, T. P., GOMES, T., PARTICIPANTS IN THE 1ST HUMAN CELL ATLAS, J. & MARIONI, J. C. 2019. EmptyDrops: distinguishing cells from empty droplets in droplet-based single-cell RNA sequencing data. *Genome Biol,* 20**,** 63.

140. LYKETSOS, C. G., CARRILLO, M. C., RYAN, J. M., KHACHATURIAN, A. S., TRZEPACZ, P., AMATNIEK, J., CEDARBAUM, J., BRASHEAR, R. & MILLER, D. S. 2011. Neuropsychiatric symptoms in Alzheimer's disease. *Alzheimers Dement,* 7**,** 532-9.

141. MANCUSO, R., OLIVAN, S., OSTA, R. & NAVARRO, X. 2011. Evolution of gait abnormalities in SOD1(G93A) transgenic mice. *Brain Res,* 1406**,** 65-73.

142. MANGIN, J. M., LI, P., SCAFIDI, J. & GALLO, V. 2012. Experience-dependent regulation of NG2 progenitors in the developing barrel cortex. *Nat Neurosci,* 15**,** 1192-4.

143. MANIATIS, S., AIJO, T., VICKOVIC, S., BRAINE, C., KANG, K., MOLLBRINK, A., FAGEGALTIER, D., ANDRUSIVOVA, Z., SAARENPAA, S., SAIZ-CASTRO, G., CUEVAS, M., WATTERS, A., LUNDEBERG, J., BONNEAU, R. & PHATNANI, H. 2019. Spatiotemporal dynamics of molecular pathology in amyotrophic lateral sclerosis. *Science,* 364**,** 89-93.

144. MARCELLI, S., CORBO, M., IANNUZZI, F., NEGRI, L., BLANDINI, F., NISTICO, R. & FELIGIONI, M. 2018. The Involvement of Post-Translational Modifications in Alzheimer's Disease. *Curr Alzheimer Res,* 15**,** 313-335.

145. MARQUES, S., ZEISEL, A., CODELUPPI, S., VAN BRUGGEN, D., MENDANHA FALCAO, A., XIAO, L., LI, H., HARING, M., HOCHGERNER, H., ROMANOV, R. A., GYLLBORG, D., MUNOZ MANCHADO, A., LA MANNO, G., LONNERBERG, P., FLORIDDIA, E. M., REZAYEE, F., ERNFORS, P., ARENAS, E., HJERLING-LEFFLER, J., HARKANY, T., RICHARDSON, W. D., LINNARSSON, S. & CASTELO-BRANCO, G. 2016. Oligodendrocyte heterogeneity in the mouse juvenile and adult central nervous system. *Science,* 352**,** 1326-1329.

146. MARSH, S. E., WALKER, A. J., KAMATH, T., DISSING-OLESEN, L., HAMMOND, T. R., DE SOYSA, T. Y., YOUNG, A. M. H., MURPHY, S., ABDULRAOUF, A., NADAF, N., DUFORT, C., WALKER, A. C., LUCCA, L. E., KOZAREVA, V., VANDERBURG, C., HONG, S., BULSTRODE, H., HUTCHINSON, P. J., GAFFNEY, D. J., HAFLER, D. A., FRANKLIN, R. J. M., MACOSKO, E. Z. & STEVENS, B. 2022. Dissection of artifactual and confounding glial signatures by single-cell sequencing of mouse and human brain. *Nat Neurosci,* 25**,** 306-316.

147. MARTINEZ-MURIANA, A., MANCUSO, R., FRANCOS-QUIJORNA, I., OLMOS-ALONSO, A., OSTA, R., PERRY, V. H., NAVARRO, X., GOMEZ-NICOLA, D. & LOPEZ-VALES, R. 2016. CSF1R blockade slows the progression of amyotrophic lateral sclerosis by reducing microgliosis and invasion of macrophages into peripheral nerves. *Sci Rep,* 6**,** 25663.

148. MARTINEZ, F. O. & GORDON, S. 2014. The M1 and M2 paradigm of macrophage activation: time for reassessment. *F1000Prime Rep,* 6**,** 13.

149. MARTISKAINEN, H., HERUKKA, S. K., STANCAKOVA, A., PAANANEN, J., SOININEN, H., KUUSISTO, J., LAAKSO, M. & HILTUNEN, M. 2017. Decreased plasma beta-amyloid in the Alzheimer's disease APP A673T variant carriers. *Ann Neurol,* 82**,** 128-132.

150. MATHYS, H., ADAIKKAN, C., GAO, F., YOUNG, J. Z., MANET, E., HEMBERG, M., DE JAGER, P. L., RANSOHOFF, R. M., REGEV, A. & TSAI, L. H. 2017. Temporal Tracking of Microglia Activation in Neurodegeneration at Single-Cell Resolution. *Cell Rep,* 21**,** 366-380.

151. MATSON, K. J. E., RUSS, D. E., KATHE, C., MARIC, D., HUA, I., KRYNITSKY, J., PURSLEY, R., SATHYAMURTHY, A., SQUAIR, J. W., COURTINE, G. & LEVINE, A. J. 2021. A Single Cell Atlas of Spared Tissue Below a Spinal Cord Injury Reveals Cellular Mechanisms of Repair. *bioRxiv***,** 2021.04.28.441862.

152. MATUSOVA, Z., HOL, E. M., PEKNY, M., KUBISTA, M. & VALIHRACH, L. 2023. Reactive astrogliosis in the era of single-cell transcriptomics. *Front Cell Neurosci,* 17**,** 1173200.
153. MCCOMBE, P. A. & HENDERSON, R. D. 2010. Effects of gender in amyotrophic lateral sclerosis. *Gend Med,* 7**,** 557-70.
154. MCGINNIS, C. S., MURROW, L. M. & GARTNER, Z. J. 2019. DoubletFinder: Doublet Detection in Single-Cell RNA Sequencing Data Using Artificial Nearest Neighbors. *Cell Syst,* 8**,** 329-337 e4.
155. MCTIGUE, D. M. & TRIPATHI, R. B. 2008. The life, death, and replacement of oligodendrocytes in the adult CNS. *J Neurochem,* 107**,** 1-19.
156. MEAD, R. J., BENNETT, E. J., KENNERLEY, A. J., SHARP, P., SUNYACH, C., KASHER, P., BERWICK, J., PETTMANN, B., BATTAGLIA, G., AZZOUZ, M., GRIERSON, A. & SHAW, P. J. 2011. Optimised and rapid pre-clinical screening in the SOD1(G93A) transgenic mouse model of amyotrophic lateral sclerosis (ALS). *PLoS One,* 6**,** e23244.
157. MEAD, R. J., SHAN, N., REISER, H. J., MARSHALL, F. & SHAW, P. J. 2023. Amyotrophic lateral sclerosis: a neurodegenerative disorder poised for successful therapeutic translation. *Nat Rev Drug Discov,* 22**,** 185-212.
158. MENASSA, D. A. & GOMEZ-NICOLA, D. 2018. Microglial Dynamics During Human Brain Development. *Front Immunol,* 9**,** 1014.
159. MIGLIARINI, S., SCARICAMAZZA, S., VALLE, C., FERRI, A., PASQUALETTI, M. & FERRARO, E. 2021. Microglia Morphological Changes in the Motor Cortex of hSOD1(G93A) Transgenic ALS Mice. *Brain Sci,* 11.
160. MILLER, S. J., GLATZER, J. C., HSIEH, Y. C. & ROTHSTEIN, J. D. 2018. Cortical astroglia undergo transcriptomic dysregulation in the G93A SOD1 ALS mouse model. *J Neurogenet,* 32**,** 322-335.
161. MILLER, S. J., ZHANG, P. W., GLATZER, J. & ROTHSTEIN, J. D. 2017. Astroglial transcriptome dysregulation in early disease of an ALS mutant SOD1 mouse model. *J Neurogenet,* 31**,** 37-48.
162. MIN, S. W., CHO, S. H., ZHOU, Y., SCHROEDER, S., HAROUTUNIAN, V., SEELEY, W. W., HUANG, E. J., SHEN, Y., MASLIAH, E., MUKHERJEE, C., MEYERS, D., COLE, P. A., OTT, M. & GAN, L. 2010. Acetylation of tau inhibits its degradation and contributes to tauopathy. *Neuron,* 67**,** 953-66.
163. MINATI, L., EDGINTON, T., BRUZZONE, M. G. & GIACCONE, G. 2009. Current concepts in Alzheimer's disease: a multidisciplinary review. *Am J Alzheimers Dis Other Demen,* 24**,** 95-121.
164. MONJE, M. 2018. Myelin Plasticity and Nervous System Function. *Annu Rev Neurosci,* 41**,** 61-76.
165. MORAWSKI, M., BRUCKNER, G., JAGER, C., SEEGER, G., MATTHEWS, R. T. & ARENDT, T. 2012. Involvement of perineuronal and perisynaptic extracellular matrix in Alzheimer's disease neuropathology. *Brain Pathol,* 22**,** 547-61.
166. MULLER, M. & SOMJEN, G. G. 2000. Na(+) and K(+) concentrations, extra- and intracellular voltages, and the effect of TTX in hypoxic rat hippocampal slices. *J Neurophysiol,* 83**,** 735-45.
167. NAGAI, M., RE, D. B., NAGATA, T., CHALAZONITIS, A., JESSELL, T. M., WICHTERLE, H. & PRZEDBORSKI, S. 2007. Astrocytes expressing ALS-linked mutated SOD1 release factors selectively toxic to motor neurons. *Nat Neurosci,* 10**,** 615-22.

168. NAGELE, R. G., D'ANDREA, M. R., LEE, H., VENKATARAMAN, V. & WANG, H. Y. 2003. Astrocytes accumulate A beta 42 and give rise to astrocytic amyloid plaques in Alzheimer disease brains. *Brain Res,* 971**,** 197-209.

169. NAGELE, R. G., WEGIEL, J., VENKATARAMAN, V., IMAKI, H., WANG, K. C. & WEGIEL, J. 2004. Contribution of glial cells to the development of amyloid plaques in Alzheimer's disease. *Neurobiol Aging,* 25**,** 663-74.

170. NELSON, P. T., ALAFUZOFF, I., BIGIO, E. H., BOURAS, C., BRAAK, H., CAIRNS, N. J., CASTELLANI, R. J., CRAIN, B. J., DAVIES, P., DEL TREDICI, K., DUYCKAERTS, C., FROSCH, M. P., HAROUTUNIAN, V., HOF, P. R., HULETTE, C. M., HYMAN, B. T., IWATSUBO, T., JELLINGER, K. A., JICHA, G. A., KOVARI, E., KUKULL, W. A., LEVERENZ, J. B., LOVE, S., MACKENZIE, I. R., MANN, D. M., MASLIAH, E., MCKEE, A. C., MONTINE, T. J., MORRIS, J. C., SCHNEIDER, J. A., SONNEN, J. A., THAL, D. R., TROJANOWSKI, J. Q., TRONCOSO, J. C., WISNIEWSKI, T., WOLTJER, R. L. & BEACH, T. G. 2012. Correlation of Alzheimer disease neuropathologic changes with cognitive status: a review of the literature. *J Neuropathol Exp Neurol,* 71**,** 362-81.

171. NEUPANE, P., THADA, P. K., SINGH, P., FAISAL, A. R., RAI, N., POUDEL, P., WALEED, M. S., QUINONEZ, J., RUXMOHAN, S. & JAIN, E. 2023. Investigating Edaravone Use for Management of Amyotrophic Lateral Sclerosis (ALS): A Narrative Review. *Cureus,* 15**,** e33746.

172. NICHOLSON, C. 1993. Ion-selective microelectrodes and diffusion measurements as tools to explore the brain cell microenvironment. *J Neurosci Methods,* 48**,** 199-213.

173. NICHOLSON, C. & PHILLIPS, J. M. 1981. Ion diffusion modified by tortuosity and volume fraction in the extracellular microenvironment of the rat cerebellum. *J Physiol,* 321**,** 225-57.

174. NIEBROJ-DOBOSZ, I., RAFALOWSKA, J., FIDZIANSKA, A., GADAMSKI, R. & GRIEB, P. 2007. Myelin composition of spinal cord in a model of amyotrophic lateral sclerosis (ALS) in SOD1G93A transgenic rats. *Folia Neuropathol,* 45**,** 236-41.

175. NIESSEN, H. G., ANGENSTEIN, F., SANDER, K., KUNZ, W. S., TEUCHERT, M., LUDOLPH, A. C., HEINZE, H. J., SCHEICH, H. & VIELHABER, S. 2006. In vivo quantification of spinal and bulbar motor neuron degeneration in the G93A-SOD1 transgenic mouse model of ALS by T2 relaxation time and apparent diffusion coefficient. *Exp Neurol,* 201**,** 293-300.

176. NIKODEMOVA, M. & WATTERS, J. J. 2011. Outbred ICR/CD1 mice display more severe neuroinflammation mediated by microglial TLR4/CD14 activation than inbred C57Bl/6 mice. *Neuroscience,* 190**,** 67-74.

177. NISHIYAMA, Y. 2009. Structure and properties of the cellulose microfibril. *Journal of Wood Science,* 55**,** 241-249.

178. NOLAN, M., SCOTT, C., GAMARALLAGE, M. P., LUNN, D., CARPENTER, K., MCDONOUGH, E., MEYER, D., KAANUMALLE, S., SANTAMARIA-PANG, A., TURNER, M. R., TALBOT, K. & ANSORGE, O. 2020. Quantitative patterns of motor cortex proteinopathy across ALS genotypes. *Acta Neuropathol Commun,* 8**,** 98.

179. NOLTE, C., MATYASH, M., PIVNEVA, T., SCHIPKE, C. G., OHLEMEYER, C., HANISCH, U. K., KIRCHHOFF, F. & KETTENMANN, H. 2001. GFAP promoter-controlled EGFP-expressing transgenic mice: a tool to visualize astrocytes and astrogliosis in living brain tissue. *Glia,* 33**,** 72-86.

180. NWAOBI, S. E., CUDDAPAH, V. A., PATTERSON, K. C., RANDOLPH, A. C. & OLSEN, M. L. 2016. The role of glial-specific Kir4.1 in normal and pathological states of the CNS. *Acta Neuropathol,* 132**,** 1-21.

181. O'ROURKE, J. G., BOGDANIK, L., MUHAMMAD, A., GENDRON, T. F., KIM, K. J., AUSTIN, A., CADY, J., LIU, E. Y., ZARROW, J., GRANT, S., HO, R., BELL, S., CARMONA, S., SIMPKINSON, M., LALL, D., WU, K., DAUGHRITY, L., DICKSON, D. W., HARMS, M. B., PETRUCELLI, L., LEE, E. B., LUTZ, C. M. & BALOH, R. H. 2015. C9orf72 BAC Transgenic Mice Display Typical Pathologic Features of ALS/FTD. *Neuron,* 88**,** 892-901.

182. ODDO, S., CACCAMO, A., SHEPHERD, J. D., MURPHY, M. P., GOLDE, T. E., KAYED, R., METHERATE, R., MATTSON, M. P., AKBARI, Y. & LAFERLA, F. M. 2003. Triple-transgenic model of Alzheimer's disease with plaques and tangles: intracellular Abeta and synaptic dysfunction. *Neuron,* 39**,** 409-21.

183. OHNO, Y., KUNISAWA, N. & SHIMIZU, S. 2021. Emerging Roles of Astrocyte Kir4.1 Channels in the Pathogenesis and Treatment of Brain Diseases. *Int J Mol Sci,* 22.

184. OLABARRIA, M., NORISTANI, H. N., VERKHRATSKY, A. & RODRIGUEZ, J. J. 2010. Concomitant astroglial atrophy and astrogliosis in a triple transgenic animal model of Alzheimer's disease. *Glia,* 58**,** 831-8.

185. OUALI ALAMI, N., SCHURR, C., OLDE HEUVEL, F., TANG, L., LI, Q., TASDOGAN, A., KIMBARA, A., NETTEKOVEN, M., OTTAVIANI, G., RAPOSO, C., ROVER, S., ROGERS-EVANS, M., ROTHENHAUSLER, B., ULLMER, C., FINGERLE, J., GRETHER, U., KNUESEL, I., BOECKERS, T. M., LUDOLPH, A., WIRTH, T., ROSELLI, F. & BAUMANN, B. 2018. NF-kappaB activation in astrocytes drives a stage-specific beneficial neuroimmunological response in ALS. *EMBO J,* 37.

186. OZDINLER, P. H., BENN, S., YAMAMOTO, T. H., GUZEL, M., BROWN, R. H., JR. & MACKLIS, J. D. 2011. Corticospinal motor neurons and related subcerebral projection neurons undergo early and specific neurodegeneration in hSOD1G(9)(3)A transgenic ALS mice. *J Neurosci,* 31**,** 4166-77.

187. PALMER, A. L. & OUSMAN, S. S. 2018. Astrocytes and Aging. *Front Aging Neurosci,* 10**,** 337.

188. PAMPHLETT, R., TODD, E., VINK, R., MCQUILTY, R. & CHEEMA, S. S. 2003. Magnesium supplementation does not delay disease onset or increase survival in a mouse model of familial ALS. *J Neurol Sci,* 216**,** 95-8.

189. PAOLICELLI, R. C., SIERRA, A., STEVENS, B., TREMBLAY, M.-E., AGUZZI, A., AJAMI, B., AMIT, I., AUDINAT, E., BECHMANN, I., BENNETT, M., BENNETT, F., BESSIS, A., BIBER, K., BILBO, S., BLURTON-JONES, M., BODDEKE, E., BRITES, D., BRÔNE, B., BROWN, G. C., BUTOVSKY, O., CARSON, M. J., CASTELLANO, B., COLONNA, M., COWLEY, S. A., CUNNINGHAM, C., DAVALOS, D., DE JAGER, P. L., DE STROOPER, B., DENES, A., EGGEN, B. J. L., EYO, U., GALEA, E., GAREL, S., GINHOUX, F., GLASS, C. K., GOKCE, O., GOMEZ-NICOLA, D., GONZÁLEZ, B., GORDON, S., GRAEBER, M. B., GREENHALGH, A. D., GRESSENS, P., GRETER, M., GUTMANN, D. H., HAASS, C., HENEKA, M. T., HEPPNER, F. L., HONG, S., HUME, D. A., JUNG, S., KETTENMANN, H., KIPNIS, J., KOYAMA, R., LEMKE, G., LYNCH, M., MAJEWSKA, A., MALCANGIO, M., MALM, T., MANCUSO, R., MASUDA, T., MATTEOLI, M., MCCOLL, B. W., MIRON, V. E., MOLOFSKY, A. V., MONJE, M., MRACSKO, E., NADJAR, A., NEHER, J. J., NENISKYTE, U., NEUMANN, H., NODA, M., PENG, B., PERI, F., PERRY, V. H., POPOVICH, P. G., PRIDANS, C., PRILLER, J., PRINZ, M., RAGOZZINO, D.,

RANSOHOFF, R. M., SALTER, M. W., SCHAEFER, A., SCHAFER, D. P., SCHWARTZ, M., SIMONS, M., SMITH, C. J., STREIT, W. J., TAY, T. L., TSAI, L.-H., VERKHRATSKY, A., VON BERNHARDI, R., WAKE, H., WITTAMER, V., WOLF, S. A., WU, L.-J. & WYSS-CORAY, T. 2022. Microglia states and nomenclature: A field at its crossroads. *Neuron,* 110**,** 3458-3483.

190. PARK, J., KIM, J.-E. & SONG, T.-J. 2022. The Global Burden of Motor Neuron Disease: An Analysis of the 2019 Global Burden of Disease Study %U https://www.frontiersin.org/journals/neurology/articles/10.3389/fneur.2022.864339. *Frontiers in Neurology,* 13**,** %7 %8 2022-April-21 %9 Original Research %# %! Global burden of motor neuron disease 2019 %* %<.

191. PASANTES-MORALES, H. & VAZQUEZ-JUAREZ, E. 2012. Transporters and channels in cytotoxic astrocyte swelling. *Neurochem Res,* 37**,** 2379-87.

192. PEFEROEN, L., KIPP, M., VAN DER VALK, P., VAN NOORT, J. M. & AMOR, S. 2014. Oligodendrocyte-microglia cross-talk in the central nervous system. *Immunology,* 141**,** 302-13.

193. PHATNANI, H. P., GUARNIERI, P., FRIEDMAN, B. A., CARRASCO, M. A., MURATET, M., O'KEEFFE, S., NWAKEZE, C., PAULI-BEHN, F., NEWBERRY, K. M., MEADOWS, S. K., TAPIA, J. C., MYERS, R. M. & MANIATIS, T. 2013. Intricate interplay between astrocytes and motor neurons in ALS. *Proc Natl Acad Sci U S A,* 110**,** E756-65.

194. PHILIPS, T., BENTO-ABREU, A., NONNEMAN, A., HAECK, W., STAATS, K., GEELEN, V., HERSMUS, N., KUSTERS, B., VAN DEN BOSCH, L., VAN DAMME, P., RICHARDSON, W. D. & ROBBERECHT, W. 2013. Oligodendrocyte dysfunction in the pathogenesis of amyotrophic lateral sclerosis. *Brain,* 136**,** 471-82.

195. PIERI, M., CARUNCHIO, I., CURCIO, L., MERCURI, N. B. & ZONA, C. 2009. Increased persistent sodium current determines cortical hyperexcitability in a genetic model of amyotrophic lateral sclerosis. *Exp Neurol,* 215**,** 368-79.

196. PIETROBON, D. & MOSKOWITZ, M. A. 2014. Chaos and commotion in the wake of cortical spreading depression and spreading depolarizations. *Nat Rev Neurosci,* 15**,** 379-93.

197. PIVONKOVA, H., HERMANOVA, Z., KIRDAJOVA, D., AWADOVA, T., MALINSKY, J., VALIHRACH, L., ZUCHA, D., KUBISTA, M., GALISOVA, A., JIRAK, D. & ANDEROVA, M. 2018. The Contribution of TRPV4 Channels to Astrocyte Volume Regulation and Brain Edema Formation. *Neuroscience,* 394**,** 127-143.

198. POCOCK, J. M. & KETTENMANN, H. 2007. Neurotransmitter receptors on microglia. *Trends Neurosci,* 30**,** 527-35.

199. QIAN, K., HUANG, H., PETERSON, A., HU, B., MARAGAKIS, N. J., MING, G. L., CHEN, H. & ZHANG, S. C. 2017. Sporadic ALS Astrocytes Induce Neuronal Degeneration In Vivo. *Stem Cell Reports,* 8**,** 843-855.

200. RAFFAELE, S., BOCCAZZI, M. & FUMAGALLI, M. 2021. Oligodendrocyte Dysfunction in Amyotrophic Lateral Sclerosis: Mechanisms and Therapeutic Perspectives. *Cells,* 10.

201. RAINE, C. S. 1984. The Neuropathology of Myelin Diseases. *In:* MORELL, P. (ed.) *Myelin.* Boston, MA: Springer US.

202. RANGANATHAN, R., HAQUE, S., COLEY, K., SHEPHEARD, S., COOPER-KNOCK, J. & KIRBY, J. 2020. Multifaceted Genes in Amyotrophic Lateral Sclerosis-Frontotemporal Dementia. *Front Neurosci,* 14**,** 684.

203. RANSOHOFF, R. M. 2016. How neuroinflammation contributes to neurodegeneration. *Science,* 353**,** 777-83.

204. RIDLER, T. W. & CALVARD, S. 1978. Picture Thresholding Using an Iterative Selection Method. *Ieee Transactions on Systems Man and Cybernetics,* 8**,** 630-632.

205. RINHOLM, J. E., HAMILTON, N. B., KESSARIS, N., RICHARDSON, W. D., BERGERSEN, L. H. & ATTWELL, D. 2011. Regulation of oligodendrocyte development and myelination by glucose and lactate. *J Neurosci,* 31**,** 538-48.

206. RODRIGUEZ-ARELLANO, J. J., PARPURA, V., ZOREC, R. & VERKHRATSKY, A. 2016. Astrocytes in physiological aging and Alzheimer's disease. *Neuroscience,* 323**,** 170-82.

207. RODRIGUEZ-GOMEZ, J. A., KAVANAGH, E., ENGSKOG-VLACHOS, P., ENGSKOG, M. K. R., HERRERA, A. J., ESPINOSA-OLIVA, A. M., JOSEPH, B., HAJJI, N., VENERO, J. L. & BURGUILLOS, M. A. 2020. Microglia: Agents of the CNS Pro-Inflammatory Response. *Cells,* 9.

208. RODRIGUEZ, J. J., OLABARRIA, M., CHVATAL, A. & VERKHRATSKY, A. 2009. Astroglia in dementia and Alzheimer's disease. *Cell Death Differ,* 16**,** 378-85.

209. ROITBAK, T. & SYKOVA, E. 1999. Diffusion barriers evoked in the rat cortex by reactive astrogliosis. *Glia,* 28**,** 40-8.

210. ROSEN, D. R., SAPP, P., O'REGAN, J., MCKENNA-YASEK, D., SCHLUMPF, K. S., HAINES, J. L., GUSELLA, J. F., HORVITZ, H. R. & BROWN, R. H., JR. 1994. Genetic linkage analysis of familial amyotrophic lateral sclerosis using human chromosome 21 microsatellite DNA markers. *Am J Med Genet,* 51**,** 61-9.

211. ROSEN, D. R., SIDDIQUE, T., PATTERSON, D., FIGLEWICZ, D. A., SAPP, P., HENTATI, A., DONALDSON, D., GOTO, J., O'REGAN, J. P., DENG, H. X. & ET AL. 1993. Mutations in Cu/Zn superoxide dismutase gene are associated with familial amyotrophic lateral sclerosis. *Nature,* 362**,** 59-62.

212. ROSSI, D. J., BRADY, J. D. & MOHR, C. 2007. Astrocyte metabolism and signaling during brain ischemia. *Nat Neurosci,* 10**,** 1377-86.

213. ROTHSTEIN, J. D. 1996. Therapeutic horizons for amyotrophic lateral sclerosis. *Curr Opin Neurobiol,* 6**,** 679-87.

214. SADICK, J. S., O'DEA, M. R., HASEL, P., DYKSTRA, T., FAUSTIN, A. & LIDDELOW, S. A. 2022. Astrocytes and oligodendrocytes undergo subtype-specific transcriptional changes in Alzheimer's disease. *Neuron,* 110**,** 1788-1805 e10.

215. SALA FRIGERIO, C., WOLFS, L., FATTORELLI, N., THRUPP, N., VOYTYUK, I., SCHMIDT, I., MANCUSO, R., CHEN, W. T., WOODBURY, M. E., SRIVASTAVA, G., MOLLER, T., HUDRY, E., DAS, S., SAIDO, T., KARRAN, E., HYMAN, B., PERRY, V. H., FIERS, M. & DE STROOPER, B. 2019. The Major Risk Factors for Alzheimer's Disease: Age, Sex, and Genes Modulate the Microglia Response to Abeta Plaques. *Cell Rep,* 27**,** 1293-1306 e6.

216. SCHELTENS, P., DE STROOPER, B., KIVIPELTO, M., HOLSTEGE, H., CHETELAT, G., TEUNISSEN, C. E., CUMMINGS, J. & VAN DER FLIER, W. M. 2021. Alzheimer's disease. *Lancet,* 397**,** 1577-1590.

217. SCHINDELIN, J., ARGANDA-CARRERAS, I., FRISE, E., KAYNIG, V., LONGAIR, M., PIETZSCH, T., PREIBISCH, S., RUEDEN, C., SAALFELD, S., SCHMID, B., TINEVEZ, J. Y., WHITE, D. J., HARTENSTEIN, V., ELICEIRI, K., TOMANCAK, P. & CARDONA, A. 2012. Fiji: an open-source platform for biological-image analysis. *Nat Methods,* 9**,** 676-82.

218. SETHI, M. K. & ZAIA, J. 2017. Extracellular matrix proteomics in schizophrenia and Alzheimer's disease. *Anal Bioanal Chem,* 409**,** 379-394.

219. SHINDO, Y., YAMANAKA, R., HOTTA, K. & OKA, K. 2020. Inhibition of Mg(2+) Extrusion Attenuates Glutamate Excitotoxicity in Cultured Rat Hippocampal Neurons. *Nutrients,* 12.

220. SOFRONIEW, M. V. 2009. Molecular dissection of reactive astrogliosis and glial scar formation. *Trends Neurosci,* 32**,** 638-47.

221. SOFRONIEW, M. V. & VINTERS, H. V. 2010. Astrocytes: biology and pathology. *Acta Neuropathol,* 119**,** 7-35.

222. SOREQ, L., CONSORTIUM, U. K. B. E., NORTH AMERICAN BRAIN EXPRESSION, C., ROSE, J., SOREQ, E., HARDY, J., TRABZUNI, D., COOKSON, M. R., SMITH, C., RYTEN, M., PATANI, R. & ULE, J. 2017. Major Shifts in Glial Regional Identity Are a Transcriptional Hallmark of Human Brain Aging. *Cell Rep,* 18**,** 557-570.

223. STADELMANN, C., TIMMLER, S., BARRANTES-FREER, A. & SIMONS, M. 2019. Myelin in the Central Nervous System: Structure, Function, and Pathology. *Physiol Rev,* 99**,** 1381-1431.

224. STEVENSON, R., SAMOKHINA, E., MANGAT, A., ROSSETTI, I., PURUSHOTHAM, S. S., MALLADI, C. S., MORLEY, J. W. & BUSKILA, Y. 2023. Astrocytic K(+) clearance during disease progression in amyotrophic lateral sclerosis. *Glia,* 71**,** 2456-2472.

225. STOKLUND DITTLAU, K., TERRIE, L., BAATSEN, P., KERSTENS, A., DE SWERT, L., JANKY, R., CORTHOUT, N., MASRORI, P., VAN DAMME, P., HYTTEL, P., MEYER, M., THORREZ, L., FREUDE, K. & VAN DEN BOSCH, L. 2023. FUS-ALS hiPSC-derived astrocytes impair human motor units through both gain-of-toxicity and loss-of-support mechanisms. *Mol Neurodegener,* 18**,** 5.

226. SUBRAMANIAN, A., TAMAYO, P., MOOTHA, V. K., MUKHERJEE, S., EBERT, B. L., GILLETTE, M. A., PAULOVICH, A., POMEROY, S. L., GOLUB, T. R., LANDER, E. S. & MESIROV, J. P. 2005. Gene set enrichment analysis: a knowledge-based approach for interpreting genome-wide expression profiles. *Proc Natl Acad Sci U S A,* 102**,** 15545-50.

227. SUCHA, P., CHMELOVA, M., KAMENICKA, M., BOCHIN, M., OOHASHI, T. & VARGOVA, L. 2020. The Effect of Hapln4 Link Protein Deficiency on Extracellular Space Diffusion Parameters and Perineuronal Nets in the Auditory System During Aging. *Neurochem Res,* 45**,** 68-82.

228. SYKOVÁ, E. 1992. Ion-selective electrodes. *Monitoring neuronal cells: a practical approach (Stamford J, ed)***,** 261-282.

229. SYKOVA, E. & NICHOLSON, C. 2008. Diffusion in brain extracellular space. *Physiol Rev,* 88**,** 1277-340.

230. SYKOVA, E., VORISEK, I., ANTONOVA, T., MAZEL, T., MEYER-LUEHMANN, M., JUCKER, M., HAJEK, M., ORT, M. & BURES, J. 2005. Changes in extracellular space size and geometry in APP23 transgenic mice: a model of Alzheimer's disease. *Proc Natl Acad Sci U S A,* 102**,** 479-84.

231. TAGARELLI, A., PIRO, A., TAGARELLI, G., LAGONIA, P. & QUATTRONE, A. 2006. Alois Alzheimer: a hundred years after the discovery of the eponymous disorder. *Int J Biomed Sci,* 2**,** 196-204.

232. TANG, Y. & LE, W. 2016. Differential Roles of M1 and M2 Microglia in Neurodegenerative Diseases. *Mol Neurobiol,* 53**,** 1181-1194.

233. THORBURN, D., BIRD, G. L., SPENCE, E., MACSWEEN, R. N. & MILLS, P. R. 1996. alpha-Glutathione S-transferase levels in chronic hepatitis C infection and the effect of alpha-interferon therapy. *Clin Chim Acta,* 253**,** 171-80.

234. THORNE, R. G., HRABETOVA, S. & NICHOLSON, C. 2005. Diffusion measurements for drug design. *Nat Mater,* 4**,** 713; author reply 714.

235. TRIPATHI, P., RODRIGUEZ-MUELA, N., KLIM, J. R., DE BOER, A. S., AGRAWAL, S., SANDOE, J., LOPES, C. S., OGLIARI, K. S., WILLIAMS, L. A., SHEAR, M., RUBIN, L. L., EGGAN, K. & ZHOU, Q. 2017. Reactive Astrocytes Promote ALS-like Degeneration and Intracellular Protein Aggregation in Human Motor Neurons by Disrupting Autophagy through TGF-β1. *Stem Cell Reports,* 9**,** 667-680.

236. TSAO, W., JEONG, Y. H., LIN, S., LING, J., PRICE, D. L., CHIANG, P. M. & WONG, P. C. 2012. Rodent models of TDP-43: recent advances. *Brain Res,* 1462**,** 26-39.

237. TURECKOVA, J., KAMENICKA, M., KOLENICOVA, D., FILIPI, T., HERMANOVA, Z., KRISKA, J., MESZAROSOVA, L., PUKAJOVA, B., VALIHRACH, L., ANDROVIC, P., ZUCHA, D., CHMELOVA, M., VARGOVA, L. & ANDEROVA, M. 2021. Compromised Astrocyte Swelling/Volume Regulation in the Hippocampus of the Triple Transgenic Mouse Model of Alzheimer's Disease. *Front Aging Neurosci,* 13**,** 783120.

238. VAN DEN BOS, M. A. J., GEEVASINGA, N., HIGASHIHARA, M., MENON, P. & VUCIC, S. 2019. Pathophysiology and Diagnosis of ALS: Insights from Advances in Neurophysiological Techniques. *Int J Mol Sci,* 20.

239. VAN DEN BOSCH, L., VAN DAMME, P., BOGAERT, E. & ROBBERECHT, W. 2006. The role of excitotoxicity in the pathogenesis of amyotrophic lateral sclerosis. *Biochim Biophys Acta,* 1762**,** 1068-82.

240. VEGH, M. J., HELDRING, C. M., KAMPHUIS, W., HIJAZI, S., TIMMERMAN, A. J., LI, K. W., VAN NIEROP, P., MANSVELDER, H. D., HOL, E. M., SMIT, A. B. & VAN KESTEREN, R. E. 2014. Reducing hippocampal extracellular matrix reverses early memory deficits in a mouse model of Alzheimer's disease. *Acta Neuropathol Commun,* 2**,** 76.

241. VERKHRATSKY, A. & NEDERGAARD, M. 2018. Physiology of Astroglia. *Physiol Rev,* 98**,** 239-389.

242. VERKHRATSKY, A., UNTIET, V. & ROSE, C. R. 2020. Ionic signalling in astroglia beyond calcium. *Journal of Physiology-London,* 598**,** 1655-1670.

243. VITVITSKY, V. M., GARG, S. K., KEEP, R. F., ALBIN, R. L. & BANERJEE, R. 2012. Na+ and K+ ion imbalances in Alzheimer's disease. *Biochim Biophys Acta,* 1822**,** 1671-81.

244. VORISEK, I. & SYKOVA, E. 1997. Ischemia-induced changes in the extracellular space diffusion parameters, K+, and pH in the developing rat cortex and corpus callosum. *J Cereb Blood Flow Metab,* 17**,** 191-203.

245. VOSKUHL, R. R., PETERSON, R. S., SONG, B., AO, Y., MORALES, L. B. J., TIWARI-WOODRUFF, S. & SOFRONIEW, M. V. 2009. Reactive Astrocytes Form Scar-Like Perivascular Barriers to Leukocytes during Adaptive Immune Inflammation of the CNS. *The Journal of Neuroscience,* 29**,** 11511.

246. VUCIC, S., PAVEY, N., HAIDAR, M., TURNER, B. J. & KIERNAN, M. C. 2021. Cortical hyperexcitability: Diagnostic and pathogenic biomarker of ALS. *Neurosci Lett,* 759**,** 136039.

247. WALCH, E., MURPHY, T. R., CUVELIER, N., ALDOGHMI, M., MOROZOVA, C., DONOHUE, J., YOUNG, G., SAMANT, A., GARCIA, S., ALVAREZ, C., BILAS, A., DAVILA, D., BINDER, D. K. & FIACCO, T. A. 2020. Astrocyte-Selective Volume Increase in Elevated Extracellular Potassium Conditions Is Mediated by the Na(+)/K(+) ATPase and Occurs Independently of Aquaporin 4. *ASN Neuro,* 12**,** 1759091420967152.

248. WEINGARTEN, M. D., LOCKWOOD, A. H., HWO, S. Y. & KIRSCHNER, M. W. 1975. A protein factor essential for microtubule assembly. *Proc Natl Acad Sci U S A,* 72**,** 1858-62.

249. WEN, X., XIAO, L., ZHONG, Z., WANG, L., LI, Z., PAN, X. & LIU, Z. 2017. Astaxanthin acts via LRP-1 to inhibit inflammation and reverse lipopolysaccharide-induced M1/M2 polarization of microglial cells. *Oncotarget,* 8**,** 69370-69385.

250. WHEELER, M. A., CLARK, I. C., TJON, E. C., LI, Z., ZANDEE, S. E. J., COUTURIER, C. P., WATSON, B. R., SCALISI, G., ALKWAI, S., ROTHHAMMER, V., ROTEM, A., HEYMAN, J. A., THAPLOO, S., SANMARCO, L. M., RAGOUSSIS, J., WEITZ, D. A., PETRECCA, K., MOFFITT, J. R., BECHER, B., ANTEL, J. P., PRAT, A. & QUINTANA, F. J. 2020. MAFG-driven astrocytes promote CNS inflammation. *Nature,* 578**,** 593-599.

251. WILCOCK, D. M., VITEK, M. P. & COLTON, C. A. 2009. Vascular amyloid alters astrocytic water and potassium channels in mouse models and humans with Alzheimer's disease. *Neuroscience,* 159**,** 1055-69.

252. WILHELMSSON, U., BUSHONG, E. A., PRICE, D. L., SMARR, B. L., PHUNG, V., TERADA, M., ELLISMAN, M. H. & PEKNY, M. 2006. Redefining the concept of reactive astrocytes as cells that remain within their unique domains upon reaction to injury. *Proc Natl Acad Sci U S A,* 103**,** 17513-8.

253. WOODBURN, S. C., BOLLINGER, J. L. & WOHLEB, E. S. 2021. The semantics of microglia activation: neuroinflammation, homeostasis, and stress. *J Neuroinflammation,* 18**,** 258.

254. WU, Y. E., PAN, L., ZUO, Y., LI, X. & HONG, W. 2017. Detecting Activated Cell Populations Using Single-Cell RNA-Seq. *Neuron,* 96**,** 313-329 e6.

255. YAMANAKA, K., CHUN, S. J., BOILLEE, S., FUJIMORI-TONOU, N., YAMASHITA, H., GUTMANN, D. H., TAKAHASHI, R., MISAWA, H. & CLEVELAND, D. W. 2008. Astrocytes as determinants of disease progression in inherited amyotrophic lateral sclerosis. *Nat Neurosci,* 11**,** 251-3.

256. YASUI, M., OTA, K. & YOSHIDA, M. 1997. Effects of low calcium and magnesium dietary intake on the central nervous system tissues of rats and calcium-magnesium related disorders in the amyotrophic lateral sclerosis focus in the Kii Peninsula of Japan. *Magnes Res,* 10**,** 39-50.

257. YERBURY, J. J., OOI, L., DILLIN, A., SAUNDERS, D. N., HATTERS, D. M., BEART, P. M., CASHMAN, N. R., WILSON, M. R. & ECROYD, H. 2016. Walking the tightrope: proteostasis and neurodegenerative disease. *J Neurochem,* 137**,** 489-505.

258. YOU, J., YOUSSEF, M. M. M., SANTOS, J. R., LEE, J. & PARK, J. 2023. Microglia and Astrocytes in Amyotrophic Lateral Sclerosis: Disease-Associated States, Pathological Roles, and Therapeutic Potential. *Biology (Basel),* 12.

259. YOUNG, M. D. & BEHJATI, S. 2020. SoupX removes ambient RNA contamination from droplet-based single-cell RNA sequencing data. *Gigascience,* 9.

260. ZAMANIAN, J. L., XU, L., FOO, L. C., NOURI, N., ZHOU, L., GIFFARD, R. G. & BARRES, B. A. 2012. Genomic analysis of reactive astrogliosis. *J Neurosci,* 32**,** 6391-410.

261. ZAMECNIK, J., HOMOLA, A., CICANIC, M., KUNCOVA, K., MARUSIC, P., KRSEK, P., SYKOVA, E. & VARGOVA, L. 2012. The extracellular matrix and diffusion barriers in focal cortical dysplasias. *Eur J Neurosci,* 36**,** 2017-24.

262. ZAMECNIK, J., VARGOVA, L., HOMOLA, A., KODET, R. & SYKOVA, E. 2004. Extracellular matrix glycoproteins and diffusion barriers in human astrocytic tumours. *Neuropathol Appl Neurobiol,* 30**,** 338-50.
263. ZEIS, T., ENZ, L. & SCHAEREN-WIEMERS, N. 2016. The immunomodulatory oligodendrocyte. *Brain Res,* 1641**,** 139-148.
264. ZHANG, M., SU, J., ZHANG, Y., XU, J. & ZHANG, S. 2018. Conveying endogenous and exogenous signals: MAPK cascades in plant growth and defense. *Curr Opin Plant Biol,* 45**,** 1-10.

10 LIST OF PUBLICATIONS

Publications related to the thesis:

1. Filipi T, Matusova Z, Abaffy P, Vanatko O, Tureckova J, Benesova S, Kubiskova M, Kirdajova D, Zahumensky J, Valihrach L, Anderova M. Cortical glia in SOD1(G93A) mice are subtly affected by ALS-like pathology. Sci Rep. 2023 Apr 21;13(1):6538. doi: 10.1038/s41598-023-33608-y. PMID: 37085528; PMCID: PMC10121704. IF = 3.8

2. Filipi T, Tureckova J, Vanatko O, Chmelova M, Kubiskova M, Sirotova N, Matejkova S, Vargova L, Anderova M. ALS-like pathology diminishes swelling of spinal astrocytes in the SOD1 animal model. Front Cell Neurosci. In press; IF = 4,2

3. Tureckova J, Kamenicka M, Kolenicova D, Filipi T, Hermanova Z, Kriska J, Meszarosova L, Pukajova B, Valihrach L, Androvic P, Zucha D, Chmelova M, Vargova L, Anderova M. Compromised Astrocyte Swelling/Volume Regulation in the Hippocampus of the Triple Transgenic Mouse Model of Alzheimer's Disease. Front Aging Neurosci. 2022 Jan 27;13:783120. doi: 10.3389/fnagi.2021.783120. PMID: 35153718; PMCID: PMC8829436. IF = 4.504

Other publications:

4. Filipi T, Hermanova Z, Tureckova J, Vanatko O, Anderova AM. Glial Cells-The Strategic Targets in Amyotrophic Lateral Sclerosis Treatment. J Clin Med. 2020 Jan 18;9(1):261. doi: 10.3390/jcm9010261. PMID: 31963681; PMCID: PMC7020059. IF = 4.044

11 APENDIX